Geochemistry of the Al Jurf Formation in the Offshore Well C-NC 41, Sabratah Basin, NW Libya

By

Ibrahim Abdalhadi Mohamed Eltekali

Supervisor

Assist. Prof. Osama Shaltami

This Thesis was submitted in Partial Fulfillment of the Requirements for Master's Degree of Science in Geology, Geochemistry

University of Benghazi

Faculty of Science

Dec 2019

University of Benghazi **Faculty of Science**

Department of Earth Science

Geochemistry of the Al Jurf Formation in the Offshore Well C-NC 41, Sabratah Basin, NW Libya

By

Ibrahim Abdalhadi Mohamed Eltekali

This Thesis was Successfully Defended and Approved on **05.12.2019**

Supervisor

Assist. Prof. Osama Shaltami

Signature: .....

Associate. Prof. Saad K. AbdallaEbaidi **(Internal Examiner)**

Signature: .....

Prof. Hamad Mohammed Adres **(External Examiner)**

Signature: .....

Dean of Faculty

Director of Graduate Studies and Training

University of Benghazi
Director of Graduate Studies and Training

صدق الله العظيم

This thesis is dedicated to my parents
and my wife for their love, endless
support and encouragement.

Ibrahim Eltekali, 2019

AKNOWLEDGEMENT

In the Name of Allah, the Most Merciful, the Most Compassionate all praise be to Allah, the Lord of the worlds; and prayers and peace be upon Mohamed His servant and messenger.

First and foremost, I must acknowledge my limitless thanks to Allah, the Ever-Magnificent; the Ever-Thankful, for His help and bless. I am totally sure that this work would have never become truth, without His guidance.

I am greatly indebted to my supervisor Dr. Osama, R. Al Shaltami, Assistant Professor of Geochemistry, Department of Earth Sciences, for his continuous guidance, encouragement and insight motivated me to earn my degree, he was helpful, supportive, patient, and available at all times.

To Doctor Fares Fathi, I express my gratefulness for the discussion and interpretation of some results presented in this thesis.

I owe a deep debt of gratitude to all staff member at the Department of Earth Sciences, Benghazi University for letting me fulfill my dream of being a student here and giving me an opportunity to complete this work.

I would like to extend my thanks to all staff members in AGIP Company to gave the samples and also thanks go to the Laboratory of Chemostratigraphy and Organic Geochemistry (LGQM), State University of Rio de Janeiro (UERJ), Brazil of for preparing and doing the samples analysis, I am really grateful to them.

I would like to take this opportunity to say warm thanks to all my beloved friends, who have been so supportive along the way of doing my thesis.

Finally, I would like to express my wholehearted thanks to my family for their generous support they provided me throughout my entire life and particularly through the process of pursuing the master degree.

LIST OF CONTENTS

LIST OF TABLES

LIST OF FIGURES

ABBREVIATION

TOC = total organic carbon (wt. %).

S_1 = amount of free hydrocarbons in sample (mg/g).

S_2 = amount of hydrocarbons generated through thermal cracking (mg/g) – provides the quantity of hydrocarbons that the rock has the potential to produce through diagenesis.

S_3 = amount of CO_2 (mg of CO_2/g of rock) - reflects the amount of oxygen in the oxidation step.

T_{max} = the temperature at which maximum rate of generation of hydrocarbons occurs.

Hydrogen index: $HI = 100 * S_2 / TOC$.

Oxygen index: $OI = 100 * S_3 / TOC$.

Production index: $PI = S_1 / (S_1 + S_2)$.

Semi-quantitative index: $GP = S_1 / S_2$.

Ro = vitrinite reflectance (wt. %).

Pr/Ph = Pristane/Phytane.

Carbon preference index: $CPI = 2(C_{23} + C_{25} + C_{27} + C_{29})/(C_{22} + 2[C_{24} + C_{26} + C_{28}] + C_{30})$.

Waxiness index: $WI = \Sigma(n\text{-}C_{21}\text{-}n\text{-}C_{31})/\Sigma(n\text{-}C_{15}\text{-}n\text{-}C_{20})$.

TPP = tetracyclic polyprenoid.

Geochemistry of the Al Jurf Formation in the Offshore Well C-NC 41, Sabratah Basin, NW Libya

By

Ibrahim Abdalhadi Mohamed Eltekali

Supervisor

Assist. Prof. Osama Shaltami

ABSTRACT

The petrographical and geochemical evaluation of the black shales of the Al Jurf Formation in the offshore Well C-NC 41, Sabratah Basin, NW Libya, is the main objective of this work. Generally, the black shales of the Upper Member are considered as very good to excellent source rocks, while the black shales of the Lower Member have a fair quality. Smectite, illite, kaolinite, gibbsite, chlorite and mixed layer clays are the main clay minerals. The black shales are considered as mature sediments (ICV< 1). Semi-humid climate is prevalent during deposition. The black shales contain high contents of vitrinite and liptinite, with lesser amounts of inertinite. The organic matter is thermally mature. Kerogens of type II and II/III are predominant in the black shales. The proved depositional environment of the Al Jurf Formation is the suboxic marine.

Keywords: Organic Petrography, Geochemistry, Source Rock, Al Jurf Formation, Sabratah Basin, Libya.

CHAPTER ONE
INTRODUCTION

1.1. General

There are seven sedimentary basins in Libya, namely the Cyrenaica, Sirte, Kufra, Murzuq, Ghadamis, Misratah and Sabratah basins (Fig. 1.1). The Sabratah Basin is located partly in Libyan territory and partly in Tunisian. The Libyan part has an area of 24,000 km^2. It occupies a position between the Jifarah Terrace and the Jarrafa Arch, and the northern boundary is marked by the narrow Zohra Graben (Hallett and Clark-Lowes, 2016). The Sabratah Basin is a pull-apart basin within a complex shear zone. Its southern margin is the Libyan Coastal Fault, a basement shear which connects westwards to the South Atlas Fracture in Algeria. The orientation of the shear zone is related to the Hercynian Nafusah Uplift. The displacement on this fault is about 6,000 ft at top Cretaceous level, but against the Jarrafa Arch on the northern margin only about 1,500 ft (Hallett and Clark-Lowes, 2016). The Mesozoic section thickens dramatically from the Jifarah Terrace into the basin. Well A1-9 on the Jifarah Terrace shows the following tops: Triassic at 1,200 ft subsea, Permian at 6,800 ft and the Hercynian unconformity (Carboniferous) at 10,000 ft (Hallett and Clark-Lowes, 2016). By contrast in the Sabratah Basin Well H1-137 reached the base Oligo-Miocene at 8,700 ft and the top Cretaceous at 9,500 ft. Depth to the top Cretaceous in the basin ranges from 7,500 ft on the southern flank to 17,500 ft in the basin centre and 10,000 ft on the northern flank (Hallett and Clark-Lowes, 2016). Due to salt withdrawal and flowage in the Triassic/Jurassic the top of the Cretaceous is a highly irregular surface (Fig. 1.2). The oldest rocks encountered in the area are Late Triassic in age in Well L1-137, located in the southern Sabratah Basin (Hallett and Clark-Lowes, 2016). These rocks were deposited in a rift basin, and it is likely that they are underlain by older Triassic and Permian rocks as seen on the Jifarah Terrace and in Tunisia. The distribution of Permian formations in the Sabratah Basin is largely unknown (Hallett and Clark-Lowes, 2016). They are well developed on the Jifarah Terrace and westwards into Tunisia, but appear to be mostly absent in the Sirt Embayment to the east. The Jurassic Bi'r al Ghanam Formation in Well L1-137 has a strongly evaporitic character,

and these rocks pass into thick salt deposits in the western Sabratah Basin (Hallett and Clark-Lowes, 2016). In this area the Late Triassic-Early Jurassic evaporites show diapiric features in the form of salt domes, swells and walls. Almost all of the hydrocarbon discoveries in the western Sabratah Basin are located on salt-related structures (Hallett and Clark-Lowes, 2016). Seismic evidence suggests that salt flowage began in the Late Cretaceous and deformation of the section overlying the salt diapers has continued to the present day with the trace of some of the structures visible on the seafloor (Hallett and Clark-Lowes, 2016). Late Jurassic and Early Cretaceous sediments are often overlain by volcanic rocks which are probably of Early Cretaceous age. Marine rocks of Neocomian to Albian age are represented by the Turghat Formation, which formed a shallow water carbonate shelf in the eastern part of the basin. Shallow water to restricted conditions became established during the Late Cretaceous, although deeper water shales are present in the centre of the basin suggesting continued subsidence in this area (Hallett and Clark-Lowes, 2016). Organic shales comparable to the Sirt Shales of the Sirt Basin have not been found in the Sabratah Basin (Fig. 1.3).

The Tertiary succession is characterized by significant facies changes in almost all formations, from basin margin in the south to deep water in the centre and north (Hallett and Clark-Lowes, 2016). Paleocene rocks are only preserved in the northern part of the basin where they show deep water facies, and the contact with the Cretaceous appears to be gradational. A major unconformity at the base of the Eocene reflects an Alpine tectonic episode which resulted in tilting and temporary emergence of the southern part of the basin. Pre-Eocene rocks are progressively truncated to the south, so that in the L1-137 Well Eocene rocks rest on Santonian/Campanian formations and at the southern margin of the basin the entire Cretaceous section has been removed (Hallett and Clark-Lowes, 2016). This event is also accompanied by a localized volcanic episode at the Paleocene-Eocene boundary.

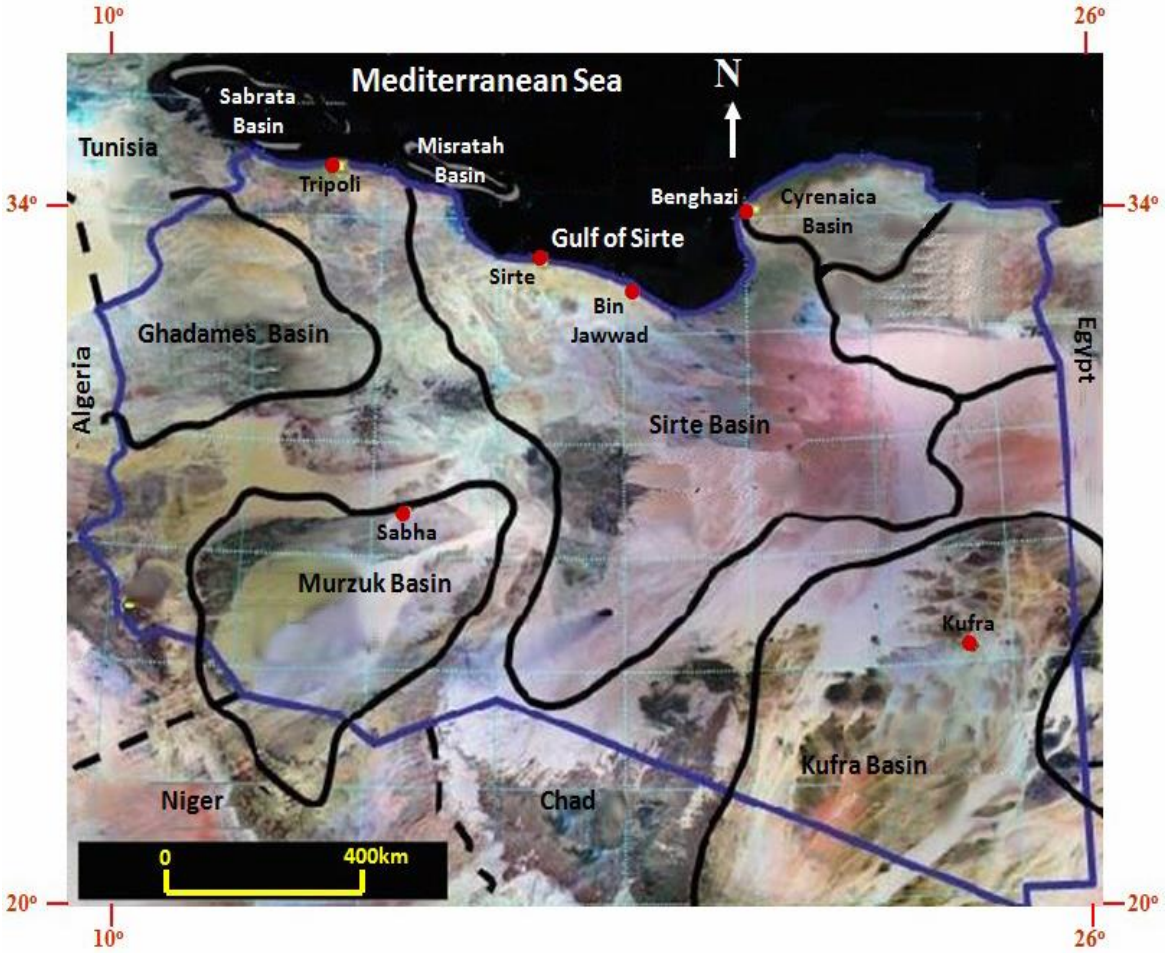

Fig. 1.1: Satellite image showing the sedimentary basins in Libya (after Shaltami, 2012).

A widespread marine transgression during the Early Eocene led to the deposition of the Farwah Group, which contains the principal oil reservoir of the Libyan offshore. The group is widespread in the basin but thins southwards and is absent in Well M1-NC 41. The Farwah Group shows a complete range of facies from lagoonal to deep water. It is overlain with a slight discordance by the Tellil Group of Middle and Late Eocene age which also shows a transition in facies from evaporitic in the south to deep water in the north (Hallett and Clark-Lowes, 2016). The Eocene-Oligocene junction is unconformable, and the Oligocene, like the other Tertiary units, shows a change from shallow shelf facies in the south to deeper water facies in the Bouri area. A significant unconformity separates the Oligocene from the Miocene which is related to wrench tectonics in the Mediterranean. The wrenching produced great instability and rapid subsidence in the Sabratah Basin where

over 6,500 ft of Miocene sediments were deposited. The wrenching produced pull-apart grabens over much of the Pelagian area, including the Zohra Graben which marks the northern limit of the basin (Hallett and Clark-Lowes, 2016).

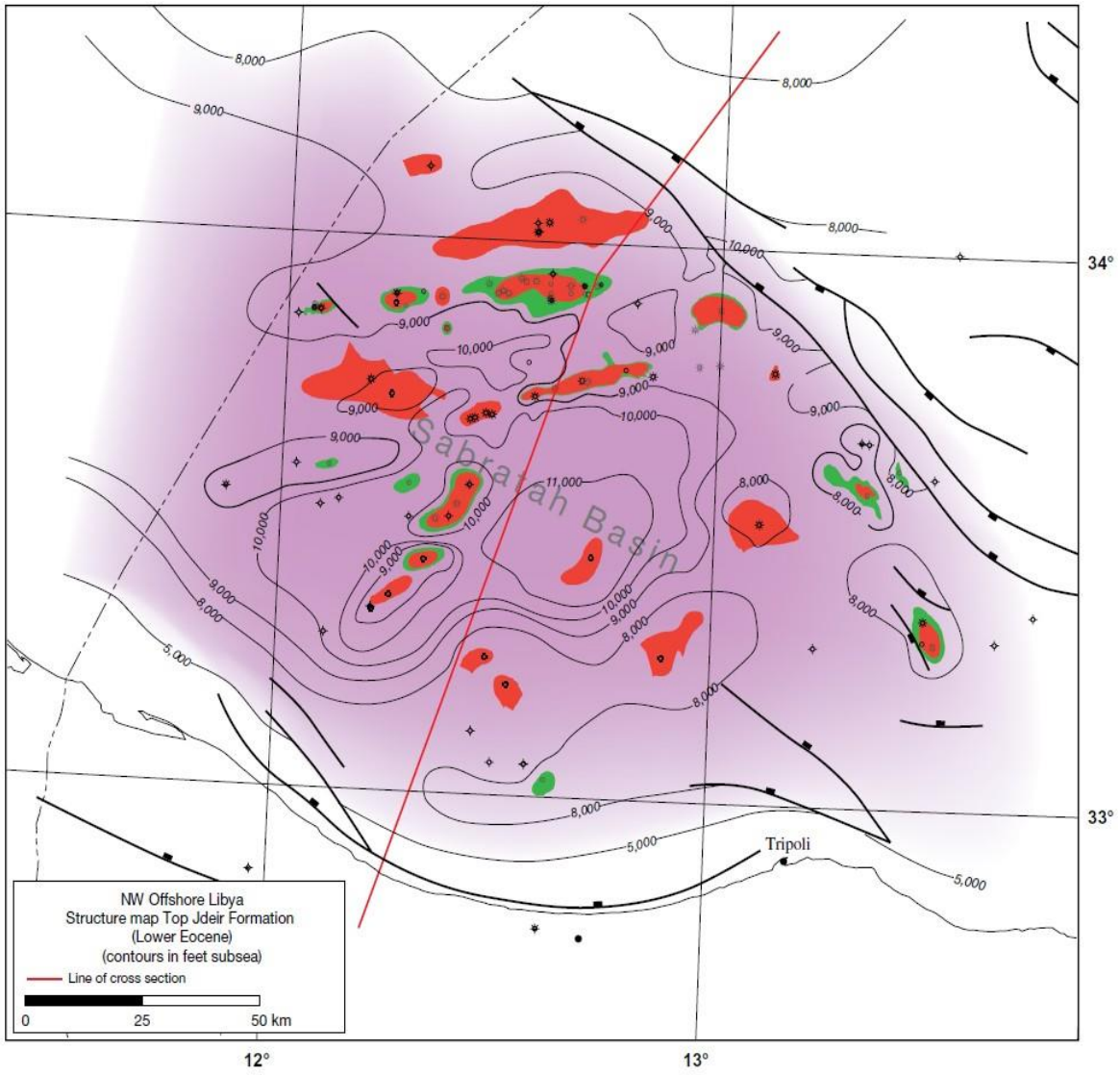

Fig. 1.2: Sabratah Basin top Jdeir Formation (Ypresian) structure map (after Hallett and Clark-Lowes, 2016).

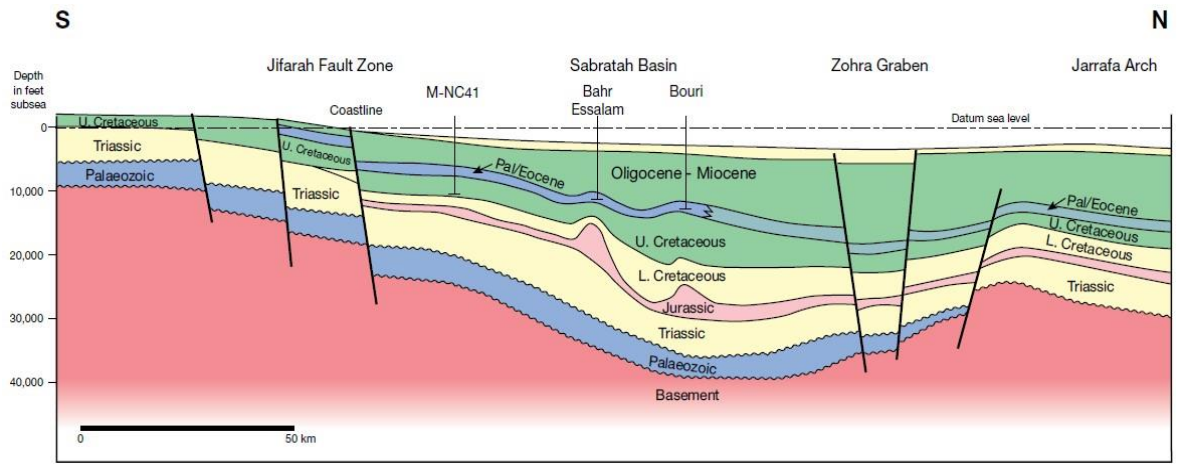

Fig. 1.3: Sabratah Basin S–N cross section (after Hallett and Clark-Lowes, 2016).

The stratigraphic chart of the basin is shown in Figs (1.4-1.5). Moreover, there are two petroleum fields in the basin namely, the Bouri and Bahr Essalam fields (Fig. 1.6).

1.2. Petroleum System of the Sabratah Basin

The Pelagian area, offshore north-west Libya, is a significant petroleum province with over twenty discoveries, most of which contain gas-condensate with or without an oil rim. Potential reservoirs range in age from Jurassic to Miocene, but the principal reservoir is the lower Eocene nummulitic carbonate which contains 80 % of the offshore hydrocarbons so far discovered (Bishop, 1988; Racey *et al.*, 2001). The Early Eocene reservoirs form part of the Farwah Group in Libya and the Metlaoui Group in Tunisia (Bishop, 1988). Smaller discoveries have been made in Cretaceous carbonates (Isis, Miskar). The Eocene trend extends from Sidi el Itayem onshore Tunisia, through the Ashtart, Hasdrubal, Zarat, Salammbo, and Didon discoveries in the Tunisian offshore to the giant Bouri field, E-NC 41, C-NC 41, A-NC 41, and other smaller discoveries in Libyan waters (Bishop, 1988; Anketell and Mriheel, 2000). The group contains a range of facies from restricted evaporites through algal limestones, nummulitic limestones to deeper water globigerinid marls. In the Libyan area most of the hydrocarbon bearing structures are salt-related, whilst in Tunisia most of the structures are syn-sedimentary horsts or faulted anticlines on a seaward dipping ramp (Anketell and Mriheel, 2000).

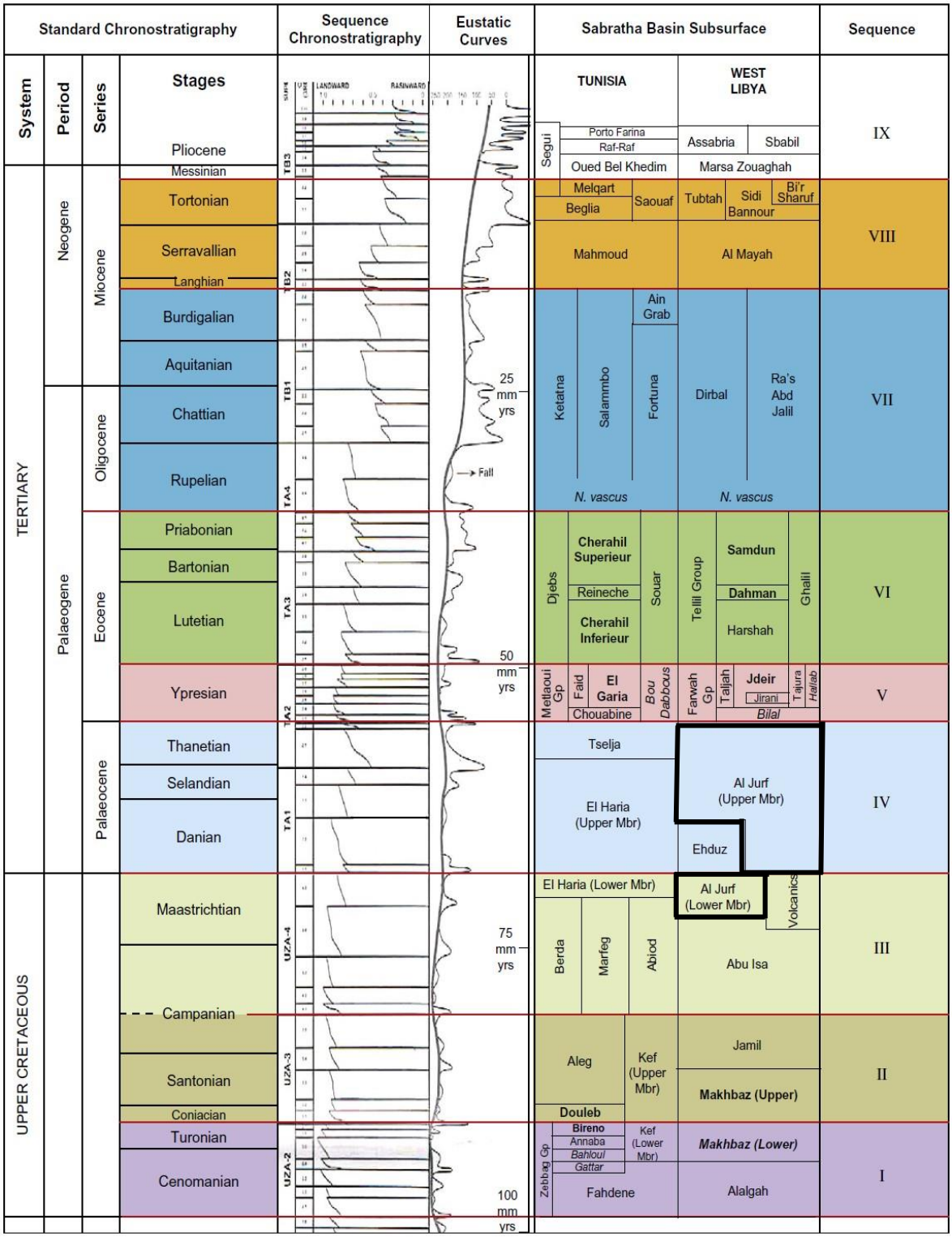

Fig. 1.4: Libyan north-western offshore, time stratigraphic summary chart (after Hammuda et al., 1985; Haq et al., 1988; Hassan and Kendall, 2014).

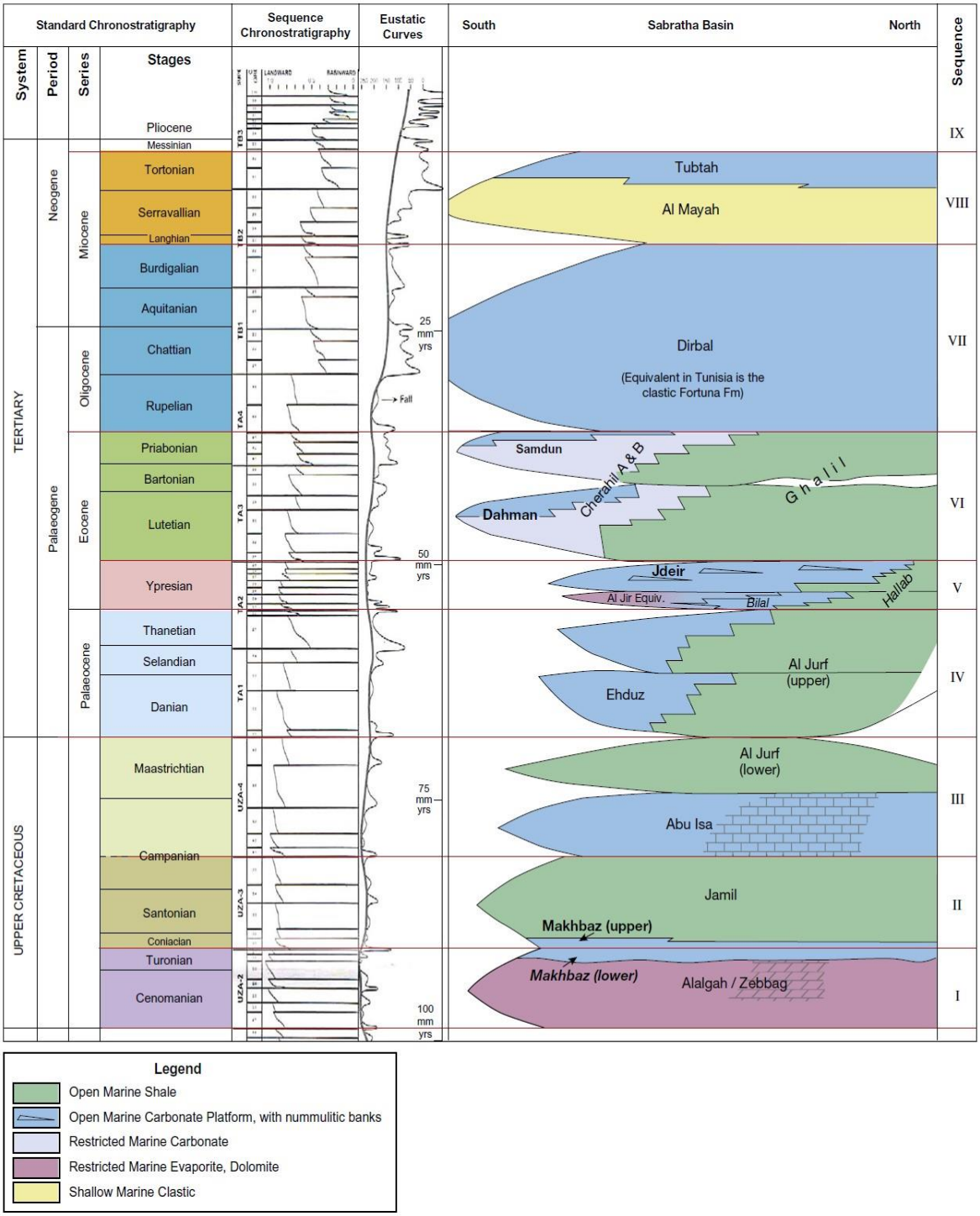

Fig. 1.5: Libyan north-western offshore, schematic chronostratigraphic framework (after Ricchiuto and Pajola, 2003; Fornaciari, 2007).

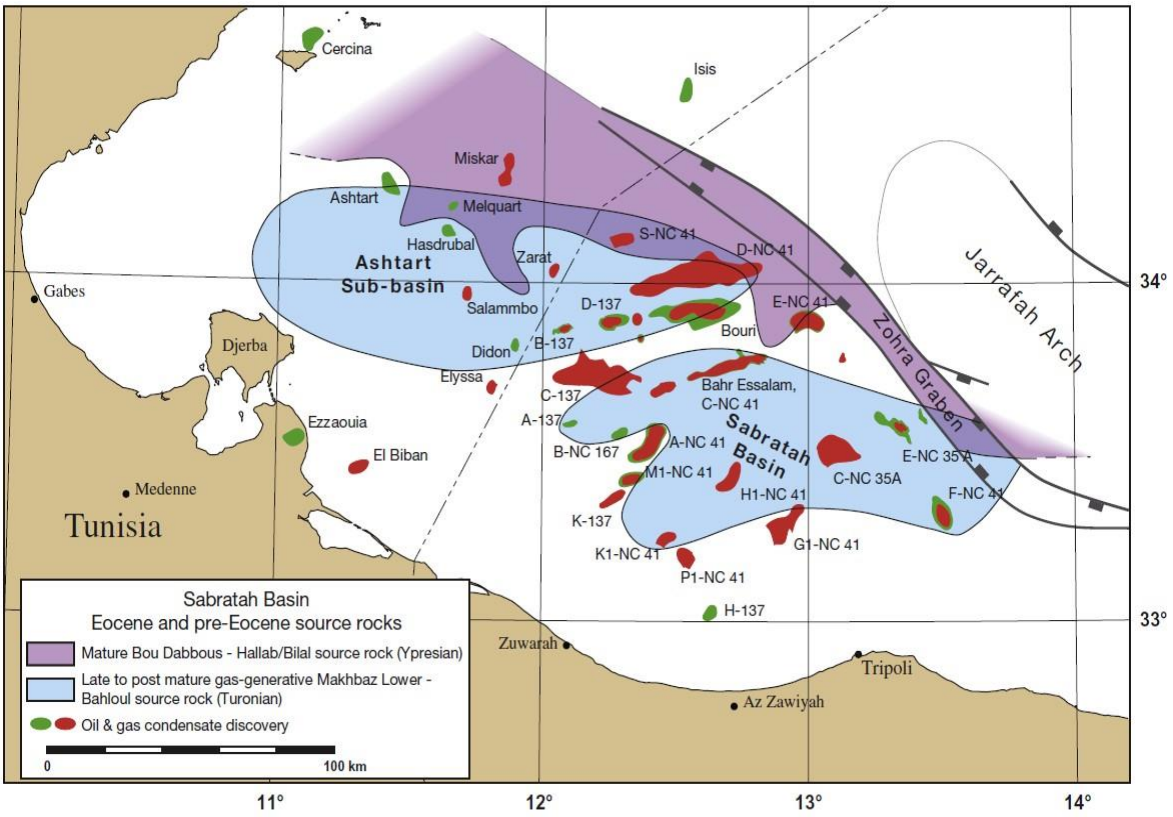

Fig. 1.6: Sabratah Basin oil and gas fields (after Bishop, 1988; Bailey et al., 1989; Sbeta, 1990; Anketell and Mriheel, 2000; Racey et al., 2001).

Geochemical studies in Tunisia indicated that the principal source rock for the Eocene hydrocarbon accumulations is the Ypresian Bou Dabbous Formation, which is the deep water lateral equivalent of the El Garia reservoir (Bailey *et al.*, 1989). In Libya the nummulitic reservoir is the Jdeir Formation and the deep water equivalent is the Hallab/Bilal Formation (Sbeta, 1990; Anketell and Mriheel, 2000, Fig. 1.6).

The Bou Dabbous Formation contains amorphous Type II marine kerogen with TOC values between 0.5 to 2.5 % (Bishop, 1988). Biomarker evidence proves that condensate in Eocene reservoirs on the Hasdrubal, Ashtart and Melqart fields in Tunisia is derived from organic matter in the Bou Dabbous Formation (Racey *et al.*, 2001). At Hasdrubal, which is probably typical of most of the Eocene fields including Bouri, analysis of oil samples shows mature unbiodegraded oil derived from a marine source rock, and carbon isotope ratios show close similarities with other oils known to have been sourced

from the Bou Dabbous Formation (Racey *et al.,* 2001). Furthermore, molecular indicators suggest a migration distance of no more than 5 km. Gas analyses from the same field provide evidence of slight cracking and generation in the peak to late maturity zones. Maturity modeling at Hasdrubal indicates the presence of adjacent source kitchens in which the Bou Dabbous source rock is in the peak to late mature window (Racey *et al.,* 2001). Oil generation began in the Early Miocene with peak generation in the Late Miocene (Bishop, 1988).

Oil and wet gas were sourced at the same time, but the more mobile gas reached the trap first. Studies on whole oils and extracts from the Jdeir Formation and Reineche Member from the Belina 1 well in concession NC 167 in the Libyan part of the basin showed the presence of wet gas in the Jdeir Formation which can be classified as a high thermogenic condensate-associated gas (Anketell and Mriheel, 2000). The Reineche Member gas showed lower maturity and was classified as migrated thermogenic petroleum associated gas. Variations in maturity and composition at Belina strongly suggest different origins for the hydrocarbons and mixing within the reservoirs (Anketell and Mriheel, 2000).

A study of the Metlaoui Group in Tunisia, based on data from twenty offshore wells, revealed an unusually high heat flow (mean value 86 mWm^{-2}), much higher than in the Pantelleria and Linosa grabens further north (Bishop, 1988). The high heat flow is attributable to recent wrenching and volcanism in the southern part of the Pelagian Block. It is also locally affected by the presence of salt walls and pillars. The depth to the oil window in this area varies from 5,900 to 6,250 ft for early mature to 8,259-8,600 ft for peak oil generation, and 11,500 ft for the base of the oil zone (Racey *et al.,* 2001). There is an increase in the level of maturity of the Metlaoui Group from the Reshef well in the north to the Salammbo field in the south (Bailey *et al.,* 1989). The Bou Dabbous source rock contains brown to black limestone horizons containing amorphous kerogen compatible with the high wax paraffinic crudes found at Ashtart, Melqart and Hasdrubal (Hallett and Clark-Lowes, 2016). Algal mats from sabkhas adjacent to restricted lagoons

may also form a second potential source rock within the Metlaoui Group which sourced the Didon, Hammon and Salammbo pools (Racey *et al.,* 2001).

Data from the Libyan sector is scarcer but the situation at Bouri and the other Farwah discoveries is believed to be similar to Hasdrubal, with generation from the adjacent deeper-water marls (which interfingers between the nummulitic shoals), short-distance migration, and emplacement during the Miocene (Anketell and Mriheel, 2000). Bernasconi *et al.,* (1991) presented a series of maps of the Bouri field which showed the presence of open shallow platform and deeper platform facies immediately to the north of the field. Combining the data from Tunisia and from Bouri it seems most likely that the Bouri field was sourced from mature Hallab/Bou Dabbous shales located to the north of the field (Fig. 1.6). Anketell and Mriheel (2000) presented a burial history/maturity plot for a well in the Sabratah Basin which is believed to be from the Bouri area. This shows that the Bou Dabbous source rock entered the oil window during the mid-Miocene but has not yet reached peak maturity.

Eocene source rocks are not present in the Sabratah Basin south of the Eocene nummulitic trend, but evidence from Tunisia suggests that several potential source rocks are present within the Upper Cretaceous (Anketell and Mriheel, 2000). The Bahloul Formation is probably the richest hydrocarbon source rock within the Upper Cretaceous (Fig. 1.6). The Bahloul is a bituminous marly carbonate of Turonian age (Racey *et al.,* 2001). An impression of the location and depth of the Cretaceous source kitchens in the According to Bernasconi *et al.,* (1991) there is a major depocentre in the Sabratah Basin, (shallowing to the north towards Bouri). They added that this depocentre is likely to indicate the location of the Cretaceous source kitchen. The major gas-condensate discoveries of D1-NC 41, E1-NC 41, C1-NC 41 and A1-NC 41 on the northern flank of the depocentre were probably sourced from this kitchen. In the centre of the basin, the base Tertiary is at a depth of 17,500 ft and this probably explains the presence of gas in the C1-NC 35a, F1-NC 41, G1-NC 41, H1-NC 41, M1-NC 41, K1-NC 41 and P1-NC 41 Wells, which are all located in the deepest part of the basin (Bernasconi *et al.,* 1991).

Little studies has been published on other potential source rocks in the Sabratah Basin but a good deal of information is available from Tunisia (Hallett and Clark-Lowes, 2016). The Isis discovery in Tunisia, reservoired in Cenomanian rudistid carbonates, was sourced from the Cenomanian Fahdene shales (Racey *et al.,* 2001). Several other Cretaceous shales and marls have source potential, including the black shales of the Turonian-Campanian Kef and Aleg formations (Racey *et al.,* 2001). The Late Cretaceous (Maastrichtian) Al Jurf Formation (El Haria in Tunisia) was identified by Hammuda *et al.,* (1985) as a possible source rock. The Early Eocene bituminous phosphatic shales of the Chouabine Formation in Tunisia show a strong radioactive response on logs, but this is more likely to be due to the presence of the phosphates (Racey *et al.,* 2001). Post-Ypresian shales such as the Hallab and Ghalil formations in Libya and the Souar and Salammbo formations in Tunisia may also have some source rock potential, although these rocks are probably immature (Hallett and Clark-Lowes, 2016). There are still many unanswered questions on the source rocks of the north-west Libyan offshore and the release of further data on geochemistry of the offshore source rocks would be of great benefit to the exploration effort in this area (Hallett and Clark-Lowes, 2016).

1.3. Present Study

1.3.1. Al Jurf Formation

The Al Jurf Formation was defined in the C-NC 41 Well (Fig. 1.7) in the centre of the Sabratah Basin by Hammuda *et al.,* (1985). The formation spans the Cretaceous-Paleocene boundary, and foraminiferal evidence suggests that the age ranges from mid-Maastrichtian to latest Paleocene (Hallett, 2002). The total thickness of the formation in the type well is 414m (Hallett, 2002). Southwards from the type well the formation thins towards the basin margin and in Well G-NC 41 only 17 m of the Al Jurf Formation is present (Hallett, 2002). Hammuda *et al.,* (1985) divided the Al Jurf Formation into Lower Member and Upper Member. The lithology of the formation suggests deposition in open marine conditions in an outer shelf environment (Hallett, 2002).

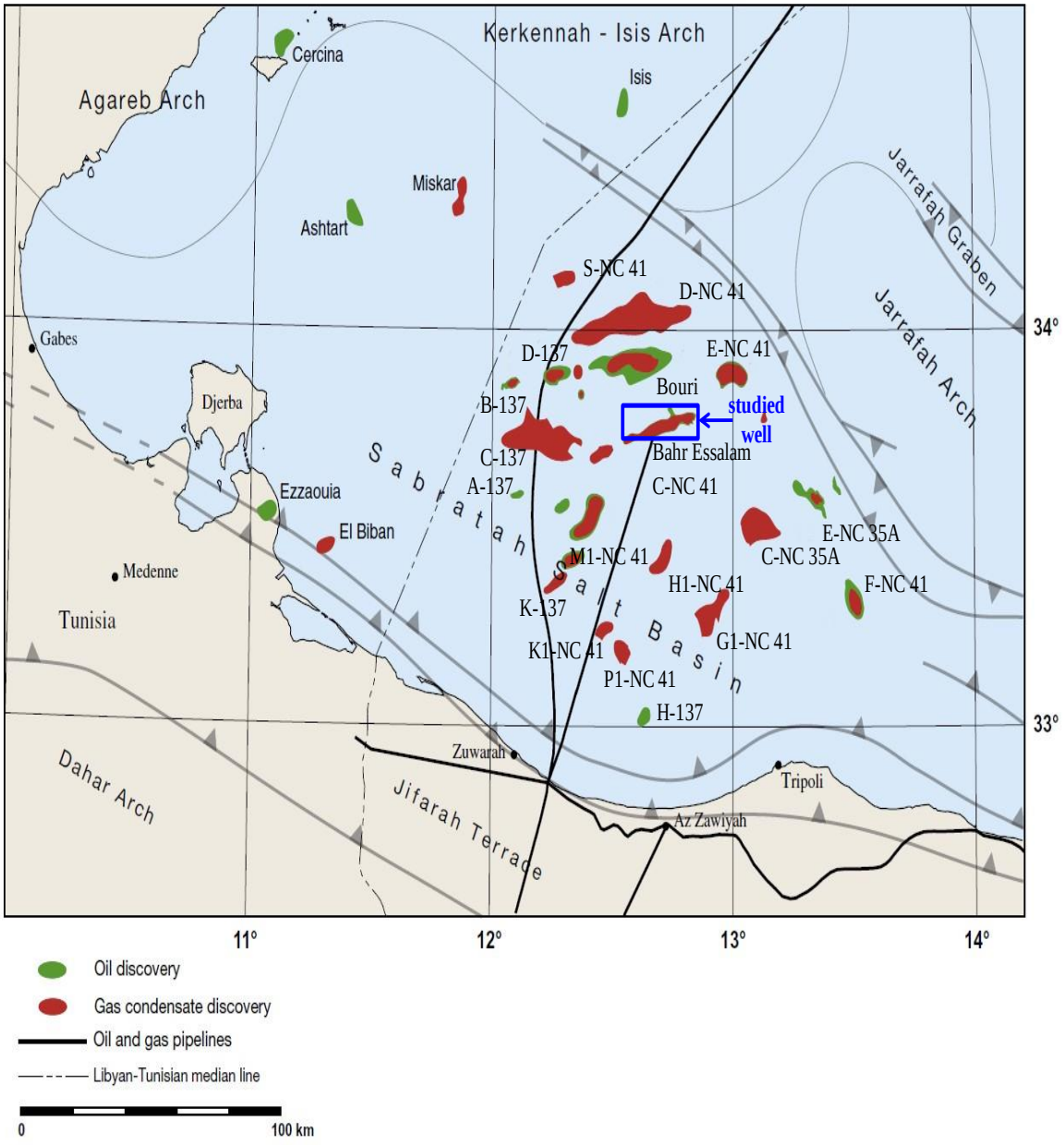

Fig. 1.7: Well location map of the Sabratah Basin showing the location of the offshore Well C-NC 41 (modified after Bishop, 1988; Bailey et al., 1989; Sbeta, 1990; Anketell and Mriheel, 2000 and Racey et al., 2001).

1.3.1.1. Lower Member

The Lower Member of the Al Jurf Formation is rich in Maastrichtian planktonic microfaunas (Hallett, 2002). The shales of the member are organically rich and have minor source potential (Hallett, 2002). In some areas volcanic rocks are present in this member (Hallett, 2002). The member correlates with the lower El Haria shales in Tunisia, and in Libya it is equivalent to the Lower Tar Member, and to the Kalash Formation of the Sirt Basin (Hammuda *et al.,* 1985).

1.3.1.2. Upper Member

The faunal richness decreases in the Upper Member of the Al Jurf Formation, but evidence from Well D-NC 41 and elsewhere proves a continuous sequence of planktonic index fossils from low in the Danian to the top of the Thanetian (Hallett, 2002). The Upper Member consists of silty marls, black shales and shaly sandstones (Hallett, 2002). The black shales represent a potential source rock for the overlying Farwah Group reservoirs, although the Early Eocene shales are a more likely candidate (Hammuda *et al.,* 1985). The member is age equivalent to both the Zimam and Shurfah Formations of northwest Libya, and to the upper part of the El Haria Formation plus the Tselja Formation in Tunisia (Hallett, 2002).

1.3.2. Objectives

The above statements suggest that the black shales of the Lower Member of the Al Jurf Formation have minor source potential, while the black shales of the Upper Member represent a potential source rock for the overlying Farwah Group reservoirs. Thus, the objective of the current work is to conduct a petrographic and geochemical assessment of all black shales of the Al Jurf Formation in the offshore Well C-NC 41 (Fig. 1.7), to obtain the following information:

1) Source rock quality.
2) Organic matter type.
3) Thermal maturity.
4) Organic matter origin.
5) Depositional environment.

6) Paleoclimate.

7) Paleooxygenation condition.

8) Paleosalinity.

9) Paleoweathering.

10) Paleotectonic setting.

1.3.3. Previous Work

It is worthy to note that the published data on the Al Jurf Formation in the Sabratah Basin are insufficient. Very limited effort has been given to the Al Jurf Formation in the basin. In this respect the detailed characteristics of their formation are given, especially in the absence of many published works on the subject.

1.3.4. Stratigraphy

The total thicknesses of the lower and upper members of the Al Jurf Formation in the offshore Well C-NC 41 are 205 and 209 m, respectively (Fig. 1.8). The formation consists of shales, shaly sandstones, marls and limestones. There are two black shale units in the Lower Member, whereas the Upper Member contains one black shale unit. In the studied well, the Al Jurf Formation is overlain by the Hallab and Bilal formations of the Farwah Group (Early Eocene), while the lower boundary of the formation is conformable with the underlying Abu Isa Formation (Late Cretaceous).

1.3.5. Methodology

1.3.5.1. Sampling

It should be noted that the data used in the present study were taken from the AGIP Company. Twenty samples were selected from the black shales (Fig. 1.8). It should be noted that, all the analyses I will mention below were conducted in the laboratory of Chemostratigraphy and Organic Geochemistry (LGQM), State University of Rio de Janeiro (UERJ), Brazil.

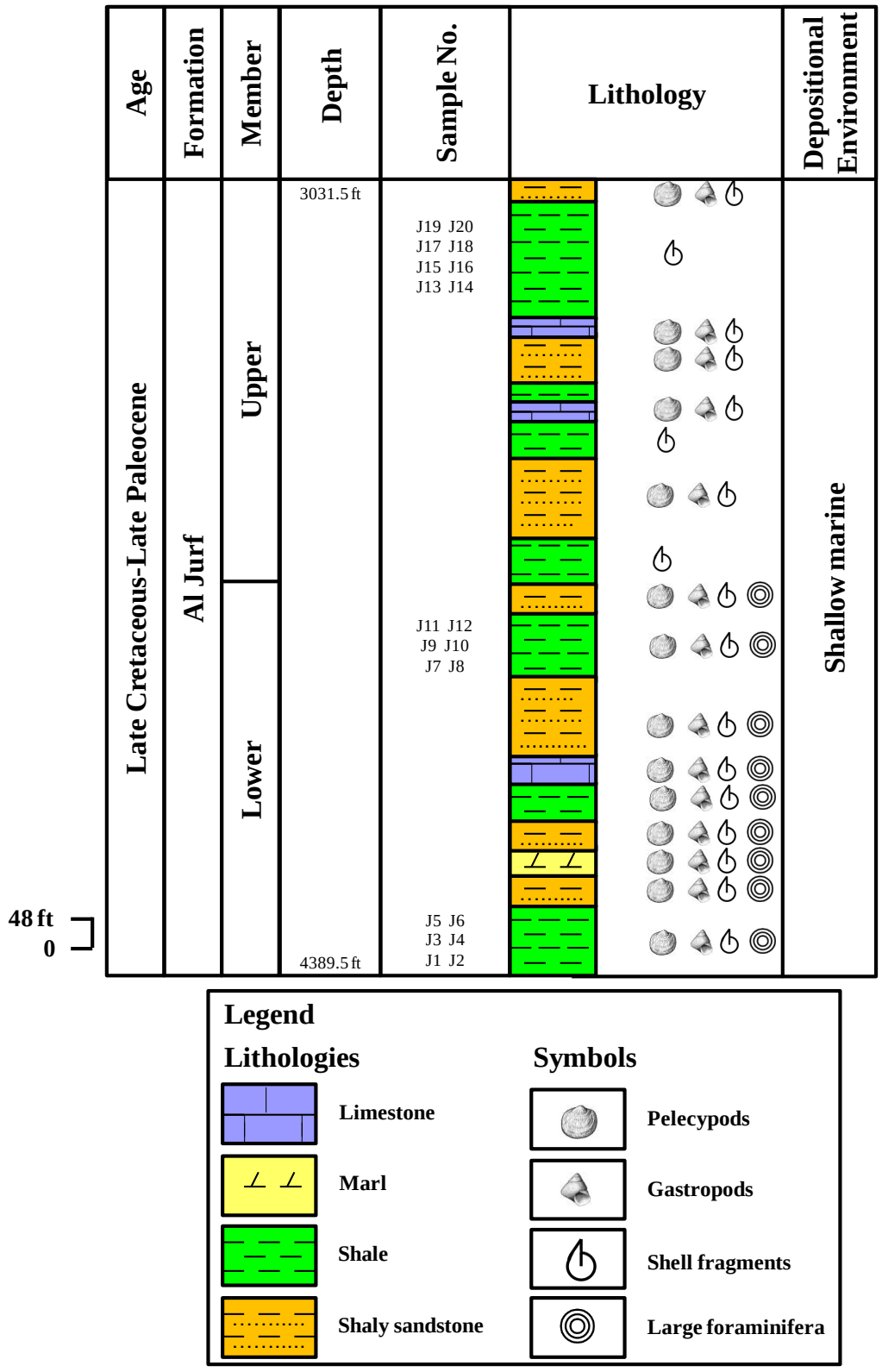

Fig. 1.8: Lithostratigraphic column of the Al Jurf Formation in the offshore Well C-NC 41.

1.3.5.2. Organic Petrography

The organic petrographic microscope was used in the current work (Fig. 1.9). Maceral analyses used reflected light and where necessary, reflected fluorescent light with a 10× ocular and 50× oil immersion objective. At least 500 points on each sample were counted using mechanical stage steps and a point counter. All counting included maceral and mineral matter. The results are expressed in volume percentage of each component (vol. %) for macerals. Random vitrinite reflectance (VR) measurements were made by calibrating against two sets of reference standards (Gadolinium-Gallium-Granat 0. 91–59, R 546 nm, oil = 1.674 %, and glass, R 546, oil = 0.576 %) using monochromatic (546) non-polarized light in conjunction with a 10× ocular and 40× oil immersion objective. The reflectance measurements were carried out mostly on vitrinite, although other macerals were used when vitrinite was absent. Reflectance is mainly carried out on solid/bitumen if available or fluorescing material like spore, etc. Organic matter in these samples occurs as a complex mixture. The identification of indigenous vitrinite populations is based upon petrographical observations and the distribution of reflectance data. The use of interpretive step to determine the indigenous vitrinite population can lead to different results when compared to whole rock analyses.

1.3.5.3. Inductively Coupled Plasma-Mass Spectrometry (ICP-MS)

A Thermo Fisher (X-Series II) inductively coupled plasma mass spectrometer (ICP-MS, Fig. 1.10) was used in this study. Prior to ICP-MS analysis, the samples were digested using a Milestone UltraClave microwave high pressure reactor. A Milli-Q A10 Ultra-pure water system with resistivity of 18.2 MΩ.cm was used for ultra-pure water preparation. A Milestone acid purification system and Milestone acid cleaning system was used for further purification of guaranteed reagents (GR) HNO_3. Five concentrations level of (0, 1, 10, 50, and 100 µg/l), diluted from 100 µg/ml standard solution (Inorganic Ventures, CCS1 & CCS4), were used. The standard stock solution of ^{103}Rh (10 µg/ml), diluted from 1000 µg/ml Rh standard solution, was used for preparation of internal standard solution (10 µg/l). A standard solution containing the multi-elements Li, Co, In, and U (1 µg/l), diluted from 100 µg/ml (THM-TS-1, Inorganic Ventures), was used as a tuning solution. All standards were used without further purification and prepared in 2 % HNO_3 (65-68 %;

volume/volume percent, v/v). The metal-oxide-semiconductor (MOS) reagent HNO_3 (70 %) and MOS reagent HF (≥ 40 %) were used for sample digestion. The MOS reagent HNO_3 (5 mol/L; 2 mol/L), GR HCl (1 mol/L, 1.75 mol/L) and Bio-Rad AG50W-x8 cation exchange resin (200- 400mesh) were used for element separation. Ultra-pure (99.999 % pure) Ar was used as the cooling, auxiliary, and nebulizer gas.

1.3.5.4. Source Rock Analyzer (SRA)

A source rock analyzer (SRA, Fig. 1.11) was used to perform pyrolysis. This method permits rapid evaluation of the organic matter type and the thermal maturity of the organic matter. All the samples were crushed to fine powder (< 150μm) and screened by Weatherford source rock analyzer (equivalent to Rock-Eval equipment) which pyrolyzed the samples to 600 °C in a helium atmosphere. The source rock hydrocarbon potential (S_1, S_2 and S_3) and thermal maturity (T_{max}) of the shale samples were determined. All samples were treated with HCl to remove $CaCO_3$ and subsequently 100mg of each sample was subjected to TOC analysis using a multi N/C 3100 analyzer produced by Analytik Jena. Other parameters such as production index (PI), hydrogen index (HI) and oxygen index (OI) were calculated from the Rock-Eval pyrolysis data and the TOC values.

1.3.5.5. Gas Chromatography-Mass Spectrometry (GC-MS)

Gas chromatography-mass spectrometry (GC-MS, Fig. 1.12) analysis was performed on the hydrocarbon fraction. Agilent GC-MS HP 5975B MSD mass spectrometer with gas chromatograph coupled to its ion source, operating at 70 eV ionization voltage, 100 milliampere filament emission current, 230 °C interface temperature, was used for detail analysis of the saturated component of the extractable organic matter. The HP-5MS column GC instrument (column length: 30 m, internal diameter: 0.32 mm, film thickness: 0.25 μm) was programmed from 40 to 300 °C at 4 °C/min, and then held for 30 min at 300 °C.

Fig. 1.9: Organic Petrographic Microscope.

Fig. 1.10: Inductively coupled plasma-mass spectrometry instrument.

Fig. 1.11: Source rock analyzer.

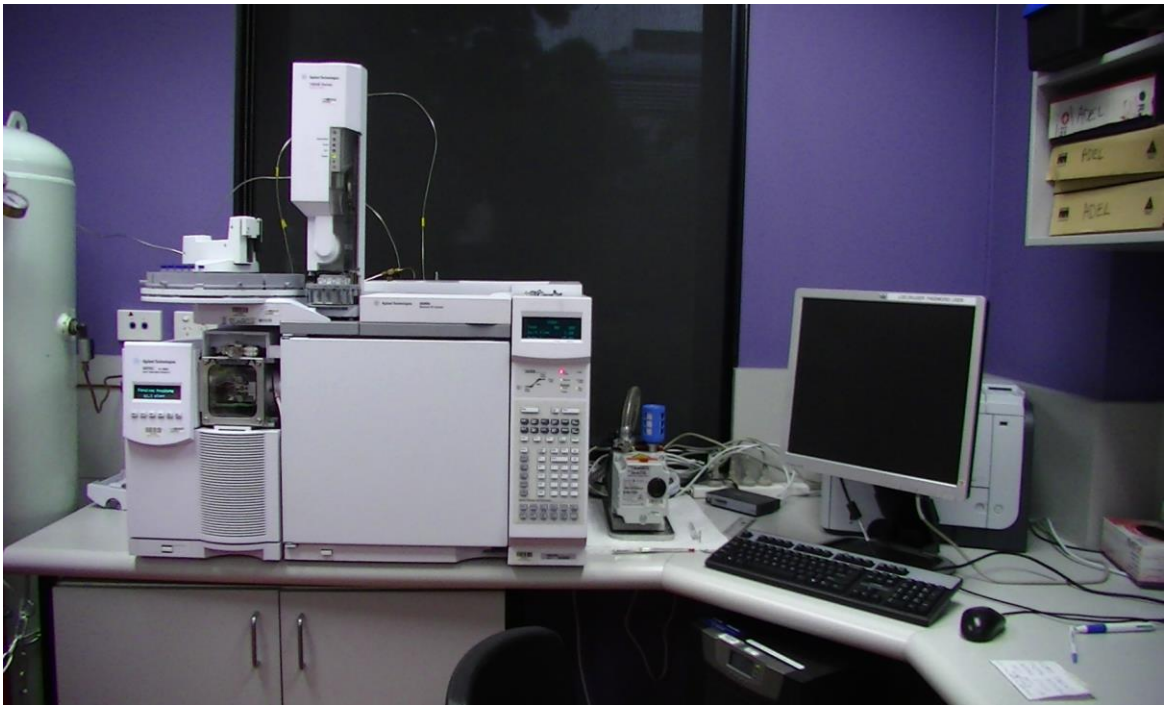

Fig. 1.12: Gas chromatography-mass spectrometry instrument.

CHAPTER TWO
ELEMENTAL GEOCHEMISTRY

2.1. Introduction

Elemental geochemical parameters and their ratios are widely used to assess paleoenvironmental conditions, ancient water compositions, paleotectonic settings, and the provenance of sedimentary rocks (Sun *et al.,* 2012; Shaltami *et al.,* 2016 and Claes *et al.,* 2019). The composition of source rocks, degree of weathering in the source area, depositional setting and post-depositional modifications are some of the factors that influence the chemical and mineralogical composition of sedimentary rocks (Nesbitt *et al.,* 1980, Roser and Korsch, 1988 and McLennan *et al.,* 1993). In recent years, the distribution of major and trace elements, including those of rare earth elements in coal and shale has extensively been analyzed and described (Liu and Lee, 2001; Dai *et al.,* 2008; Baioumy *et al.,* 2014 and Dianshi *et al.,* 2019).

The aim of this chapter is to define the geochemical characteristics of the black shales of the Al Jurf Formation in the offshore Well C-NC 41 based on their major oxides and trace elements and to discuss the paleoweathering, paleoclimate, depositional environment, paleosalinity, paleo-oxygenation, and paleotectonic setting of the shales. The data of major oxides and trace elements are given in Tables (2.1-2.2).

Major oxides data showed that SiO_2 content ranks the most abundant content were ranged between (64.85-70.57 wt %) in all black shales. Al_2O_3 (7.62-12.59 wt %) is the second most abundant oxide. The rest of the oxides of (TiO_2, Fe_2O_3, MnO, MgO, CaO, Na_2O, K_2O and P_2O_5) have concentrations less than of 3 wt %. Generally, the black shales are enriched in high field strength elements (Zr, Hf, Nb, Ta, Th and U) and heavy metals (Ga, B, V, Cr, Ni, Co, Cu and Zn), while they contains low concentrations of low field strength elements (Rb) and pseudo-lanthanides (Sc).

Table 2.1: Chemical analysis data (major oxides in wt % and trace elements in ppm) of the black shales of the Lower Member of the Al Jurf Formation

Oxides and Elements	Sample No.											
	J1	J2	J3	J4	J5	J6	J7	J8	J9	J10	J11	J12
SiO_2	65.65	64.85	67.77	67.42	66.48	65.91	66.17	65.61	65.96	66.18	69.24	70.57
TiO_2	0.28	0.41	0.25	0.15	0.11	0.17	0.20	0.41	0.35	0.28	0.14	0.27
Al_2O_3	12.59	11.42	10.76	10.20	10.09	10.00	10.21	12.10	9.23	9.27	7.62	9.92
Fe_2O_3	0.81	0.94	1.24	1.54	2.45	2.55	2.66	0.73	2.40	2.30	1.10	1.11
MnO	0.07	0.07	0.07	0.07	0.07	0.07	0.07	0.07	0.07	0.07	0.07	0.07
MgO	1.98	1.94	2.03	2.14	1.95	2.12	2.04	1.99	2.66	2.62	3.07	2.29
CaO	1.16	1.00	0.67	0.86	0.92	1.17	1.04	0.90	0.77	0.74	1.22	1.10
Na_2O	0.28	0.30	0.18	0.27	0.33	0.30	0.25	0.38	0.54	0.42	0.43	0.55
K_2O	0.40	0.29	0.54	0.55	0.66	0.48	0.59	0.41	0.56	0.53	0.38	0.50
Cl	0.05	0.05	0.05	0.05	0.05	0.05	0.05	0.05	0.05	0.05	0.05	0.05
P_2O_5	0.25	0.23	0.18	0.31	0.30	0.29	0.29	0.21	0.26	0.24	0.24	0.28
Rb	10.70	9.43	9.00	8.33	10.95	11.87	9.49	9.30	9.42	10.91	15.03	15.95
Ga	7.37	6.10	5.67	5.00	7.62	8.54	6.16	5.97	6.09	7.58	11.70	12.62
B	36.92	34.65	28.22	33.54	35.17	37.49	34.71	35.45	34.64	32.81	50.44	56.66
V	162.53	171.51	160.00	186.59	158.74	150.50	172.59	169.21	168.08	160.89	172.93	180.44
Cr	38.70	31.59	43.77	30.13	40.53	31.87	36.98	30.83	30.41	29.58	43.94	52.92
Ni	54.96	63.30	57.83	55.17	35.54	33.15	55.33	58.14	29.28	29.90	55.44	54.85
Co	7.17	8.23	8.31	7.73	4.16	3.10	7.89	8.55	2.38	2.86	8.06	7.80
Cu	93.34	93.61	97.88	93.42	94.78	95.30	107.53	111.72	79.96	85.06	89.54	90.16
Zn	38.52	35.02	34.48	35.40	37.40	33.52	46.73	42.93	25.36	24.19	37.99	39.56
Zr	178.17	179.19	178.99	176.13	164.76	165.48	182.53	181.89	207.70	207.06	181.21	179.65
Hf	2.76	2.69	2.81	2.40	2.38	2.21	3.10	2.81	3.00	2.88	2.73	2.82
Nb	7.26	7.80	7.37	6.23	6.85	6.63	7.71	7.42	7.52	7.58	7.47	7.36
Ta	1.22	1.36	1.27	1.32	1.11	1.03	1.39	1.30	1.37	1.33	1.27	1.34
Th	8.55	8.66	8.36	8.75	6.55	7.84	9.05	7.71	7.13	7.00	8.55	8.50
U	10.76	10.16	10.05	9.12	8.88	9.00	9.67	10.59	7.32	8.05	8.38	7.96
Sc	22.54	22.63	22.24	24.41	22.02	20.54	23.49	22.72	23.05	22.22	20.64	20.90

Table 2.2: Chemical analysis data (major oxides in wt % and trace elements in ppm) of the black shales of the Upper Member of the Al Jurf Formation

Oxides and Elements	Sample No.							
	J13	J14	J15	J16	J17	J18	J19	J20
SiO_2	67.46	65.89	66.43	65.96	66.12	65.59	66.58	66.00
TiO_2	0.28	0.36	0.13	0.19	0.22	0.43	0.09	0.15
Al_2O_3	10.92	11.59	10.07	10.00	10.19	12.08	10.12	10.06
Fe_2O_3	1.10	0.36	2.47	2.57	2.68	0.75	2.44	2.53
MnO	0.09	0.09	0.09	0.09	0.09	0.09	0.09	0.09
MgO	1.89	2.05	1.93	2.10	2.02	1.97	1.97	2.14
CaO	0.77	0.87	0.94	1.19	1.06	0.92	0.90	1.15
Na_2O	0.60	0.62	0.78	0.81	0.71	0.66	0.57	0.50
K_2O	0.51	0.49	0.68	0.50	0.61	0.43	0.64	0.46
Cl	0.03	0.03	0.03	0.03	0.03	0.03	0.03	0.03
P_2O_5	0.33	0.34	0.28	0.27	0.27	0.19	0.32	0.32
Rb	11.70	12.78	9.78	9.02	13.90	12.75	8.64	8.21
Ga	8.37	9.45	6.45	5.69	10.57	9.42	5.31	4.88
B	46.92	44.00	37.11	31.24	46.12	47.97	29.86	28.43
V	142.15	137.29	158.76	150.52	172.61	169.23	158.70	150.48
Cr	27.44	33.52	40.49	30.84	36.94	30.79	40.57	31.92
Ni	47.67	49.41	35.57	33.18	55.38	58.17	35.51	33.12
Co	6.08	6.29	4.12	3.06	7.85	8.51	4.20	3.14
Cu	113.57	112.25	94.82	95.33	107.56	111.75	94.75	95.27
Zn	43.71	47.62	37.43	33.55	46.76	42.96	37.37	33.49
Zr	219.75	214.67	164.72	165.44	182.49	181.85	164.80	165.52
Hf	3.36	3.43	2.42	2.25	3.14	2.85	2.34	2.17
Nb	9.61	9.10	6.89	6.67	7.75	7.46	6.81	6.59
Ta	1.53	1.60	1.08	1.00	1.36	1.27	1.14	1.06
Th	8.57	8.50	6.56	7.87	9.06	7.74	6.50	7.81
U	9.87	10.00	7.12	7.50	9.63	10.12	8.14	7.58
Sc	20.26	19.08	22.04	20.56	23.44	22.74	22.00	20.52

2.2. Statistical Treatments

Using the SPSS© program, three types of statistical analyses were performed in this chapter. These analyses are descriptive statistics (Table 2.3), Pearson's correlation coefficient (correlation analysis, Table 2.4 and Figs. 2.1-2.2) and factor analysis (Table 2.5 and Fig. 2.3). The correlation analysis shows that SiO_2 does not demonstrate any confident coherence to any of the analyzed major oxides (Table 2.4 and Fig. 2.1), indicating the abundance of free silica (quartz) in the studied black shales. There are no strong correlations between most major oxides, showing a significant difference in the minerals carrying these oxides. The inverse correlation between SiO_2 and Al_2O_3 suggests that the total amount of clay minerals in the black shales is mainly controlled by sedimentary environment. Moreover, the absence of strong correlations among some heavy metals (Table 2.4 and Fig. 2.2) can be interpreted to their derivation from different sources and/or remobilization during chemical weathering. Additionally, most high field strength elements are mutually correlated (Table 2.4 and Fig. 2.2), suggesting that these elements are controlled by accessory minerals.

Approximately 63.9 % of the total variables are explained by three factors. The explanation of these factors is as follows:

Factor one (F1): It accounts for about 28.38 % of the total variables. It shows positive loading for TiO_2, Al_2O_3, Ga, B, Ni, Co, Cu, Zn, Zr, Hf, Nb, Ta, Th and U. It also displays negative loading for Fe_2O_3. This factor is important in determining minerals that carry heavy metals and high field strength elements.

Factor two (F2): It accounts for 19.78 % of the total variables. It loads positively for MnO, Na_2O and K_2O. It also displays negative loading for Cl and V. This factor is important in identifying clay mineral types.

Factor three (F3): It accounts for 15.74 % of the total variables. It has only positive loading for SiO_2. This factor is important in determining free silica content.

Table 2.3: Descriptive statistics the studied black samples (major oxides in wt. % and trace elements in ppm)

Oxides and elements	N	Minimum	Maximum	Mean	Std. Deviation
SiO_2	20	64.85	70.57	66.59	1.34
TiO_2	20	0.09	0.43	0.24	0.11
Al_2O_3	20	7.62	12.59	10.42	1.14
Fe_2O_3	20	0.36	2.68	1.74	0.82
MnO	20	0.07	0.09	0.08	0.01
MgO	20	1.89	3.07	2.15	0.30
CaO	20	0.67	1.22	0.97	0.16
Na_2O	20	0.18	0.81	0.47	0.19
K_2O	20	0.29	0.68	0.51	0.10
Cl	20	0.03	0.05	0.04	0.01
P_2O_5	20	0.18	0.34	0.27	0.05
Ga	20	4.88	12.62	7.53	2.25
Rb	20	8.21	15.95	10.86	2.25
B	20	28.22	56.66	38.12	7.88
V	20	137.29	186.59	162.69	12.46
Cr	20	27.44	52.92	35.69	6.48
Ni	20	29.28	63.30	46.55	11.73
Co	20	2.38	8.55	5.97	2.30
Cu	20	79.96	113.57	97.88	9.58
Zn	20	24.19	47.62	37.70	6.36
Zr	20	164.72	219.75	182.10	17.11
Hf	20	2.17	3.43	2.73	0.37
Nb	20	6.23	9.61	7.40	0.80
Ta	20	1.00	1.60	1.27	0.16
Th	20	6.50	9.06	7.96	0.83
U	20	7.12	10.76	9.00	1.16
Sc	20	19.08	24.41	21.90	1.34

Table 2.4: Correlation matrix of the studied shales

Oxides and elements	SiO_2	TiO_2	Al_2O_3	Fe_2O_3	MnO	MgO	CaO	Na_2O	K_2O	Cl	P_2O_5	Ga	Rb	B	V	Cr	Ni	Co	Cu	Zn	Zr	Hf	Nb	Ta	Th	U	Sc
SiO_2	1.00																										
TiO_2	-0.31	1.00																									
Al_2O_3	-0.49	0.59	1.00																								
Fe_2O_3	-0.17	-0.65	-0.54	1.00																							
MnO	-0.21	-0.10	0.15	0.13	1.00																						
MgO	0.42	-0.09	-0.76	0.05	-0.38	1.00																					
CaO	0.07	-0.29	-0.15	0.15	0.04	0.12	1.00																				
Na_2O	-0.02	-0.01	-0.09	0.17	0.82	-0.05	0.11	1.00																			
K_2O	0.10	-0.59	-0.30	0.65	0.25	-0.18	-0.32	0.26	1.00																		
Cl	0.21	0.10	-0.15	-0.13	-1.00	0.38	-0.04	-0.82	-0.25	1.00																	
P_2O_5	0.07	-0.49	-0.18	0.31	0.37	-0.16	0.13	0.23	0.41	-0.37	1.00																
Ga	0.54	0.13	-0.19	-0.31	0.00	0.34	0.30	0.24	-0.16	0.00	-0.03	1.00															
Rb	0.54	0.13	-0.19	-0.31	0.00	0.34	0.30	0.24	-0.16	0.00	-0.03	0.95	1.00														
B	0.53	0.25	-0.06	-0.44	0.09	0.22	0.23	0.33	-0.19	-0.09	0.02	0.93	0.93	1.00													
V	0.31	0.06	-0.16	-0.05	-0.52	0.26	0.08	-0.30	-0.08	0.52	-0.40	0.12	0.12	0.19	1.00												
Cr	0.69	-0.35	-0.25	-0.05	-0.21	0.14	0.24	-0.08	0.22	0.21	-0.08	0.44	0.44	0.34	0.30	1.00											
Ni	0.18	0.45	0.44	-0.70	-0.22	-0.19	0.04	-0.32	-0.48	0.22	-0.41	0.28	0.28	0.40	0.49	0.21	1.00										
Co	0.25	0.39	0.40	-0.67	-0.21	-0.16	0.01	-0.30	-0.39	0.21	-0.41	0.32	0.32	0.43	0.52	0.28	0.98	1.00									
Cu	-0.22	0.32	0.59	-0.35	0.46	-0.60	-0.09	0.18	-0.05	-0.46	0.07	0.12	0.12	0.26	-0.27	-0.24	0.47	0.48	1.00								
Zn	0.05	0.14	0.44	-0.36	0.35	-0.47	0.17	0.16	0.01	-0.35	0.18	0.37	0.37	0.49	-0.03	0.17	0.60	0.64	0.85	1.00							
Zr	0.02	0.55	0.07	-0.39	0.01	0.25	-0.54	0.09	-0.13	-0.01	0.07	0.25	0.25	0.32	-0.22	-0.36	0.08	0.06	0.21	0.07	1.00						
Hf	0.06	0.58	0.23	-0.45	0.04	0.05	-0.40	0.08	-0.08	-0.04	-0.05	0.41	0.41	0.49	-0.05	-0.07	0.43	0.43	0.47	0.47	0.85	1.00					
Nb	0.01	0.52	0.25	-0.48	0.21	-0.06	-0.35	0.17	-0.18	-0.21	0.11	0.37	0.37	0.46	-0.37	-0.18	0.30	0.27	0.53	0.46	0.84	0.89	1.00				
Ta	0.12	0.57	0.21	-0.55	-0.07	0.07	-0.46	-0.07	-0.17	0.07	0.06	0.32	0.32	0.43	0.08	-0.13	0.50	0.48	0.38	0.40	0.86	0.92	0.83	1.00			
Th	0.20	0.26	0.18	-0.40	-0.14	-0.02	0.27	-0.25	-0.46	0.14	-0.04	0.31	0.31	0.37	0.26	0.02	0.73	0.68	0.36	0.48	0.24	0.46	0.36	0.51	1.00		
U	-0.26	0.53	0.74	-0.64	-0.18	-0.44	-0.14	-0.45	-0.43	0.18	-0.30	0.08	0.08	0.13	0.05	-0.15	0.75	0.72	0.64	0.57	0.23	0.47	0.43	0.47	0.54	1.00	
Sc	-0.22	0.08	0.12	0.18	-0.36	-0.10	-0.25	-0.33	0.19	0.36	-0.38	-0.34	-0.34	-0.27	0.75	-0.08	0.29	0.31	-0.11	-0.08	-0.16	-0.02	-0.34	0.03	0.04	0.20	1.00

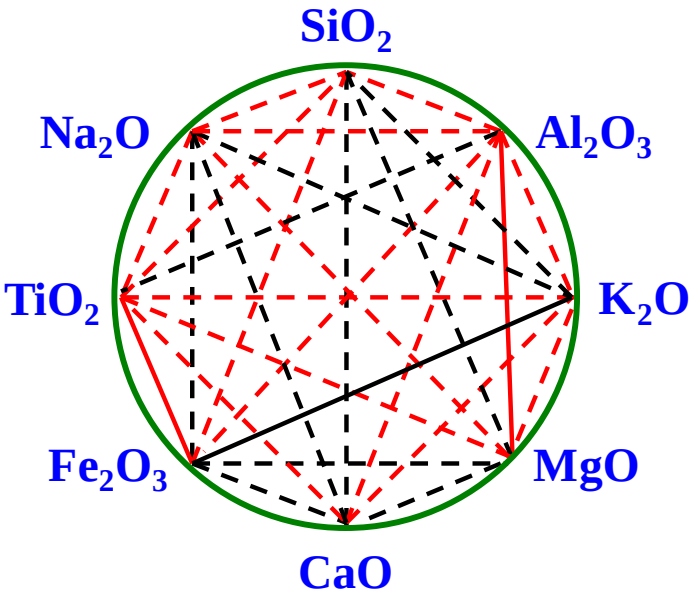

Fig. 2.1: Correlations among the analyzed major oxides in the black shale samples (intensity of lines corresponds to the strength of the correlation coefficient (< 0.4 to > 0.8)) (red line means inverse relation).

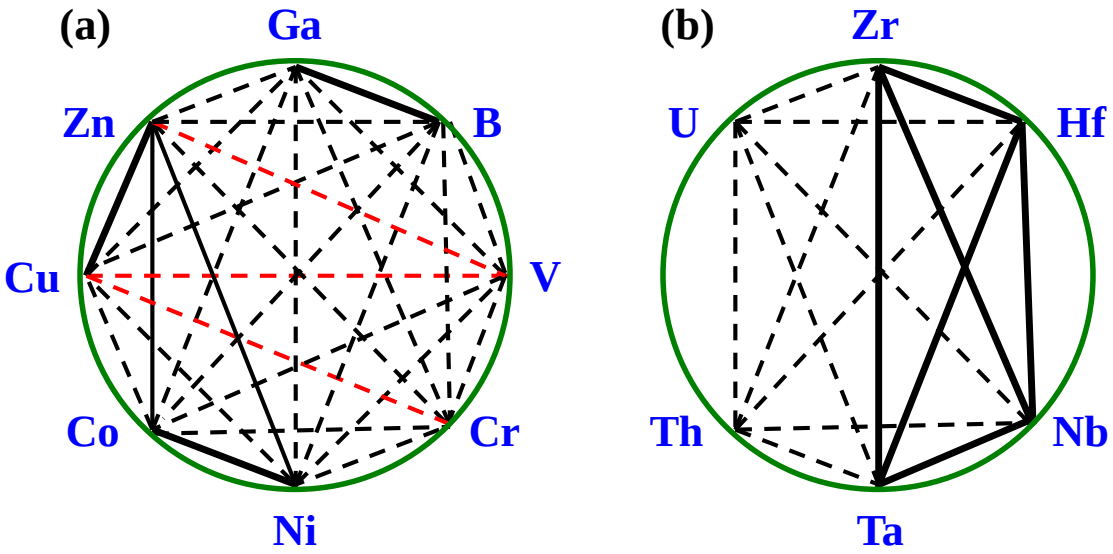

Fig. 2.2: Correlations among the analyzed trace elements (a- heavy metals and b- high field strength elements) in the black shale samples (intensity of lines corresponds to the strength of the correlation coefficient (< 0.4 to > 0.8)) (red line means inverse relation).

Table 2.5: Factor analysis of major oxides and trace elements of the studied black shale

Eigenvalue	7.95	5.54	4.41
% of Variance	28.38	19.78	15.74
Cumulative %	28.38	48.16	63.90
Factor	1	2	3
SiO_2	0.10	-0.33	0.75
TiO_2	0.67	-0.06	-0.34
Al_2O_3	0.61	0.20	-0.56
Fe_2O_3	-0.78	0.18	0.08
MnO	0.03	0.92	0.09
MgO	-0.16	-0.44	0.57
CaO	-0.14	-0.10	0.36
Na_2O	-0.03	0.74	0.38
K_2O	-0.44	0.64	0.14
Cl	-0.03	-0.92	-0.09
P_2O_5	-0.20	0.51	0.25
Ga	0.60	-0.07	0.28
Rb	0.50	-0.07	0.58
B	0.63	0.01	0.55
V	0.08	-0.73	0.06
Cr	-0.05	-0.34	0.56
Ni	0.80	-0.39	-0.14
Co	0.78	-0.39	-0.08
Cu	0.66	0.49	-0.25
Zn	0.69	0.31	0.06
Zr	0.66	0.18	0.06
Hf	0.81	0.12	0.08
Nb	0.76	0.35	0.09
Ta	0.80	0.01	0.03
Th	0.66	-0.25	0.05
U	0.76	-0.15	-0.49
Sc	-0.05	-0.45	-0.46

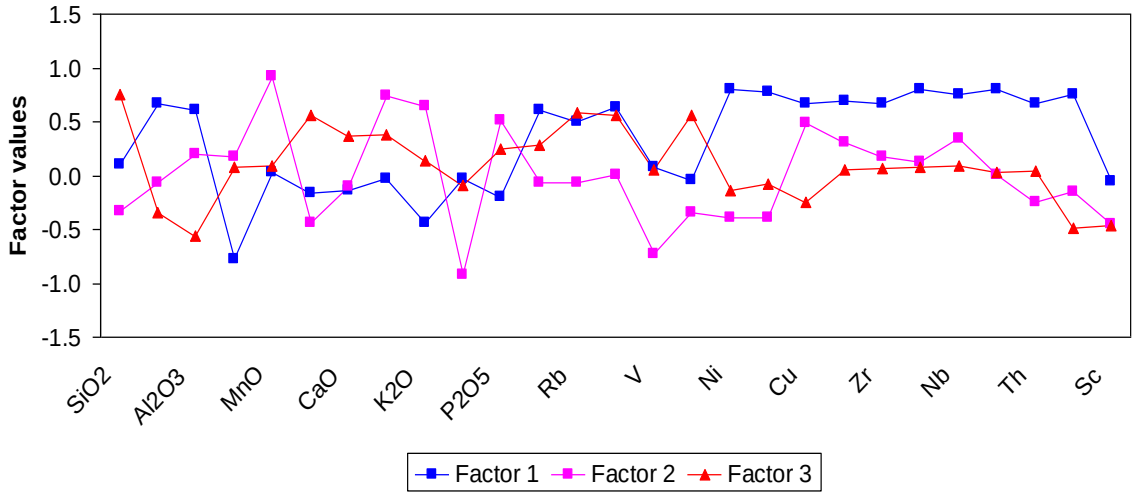

Fig. 2.3: Distribution of the analyzed major oxides and trace elements in factors 1, 2 and 3.

2.3. Clay Minerals

There is no general classification scheme for mineral compositions of source rocks in oil industry at present time (Xiaodong *et al.*, 2011). On the other hand, YaO *et al.*, (2014) divided major minerals in black shales into four categories: 1) Detrital minerals, including quartz, plagioclase, potassium feldspar, etc., 2) Carbonate minerals, including calcite and dolomite, 3) Clay minerals, including illite, smectite, chlorite, kaolinite and mixed-layer minerals, and 4) Other minerals, such as pyrite. Clay minerals can be identified in rocks using several techniques such as X-ray diffraction (XRD), scanning electron microscope (SEM) and geochemistry.

Based on the chemical composition, there are two basic models used to determine clay mineral types: 1) the plot of K versus Th (Morgan and Heier, 1966), and 2) the ternary plot of A-CN-K (Al_2O_3-($CaO+Na_2O$)-K_2O) (Nesbitt and Young, 1982). When these models are used in the current work, smectite, illite, kaolinite, gibbsite, chlorite and mixed layer clays are found to be the main clay minerals in the studied black shales (Figs. 2.4-2.5). This reflects that the black shales were formed in the middle period of digenesis.

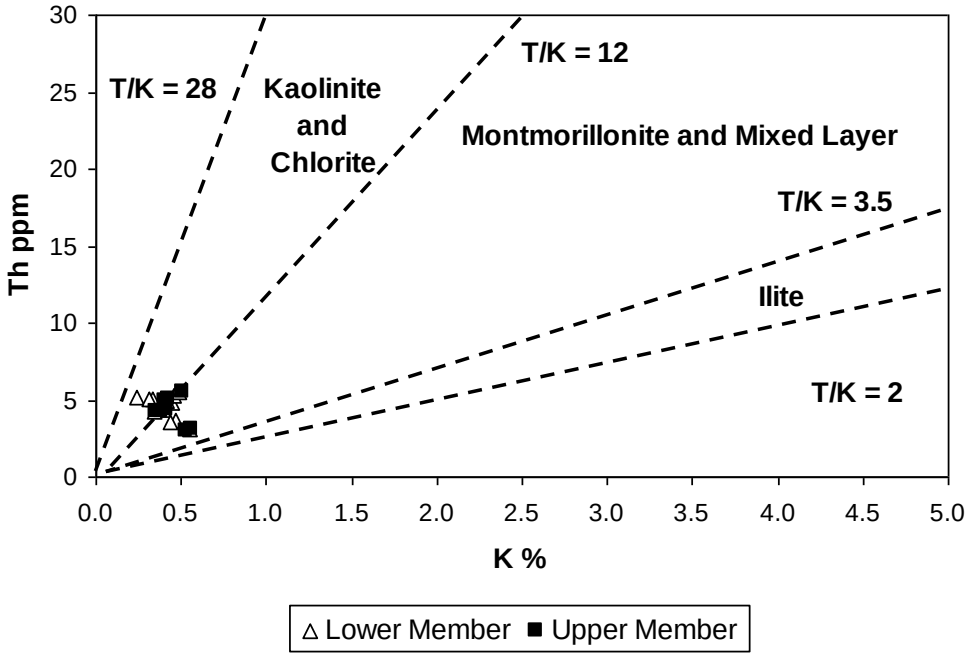

Fig. 2.4: Plot of K vs. Th showing the clay mineral types in the studied black shales (fields after Morgan and Heier, 1966).

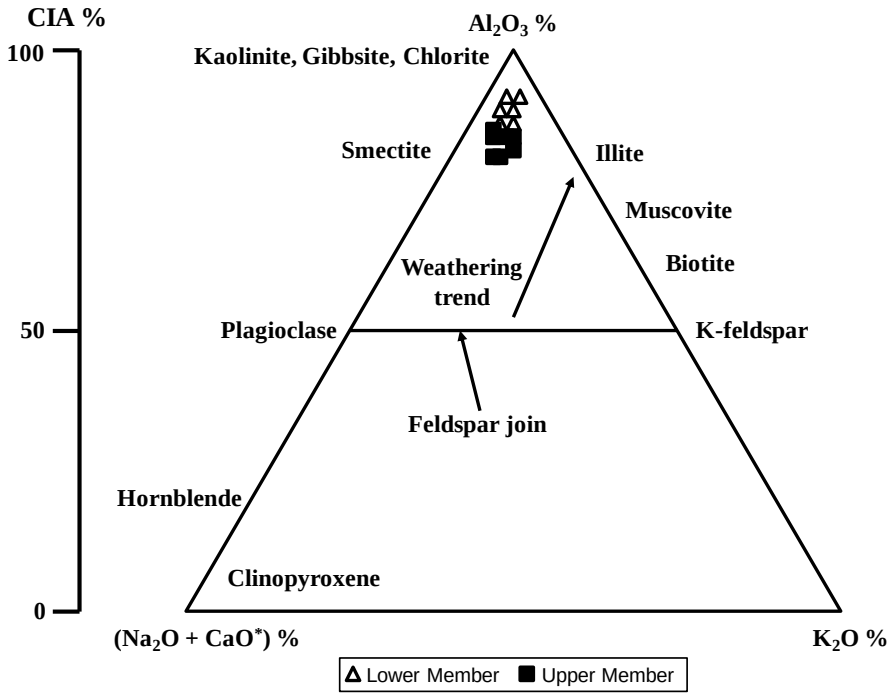

Fig. 2.5: A-CN-K ternary diagram showing the clay mineral types in the studied black shales (fields after Nesbitt and Young, 1982).

2.4. Paleoweathering

There are many indices that are used in evaluating the paleoweathering such as chemical index of alteration (CIA), chemical index of weathering (CIW), modified version of chemical index of weathering (CIW´) and plagioclase index of alteration (PIA) (Nesbitt and Young, 1982; Fedo *et al.,* 1995; Cullers, 2000; Armstrong-Altrin *et al.,* 2004 and Baiyegunhi *et al.,* 2017). The values of indices range from almost 50 in case of fresh rocks to 100 for completely weathered rocks. These indices are calculated as follows:

$$CIA = (Al_2O_3/(Al_2O_3 + CaO^* + Na_2O + K_2O))100$$

$$CIW = (Al_2O_3/(Al_2O_3 + CaO^* + Na_2O))100$$

$$PIA = ((Al_2O_3 - K_2O)/((Al_2O_3 - K_2O) + CaO^* + Na_2O))100$$

$$CIW' = (Al_2O_3/(Al_2O_3 + Na_2O))100$$

Where CaO* is the content of CaO found in silicate fraction. The values of weathering indices in the studied black shales are shown in Tables (2.6- 2.7). Clearly, all indices have values greater than 80 %, suggesting high degree of chemical weathering in the source area.

According to Nesbitt and Young (1984) the plots of PIA versus K_2O/Na_2O, PIA versus total alkalis (K_2O+Na_2O), PIA versus K_2O, PIA versus Na_2O and PIA versus CaO can be used to detect the mobility of elements during the final stage of chemical weathering of previously altered feldspars. In the present study, the K_2O/Na_2O ratio is positively correlated with PIA (Fig. 2.6), while there is an inverse correlation between the total alkalis and PIA (Fig. 2.7). These correlations may be attributed to the presence of K-bearing minerals. Moreover, PIA is negatively correlated with Na_2O (Fig. 2.8), K_2O (Fig. 2.9) and CaO (Fig. 2.10). It is may be the consequence of the presence of carbonates.

Table 2.6: Values of weathering indices (wt. %) of the black shales of the Lower Member of the Al Jurf Formation

Sample No.	CIA	CIW	CIW´	PIA
J1	92.92	95.74	97.82	95.61
J2	92.77	95.01	97.44	94.88
J3	92.28	96.76	98.35	96.60
J4	90.35	94.97	97.42	94.70
J5	88.43	93.86	96.83	93.46
J6	90.25	94.34	97.09	94.07
J7	90.35	95.33	97.61	95.06
J8	91.18	94.09	96.96	93.90
J9	84.91	89.52	94.47	88.92
J10	87.12	91.69	95.67	91.23
J11	86.00	89.86	94.66	89.38
J12	86.11	90.00	94.75	89.54

Table 2.7: Values of weathering indices (wt. %) of the black shales of the Upper Member of the Al Jurf Formation

Sample No.	CIA	CIW	CIW´	PIA
J13	86.46	90.10	94.79	89.66
J14	87.01	90.34	94.92	89.95
J15	81.80	86.59	92.81	85.75
J16	82.51	86.06	92.51	85.43
J17	83.39	87.77	93.49	87.09
J18	87.35	90.15	94.82	89.82
J19	85.04	89.88	94.67	89.27
J20	87.33	90.96	95.27	90.57

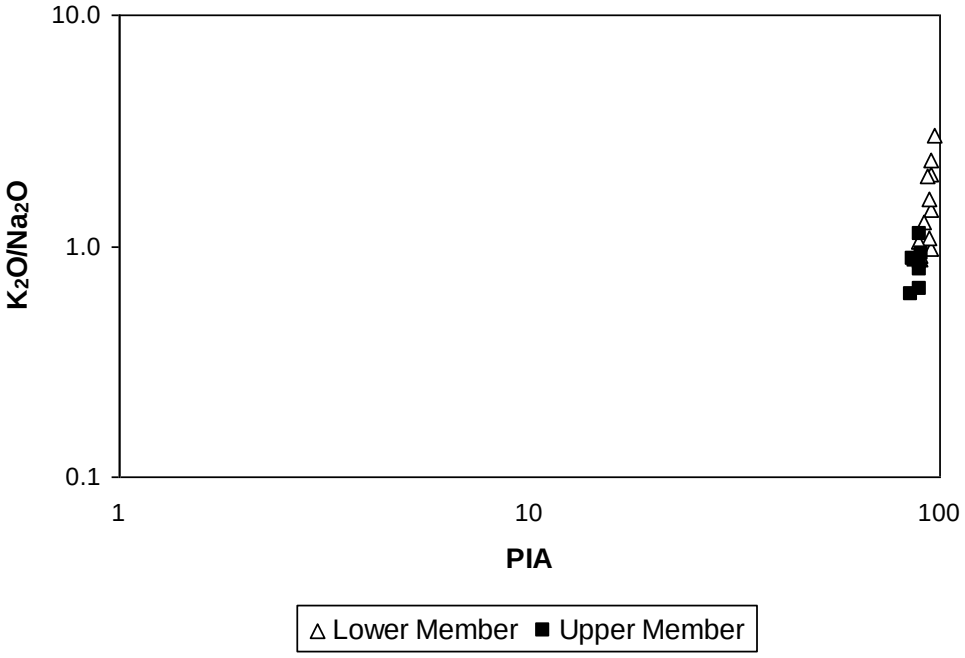

Fig. 2.6: Relationship between PIA and K_2O/Na_2O in the studied black shales.

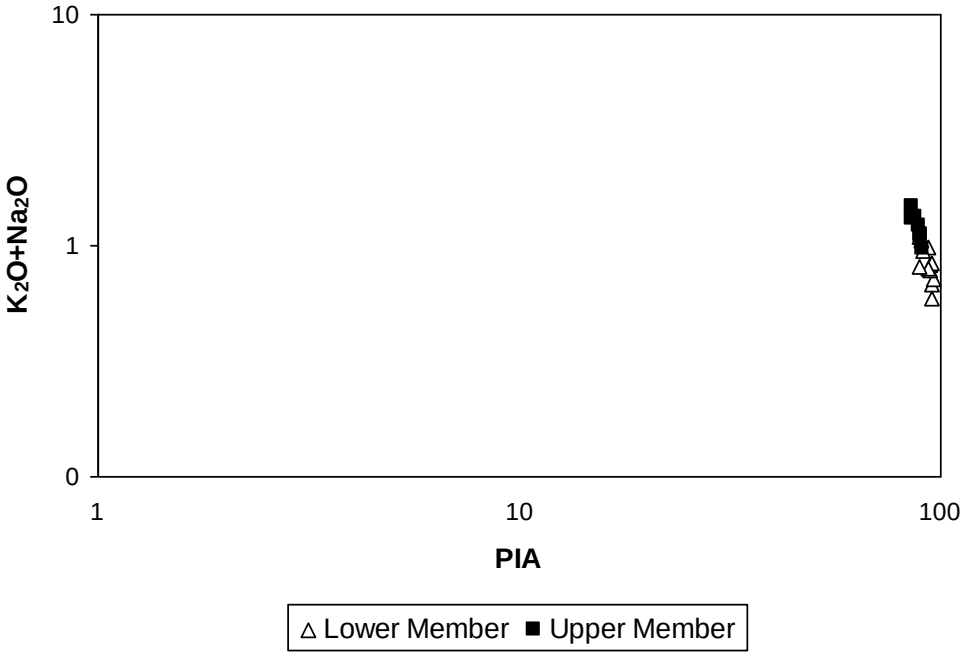

Fig. 2.7: Relationship between PIA and K_2O+Na_2O in the studied black shales.

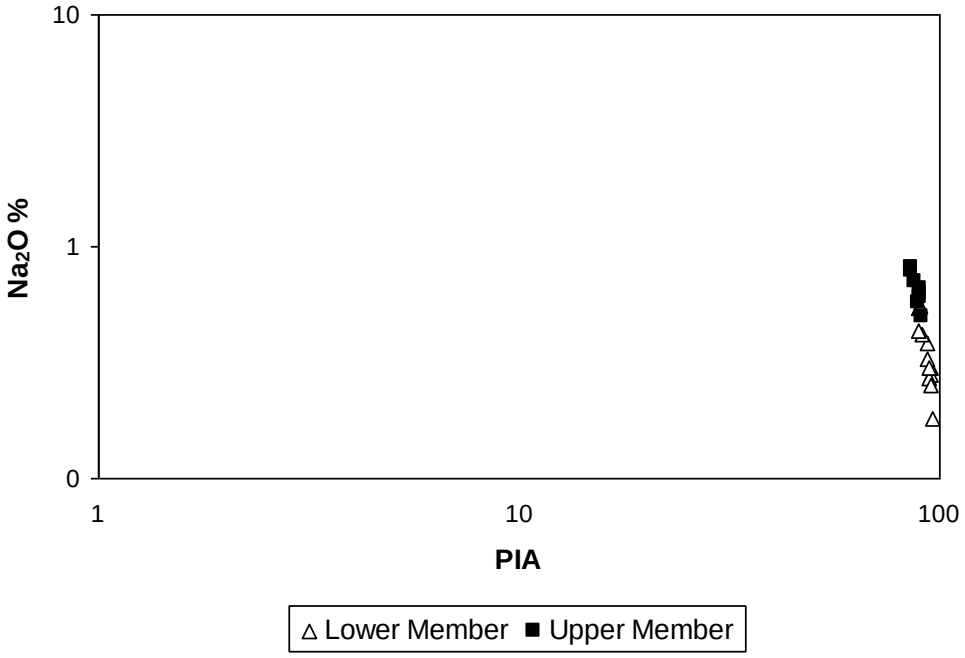

Fig. 2.8: Relationship between PIA and Na_2O in the studied black shales.

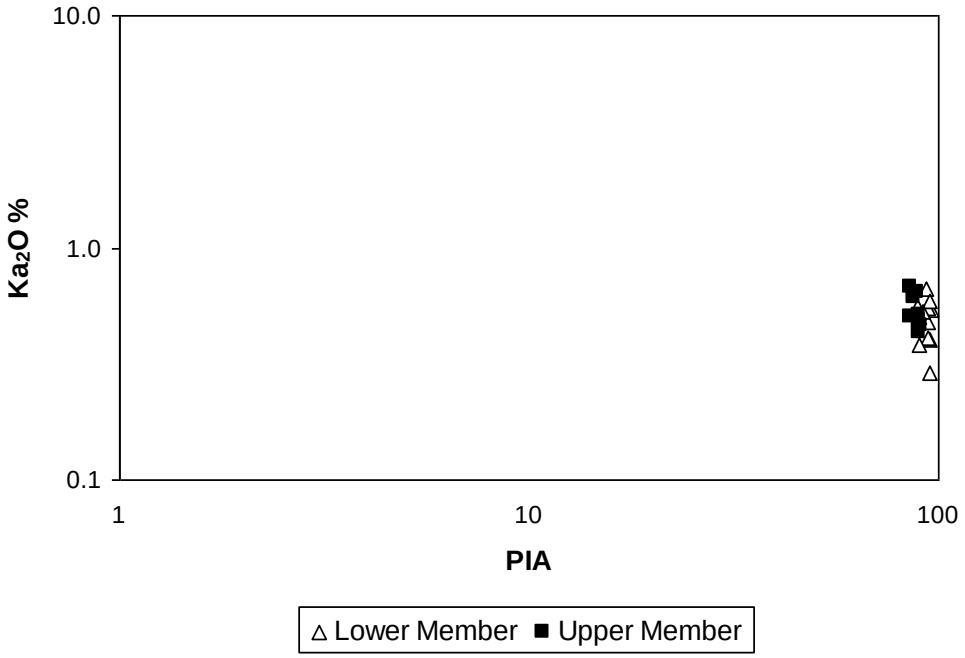

Fig. 2.9: Relationship between PIA and K_2O in the studied black shales.

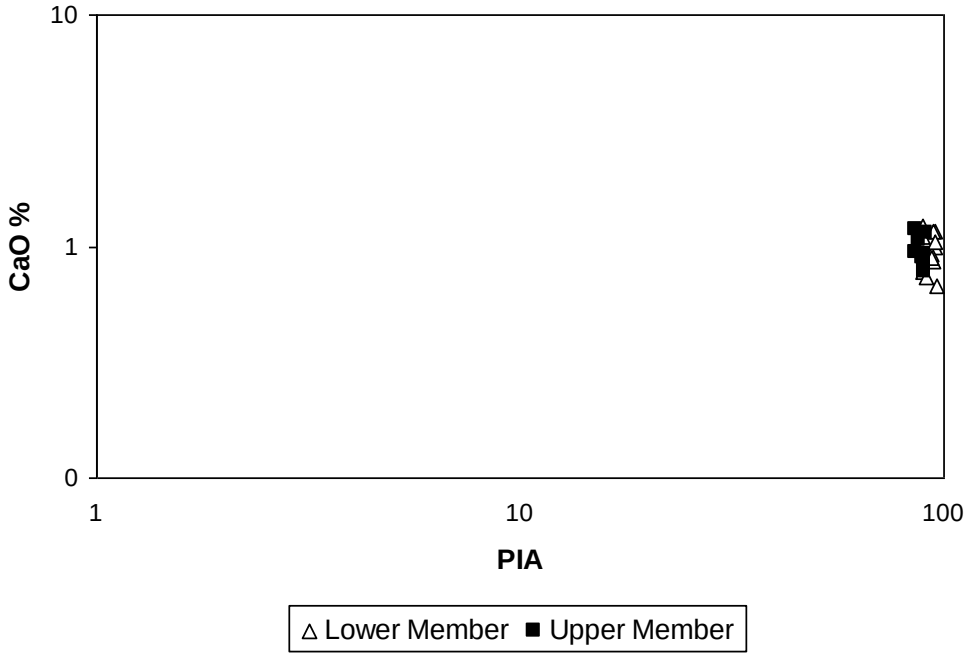

Fig. 2.10: Relationship between PIA and CaO in the studied black shales.

2.5. Paleoclimate and Maturity

The index compositional variation (ICV) can be used to determine the prevailed climatic conditions and maturity of sediments (Cox *et al.*, 1995). In general, mature sediments exhibit low ICV (< 1), while the ICV is high (> 1) in immature deposits (Baiyegunhi *et al.*, 2017). According to Cox *et al.*, (1995) the ICV is calculated as:

$$ICV = (Fe_2O_3+K_2O+Na_2O+CaO+MgO+MnO)/Al_2O_3$$

In the studied black shales, the ICV value ranges from 0.37 to 0.82, indicating the maturation of the sediments. This assumption is also supported by the plot of CIA versus ICV (Fig. 2.11). Furthermore, the plots of $(Al_2O_3+K_2O+Na_2O)$ versus SiO_2 (Fig. 2.12) and K_2O/Al_2O_3 versus Ga/Rb (Fig. 2.13) indicate that the prevailing climate in the source area is semi-humid conditions.

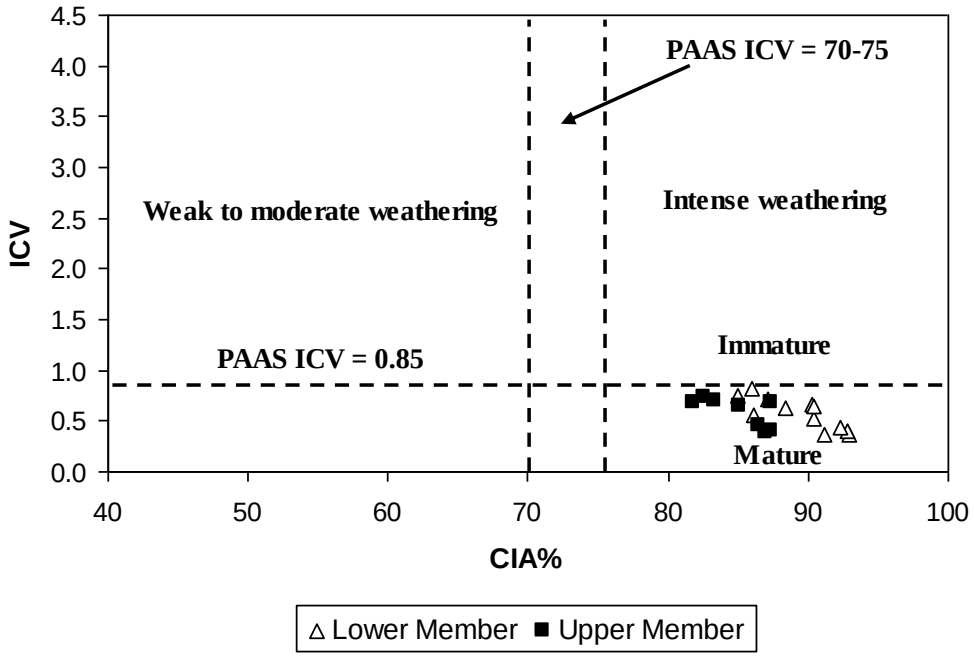

Fig. 2.11: Plot of CIA vs. ICV showing the maturity for the studied black shales (fields after Baiyegunhi et al., 2017).

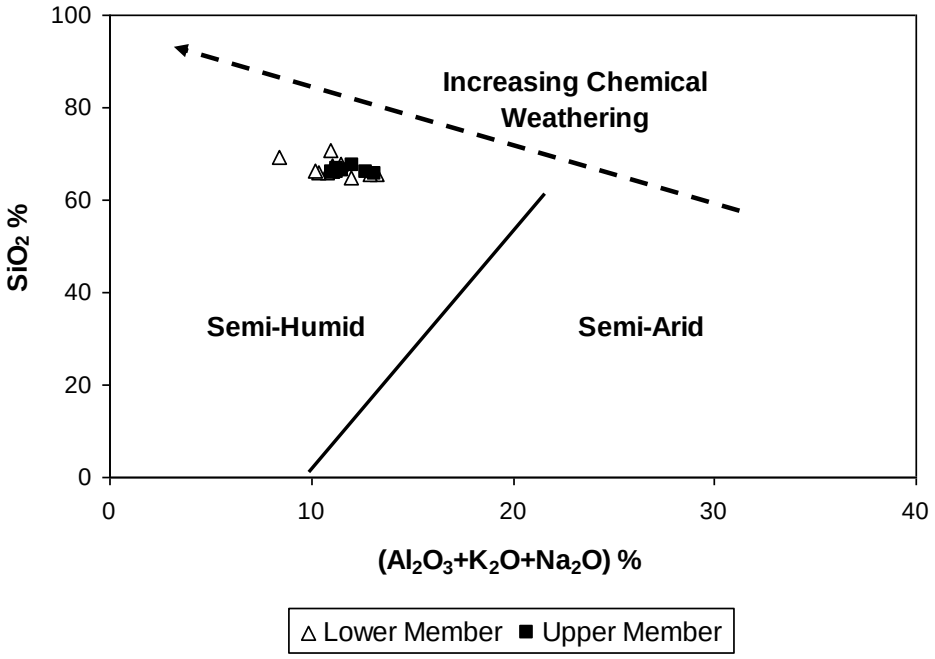

Fig .2.12: Plot of (Al_2O_3+K_2O+Na_2O) vs. SiO_2 showing the paleoclimate conditions for the studied black shales (fields after Suttner and Dutta, 1986).

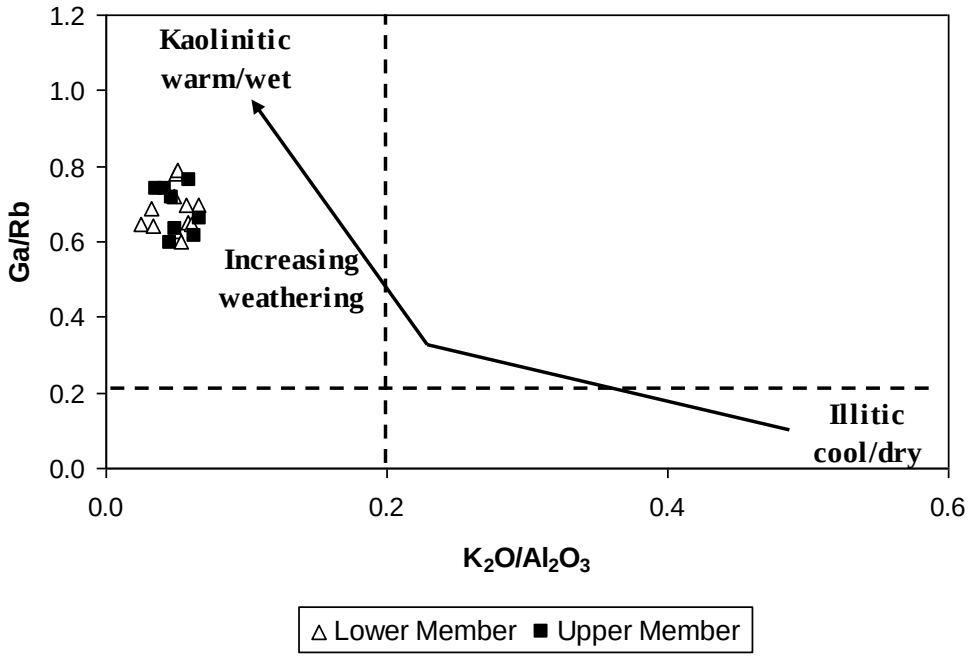

Fig .2.13: Plot of K_2O/Al_2O_3 vs. Ga/Rb showing the paleoclimate conditions for the studied black shales (fields after Roy and Roser, 2013).

2.6. Depositional Environment, Paleo-oxygenation condition and Paleosalinity

Many authors (e.g., Bau and Alexander, 2009) used trace element ratios to determine the depositional environment of clastic rocks. The most common ratios are Zr/Hf, Hf/Ta and Zr/Ta (Bau and Alexander, 2009). In the marine environment, the Zr/Hf, Hf/Ta and Zr/Ta ratios range from 56 to 207, 1.3 to 2.5 and 115 to 688, respectively (Bau and Alexander, 2009). In the current work, these ratios (Tables 2.8-2.9) suggest that marine environment is the proved origin of the Al Jurf Formation.

The B/Ga ratio is one of the parameters used to define the paleosalinity of sediments (Deng and Qian, 1993). High B/Ga value (> 4.2) indicates salt water, B/Ga values from 3.3 and 4.2 suggest brackish water, and B/Ga ratio lower than 3.3 points to fresh water (Deng and Qian, 1993). The B/Ga ratio is high in all black shales (4.31- 6.71), suggesting deposition in a high salinity marine environment.

Table 2.8: Ratios of Zr/Hf, Hf/Ta and Zr/Ta of the black shales of the Lower Member of the Al Jurf Formation

Sample No.	Zr/Hf	Hf/Ta	Zr/Ta
J1	64.55	2.26	146.04
J2	66.61	1.98	131.76
J3	63.70	2.21	140.94
J4	73.39	1.82	133.43
J5	69.23	2.14	148.43
J6	74.88	2.15	160.66
J7	58.88	2.23	131.32
J8	64.73	2.16	139.92
J9	69.23	2.19	151.61
J10	71.90	2.17	155.68
J11	66.38	2.15	142.69
J12	63.71	2.10	134.07

Table 2.9: Ratios of Zr/Hf, Hf/Ta and Zr/Ta of the black shales of the Upper Member of the Al Jurf Formation

Sample No.	Zr/Hf	Hf/Ta	Zr/Ta
J13	65.40	2.20	143.63
J14	62.59	2.14	134.17
J15	68.07	2.24	152.52
J16	73.53	2.25	165.44
J17	58.12	2.31	134.18
J18	63.81	2.24	143.19
J19	70.43	2.05	144.56
J20	76.28	2.05	156.15

Redox-sensitive trace element concentrations or ratios are among the most widely used indicators of redox conditions in modern and ancient sedimentary systems (e.g., Jones and Manning, 1994; Dean *et al.*, 1999; Algeo and Maynard, 2004 and Shaltami *et al.*, 2018). Trace elements commonly exhibit considerable enrichment in laminated, organic-rich facies, especially those deposited under euxinic conditions and, conversely, little if any enrichment in bioturbated, organic-poor facies (Algeo and Maynard, 2004). This pattern exists because:

1) Many trace elements have multiple valence states, and the reduced forms that exist under low-oxygen conditions are more readily complexed with organic acids, taken into solid solution by authigenic sulfides, or precipitated as insoluble oxyhydroxides (Algeo and Maynard, 2004).

2) All trace elements are affected by processes that operate more strongly under low-oxygen conditions (Pratt and Davis, 1992).

Trace element ratios such as Ni/Co, V/Cr and U/Th as well as authigenic U (AU = U-(Th/3)) and δU (δU = 2U/(U+Th/3)) have been used in many studies to determine the redox conditions of sediments (e.g., Jones and Manning, 1994, Nath *et al.*, 1997, Nagarajan *et al.*, 2007 and Yao *et al.*, 2017). Table (2.10) illustrates the standards for the parameters. In the present study, these parameters (Tables 2.11-2.12) indicate that the Al Jurf Formation was deposited in a suboxic marine environment. The plots of Ni/Co versus V/Cr (Fig. 2.14) and U/Th versus AU (Fig. 2.15) support this assumption.

2.7. Paleotectonic Setting

Previous studies (e.g., Wood, 1980; Bhatia, 1983 and He *et al.*, 2011) classified the paleotectonic settings into four types namely, Oceanic Island Arc (A), Continental Island Arc (B), Active Continental Margin (C) and Passive Continental Margin (D). All black shales are located in the fields of C and D (Figs. 2.16-2.18).

Table 2.10: Redox classification using trace element ratios (values of Ni/Co, V/Cr, U/Th, AU and δU after Jones and Manning, 1994, Nath et al., 1997, Nagarajan et al., 2007 and Yao et al., 2017)

Ratio	Oxic conditions	Anoxic conditions
Ni/Co	<5	>5
V/Cr	<2	>2
U/Th	<1.25	>1.25
AU	<5	>5
δU	<1	>1

Table 2.11: Values of Ni/Co, V/Cr, U/Th, AU and δU of the black shales of the Lower Member of the Al Jurf Formation

Sample No.	Ni/Co	V/Cr	U/Th	AU	δU
J1	7.67	4.20	1.26	7.91	1.58
J2	7.69	5.43	1.17	7.27	1.56
J3	6.96	3.66	1.20	7.26	1.57
J4	7.14	6.19	1.04	6.20	1.52
J5	8.54	3.92	1.36	6.70	1.61
J6	10.69	4.72	1.15	6.39	1.55
J7	7.00	4.67	1.07	6.66	1.53
J8	6.80	5.49	1.37	8.02	1.61
J9	12.30	5.53	1.03	4.94	1.51
J10	10.45	5.44	1.15	5.71	1.55
J11	6.88	3.94	0.98	5.53	1.49
J12	7.05	3.41	0.94	5.13	1.47

Table 2.12: Values of Ni/Co, V/Cr, U/Th, AU and δU of the black shales of the Upper Member of the Al Jurf Formation

Sample No.	Ni/Co	V/Cr	U/Th	AU	δU
J13	7.84	5.18	1.15	7.00	1.55
J14	7.86	4.10	1.18	7.17	1.56
J15	8.63	3.92	1.09	4.93	1.53
J16	10.84	4.88	0.95	4.88	1.48
J17	7.05	4.67	1.06	6.61	1.52
J18	6.84	5.50	1.31	7.54	1.59
J19	8.45	3.91	1.25	5.97	1.58
J20	10.55	4.71	0.97	4.98	1.49

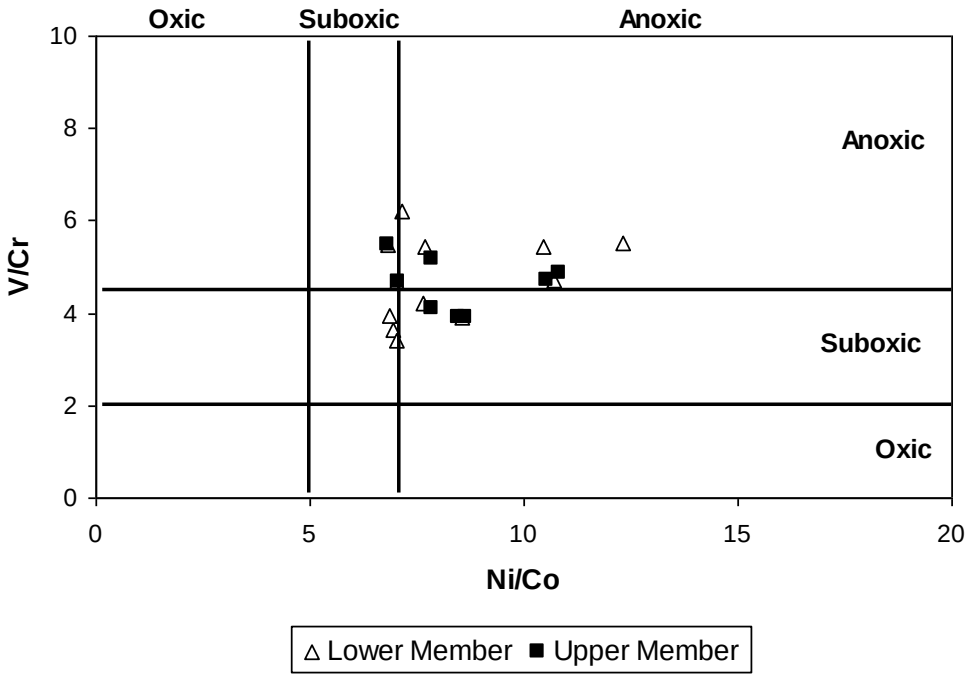

Fig. 2.14: Plot of Ni/Co vs. V/Cr showing the paleooxygenation conditions for the studied black shales (fields after Jones and Manning, 1994).

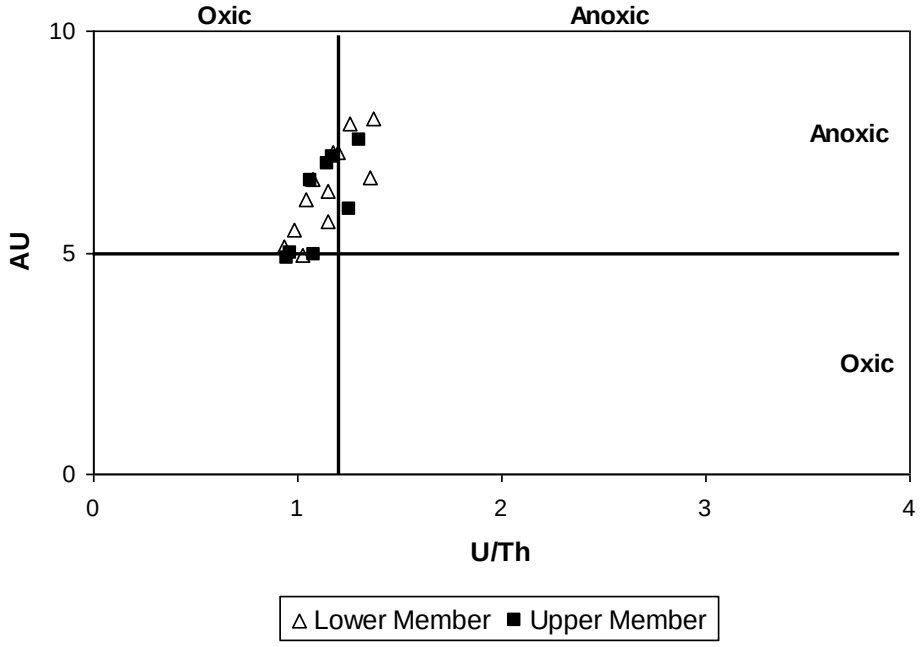

Fig. 2.15: Plot of U/Th vs. AU showing the paleooxygenation conditions for the studied black shales (fields after Nath et al., 1997 and Nagarajan et al., 2007).

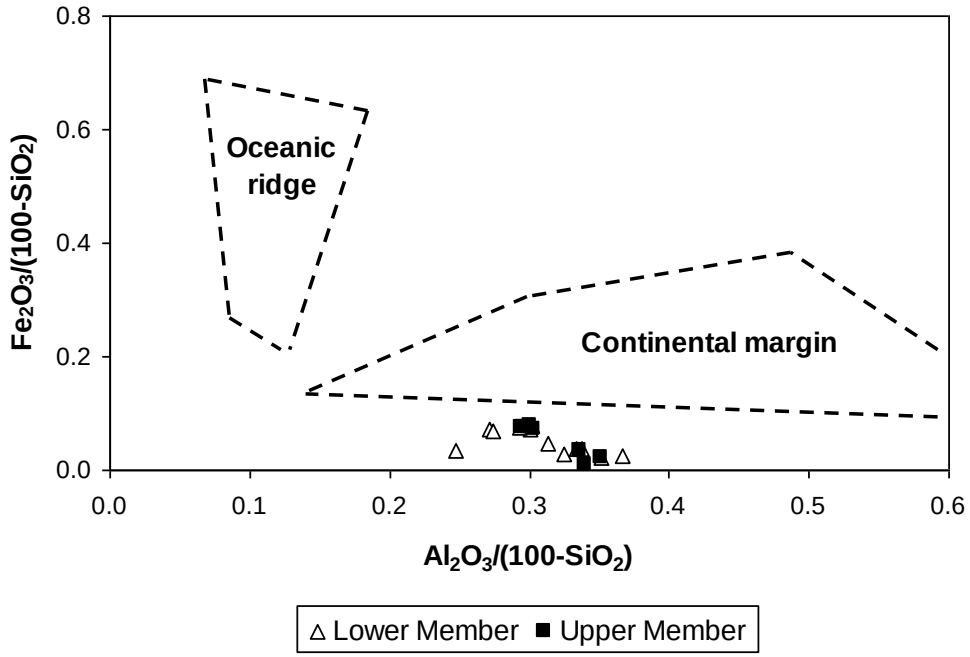

Fig. 2.16: Plot of $Al_2O_3/(100-SiO_2)$ vs. $Fe_2O_3/(100-SiO_2)$ showing the paleotectonic setting for the studied black shales (fields after He et al., 2011).

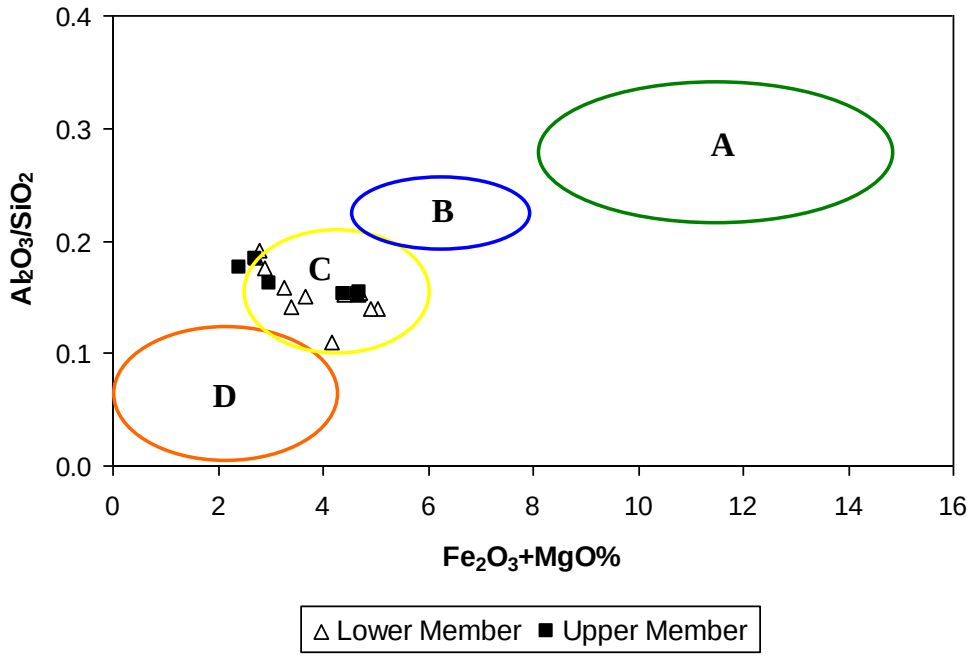

Fig. 2.17: Plot of Fe_2O_3+MgO vs. Al_2O_3/SiO_2 showing the paleotectonic setting for the studied black shales (fields after Bhatia, 1983).

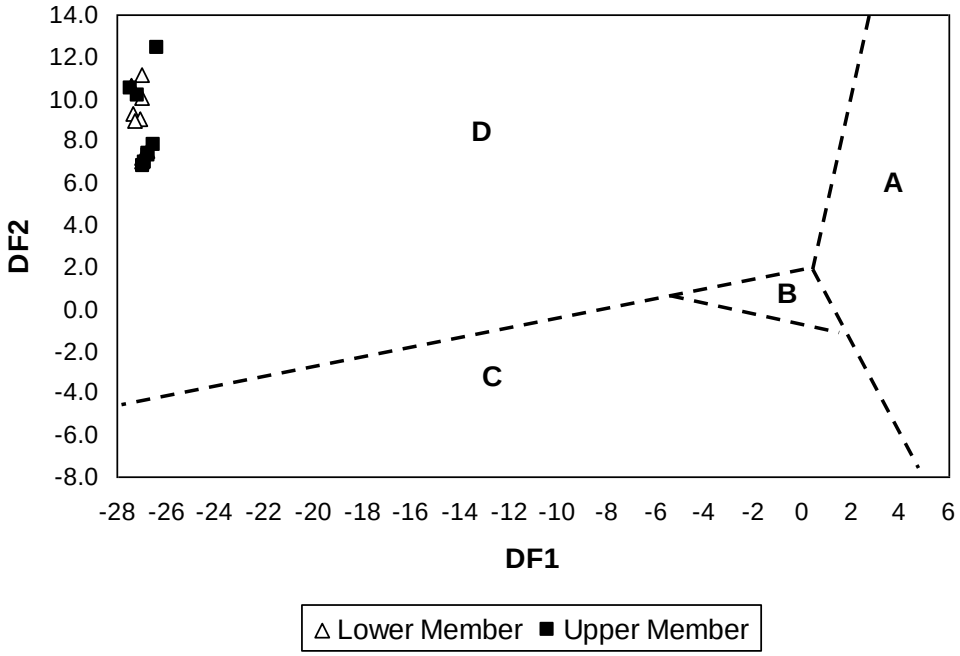

Fig. 2.18: Plot of DF1 vs. DF2 showing the paleotectonic setting for the studied black shales (fields after Bhatia, 1983).

The discriminant functions are calculated as:

DF1 = $-0.447SiO_2 - 0.972TiO_2 - 0.059Fe_2O_3 - 3.082MnO + 0.140MgO + 0.195CaO + 0.719Na_2O - 0.032K_2O + 7.51P_2O_5 + 0.303$)

DF2 = $-0.421SiO_2 + 1.988TiO_2 - 0.526Al_2O_3 - 2.161Fe_2O_3 + 2.720MnO + 0.881MgO - 0.907CaO - 0.177Na_2O - 1.840K_2O + 7.244P_2O_5 + 43.57$)

CHAPTER THREE
ORGANIC PETROGRAPHY AND GEOCHEMISTRY

3.1. Introduction

Organic petrography is the study of the organic constituents, known as macerals, in sedimentary rocks, that is, the description and terminology of the properties of the organic matter, whether the rocks be, for example, coal, petroleum source rocks and oil shales (all of which contain abundant organic matter) or limestone, sandstone and shale (all with minor dispersed organic matter (DOM)) (Belkin *et al.,* 2010; Furmann *et al.,* 2015 and Ndip *et al.,* 2019). Traditional petrographic studies utilize transmitted light microscopy for thin-sections and strew mounts (as in palynological and kerogen studies) or incident (also called reflected) white light microscopy for polished blocks. In the last two decades, organic petrography has advanced significantly with the development of fluorescence mode microscopy (Flores *et al.,* 2010; Furmann *et al.,* 2015 and Cavelan *et al.,* 2019).

Organic geochemistry is the study of the impacts and processes that organisms have had on the Earth (Kvenvolden, 2006). For the past 20 years, organic geochemistry has been widely applied to solve exploration problems such as source-rock recognition, maturity evaluation, oil-oil or oil-source correlations or to predict hydrocarbon fluid composition in a potential target. However, since the late eighties (Kaufman *et al.,* 1990), geochemistry has helped to solve production problems such as reservoir continuity, identification of producing/non-producing intervals or leaking of casing and production allocation. These approaches were based on static approaches where differences in composition are interpreted mainly in terms of reservoir continuity (Curiale and Curtis, 2016).

3.2. Organic Petrography

A maceral is a component, organic in origin, of coal or oil shale (Kruszewska, 2003). Macerals are analogous to minerals in inorganic rocks, but they lack a definite crystalline structure. Macerals are classified into three major groups: vitrinite/huminite, inertinite, and liptinite/exinite.

In the present study, vitrinite is the main maceral in the studied black shales, consisting of collotelinite (Fig. 3.1) and vitrodetrinite (Fig. 3.2). Liptinite is the second most common maceral in terms of abundance, consisting of resinite (Fig. 3.3), cutinite (Fig. 3.4), sporinite (Fig. 3.5) and alginite (Fig. 3.6). Inertinite, in the form of fusinite (Fig. 3.7) and inertodetrinite (Fig. 3.8), is a minor component of the black shales. However, the studied samples also contain a large amount of framboidal pyrite (Fig. 3.9).

3.3. Organic Geochemistry

The results of source rock analyzer (SRA) and gas chromatography-mass spectrometry (GC-MS) are shown in tables (3.1-3.8).

3.3.1. Statistical Treatments

In the current chapter, three types of statistical analysis were used, namely descriptive statistics (Table 3.9), Pearson's correlation coefficient (correlation analysis, Table 3.10 and Fig. 3.10) and factor analysis (Table 3.11 and Fig. 3.11). The SPSS© program was used to perform the previous analyses.

The contribution of S_1 and S_2 from TOC is evident through the strong correlation between TOC and both S_1 and S_2 (r = 0.89 and 0.91, respectively). Moreover, the maturity of the studied black shales is independent of the amount of organic matter, because TOC is negatively correlated with HI, OI and PI (r = -0.22, -0.94 and -0.92, respectively).

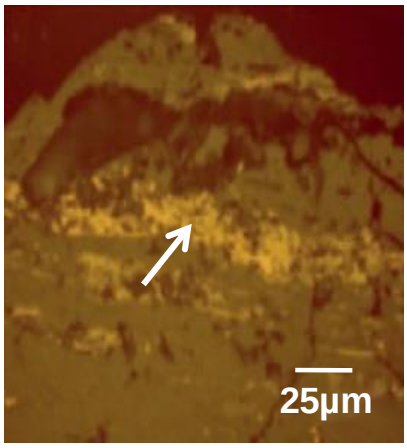

Fig. 3.1: Photomicrograph (oil immersion) showing collotelinite (white arrow, sample J6).

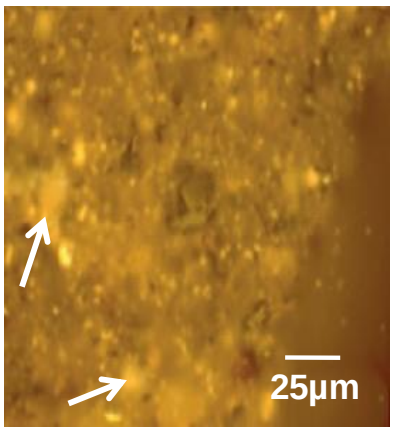

Fig. 3.2: Photomicrograph (oil immersion) showing vitrodetrinite (white arrows, sample J13).

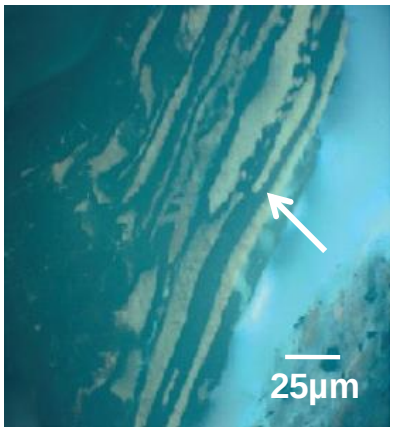

Fig. 3.3: Photomicrograph (oil immersion) showing resinite (white arrow, sample J20).

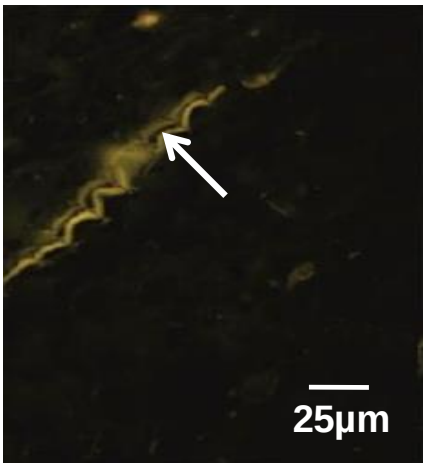

Fig. 3.4: Photomicrograph showing cutinite (white arrow, sample J17).

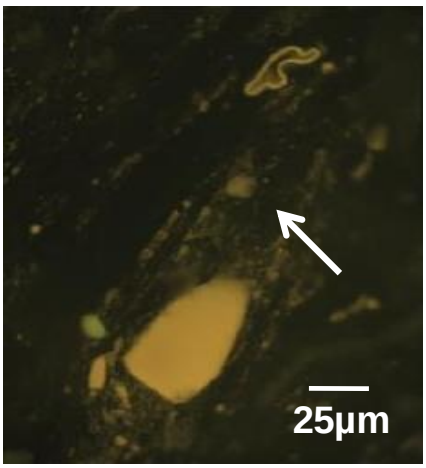

Fig. 3.5: Photomicrograph showing sporinite (white arrow, sample J17).

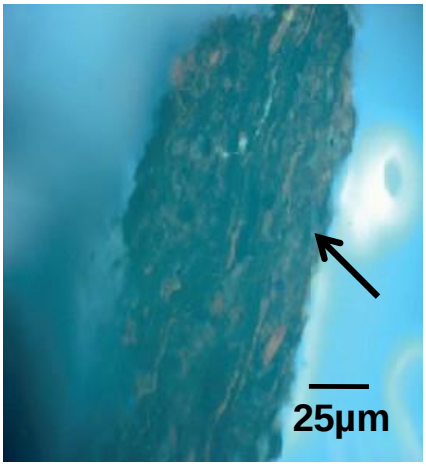

Fig. 3.6: Photomicrograph (oil immersion) showing alginite (black arrow, sample J20).

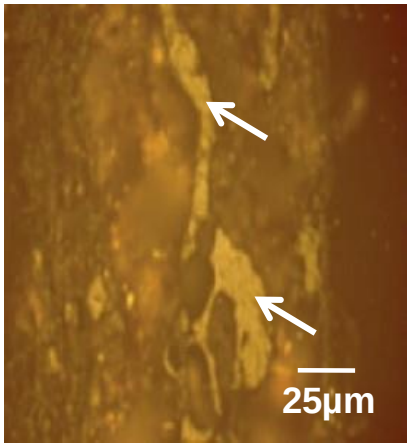

Fig. 3.7: Photomicrograph (oil immersion) showing fusinite (white arrows, sample J13).

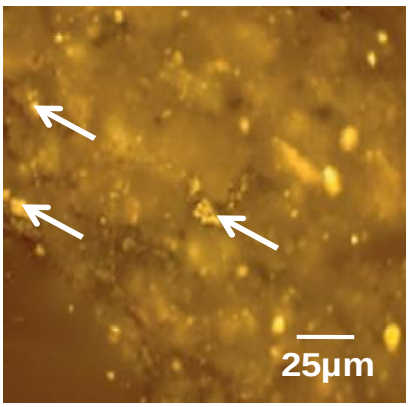

Fig. 3.8: Photomicrograph (oil immersion) showing inertodetrinite (white arrows, sample J13).

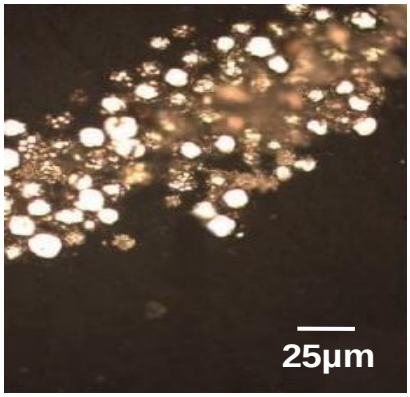

Fig. 3.9: Photomicrograph showing framboidal pyrite (Sample J15).

Table 3.1: SRA data of the black shales of the Lower Member of the Al Jurf Formation

Sample No.	TOC	T_{max}	Ro	S_1	S_2	S_3	HI	OI	GP	PI
J1	0.85	433.00	0.66	4.09	3.16	1.33	371.77	156.47	5.25	0.78
J2	0.82	432.00	0.70	4.56	3.27	1.29	398.78	157.32	5.83	0.78
J3	0.82	434.00	0.68	3.47	3.65	1.41	445.12	171.95	5.58	0.62
J4	0.78	434.00	0.71	4.16	3.44	1.44	441.05	184.62	5.60	0.74
J5	0.75	435.00	0.62	3.37	3.36	1.39	448.00	185.33	4.73	0.71
J6	0.76	440.00	0.64	3.82	2.90	1.32	381.58	173.68	5.03	0.76
J7	0.80	441.00	0.69	4.14	2.34	1.52	292.50	190.00	5.48	0.76
J8	0.83	441.00	0.70	4.00	2.29	1.50	275.90	180.72	5.29	0.76
J9	0.65	435.00	0.70	3.92	2.43	1.50	373.85	230.77	5.35	0.73
J10	0.66	432.00	0.72	4.17	3.23	1.47	489.39	222.73	5.40	0.77
J11	0.57	440.00	0.72	3.75	2.66	1.11	466.67	194.74	5.41	0.69
J12	0.71	440.00	0.65	3.44	2.62	1.08	369.00	152.11	5.06	0.68

Table 3.2: SRA data of the black shales of the Upper Member of the Al Jurf Formation

Sample No.	TOC	T_{max}	Ro	S_1	S_2	S_3	HI	OI	GP	PI
J13	4.11	437.00	0.81	7.17	10.34	1.62	251.58	39.42	17.51	0.41
J14	4.40	435.00	0.81	7.05	10.81	1.58	245.68	35.91	17.86	0.39
J15	3.54	433.00	0.80	8.11	13.83	1.55	390.68	43.79	21.94	0.37
J16	2.32	433.00	0.84	7.77	14.00	1.43	603.45	61.64	21.77	0.36
J17	3.88	438.00	0.79	8.08	15.79	1.60	406.96	41.24	23.87	0.34
J18	4.78	437.00	0.77	8.34	17.14	1.60	358.58	33.47	25.48	0.33
J19	3.71	437.00	0.76	9.20	15.09	1.49	406.74	40.16	24.29	0.38
J20	2.39	433.00	0.76	8.87	14.17	1.54	592.89	64.44	23.04	0.38

Where: TOC = total organic carbon (wt. %), S_1 = amount of free hydrocarbons in sample (mg/g), S_2 = amount of hydrocarbons generated through thermal cracking (mg/g) – provides the quantity of hydrocarbons that the rock has the potential to produce through diagenesis, S_3 = amount of CO_2 (mg of CO_2/g of rock) - reflects the amount of oxygen in the oxidation step, T_{max} = the temperature at which maximum rate of generation of hydrocarbons occurs, Hydrogen index: HI = $(100*S_2)/TOC$, Oxygen index: OI = $(100*S_3)/TOC$, Production index: PI = $S_1/(S_1+S_2)$, Semi-quantitative index: GP = S_1/S_2, Ro = vitrinite reflectance (wt. %)

Table 3.3: Gas chromatogram data of normal alkanes and isoprenoids ratios of the black shales of the Lower Member of the Al Jurf Formation (calculated on m/z 85)

Sample No.	Pr/Ph	(Pr+n-C_{17})/ (Ph+n-C_{18})	Pr/n-C_{17}	Ph/n-C_{18}	$\sum$(n-C_{12}-n-C_{20})/ ($\sum$(n-C_{12}-n-C_{20})+ $\sum$(n-C_{12}-n-C_{29}))	CPI	WI
J1	1.62	1.13	0.29	0.52	0.51	0.84	0.80
J2	2.38	1.22	0.27	0.49	0.58	0.90	0.74
J3	2.40	0.98	0.23	0.41	0.70	0.81	0.81
J4	1.50	1.00	0.25	0.45	0.69	0.75	0.84
J5	1.62	0.92	0.26	0.47	0.42	0.87	0.79
J6	2.61	0.90	0.23	0.51	0.45	0.74	0.82
J7	1.54	1.12	0.17	0.46	0.56	0.80	0.70
J8	1.57	1.10	0.20	0.48	0.42	0.64	0.67
J9	2.38	1.00	0.29	0.52	0.67	0.66	0.80
J10	2.44	0.89	0.25	0.51	0.64	0.58	0.85
J11	1.77	0.90	0.18	0.37	0.51	0.43	0.45
J12	2.47	1.08	0.20	0.40	0.43	0.49	0.41

Table 3.4: Gas chromatogram data of normal alkanes and isoprenoids ratios of the black shales of the Upper Member of the Al Jurf Formation (calculated on m/z 85)

Sample No.	Pr/Ph	(Pr+n-C_{17})/ (Ph+n-C_{18})	Pr/n-C_{17}	Ph/n-C_{18}	$\sum$(n-C_{12}-n-C_{20})/ ($\sum$(n-C_{12}-n-C_{20})+ $\sum$(n-C_{12}-n-C_{29}))	CPI	WI
J13	1.70	0.77	0.24	0.41	0.69	0.72	0.68
J14	2.72	0.79	0.27	0.44	0.44	0.69	0.63
J15	1.69	0.65	0.28	0.45	0.52	0.85	0.84
J16	1.66	0.54	0.25	0.49	0.50	0.72	0.87
J17	2.71	0.56	0.19	0.44	0.50	0.78	0.75
J18	1.42	0.71	0.22	0.46	0.74	0.62	0.72
J19	2.12	0.66	0.24	0.49	0.66	0.89	0.74
J20	1.63	0.63	0.21	0.53	0.58	0.76	0.77

Table 3.5: Gas chromatogram data of steranes and diasteranes of the black shales of the Lower Member of the Al Jurf Formation (calculated on m/z 217)

Sample No.	C_{27}	C_{28}	C_{29}	C_{29} (ßß/ßß+αα)	C_{29} ßα(S+R)-dia/ (C_{28} ßα(S+R)-dia+ C_{27} ßα(S+R)-dia)
J1	46.00	15.54	38.46	0.37	0.67
J2	45.54	17.58	36.88	0.36	0.55
J3	50.11	9.44	40.45	0.36	0.61
J4	48.91	7.41	43.68	0.33	0.61
J5	49.09	13.56	37.35	0.39	0.53
J6	51.66	4.61	43.73	0.33	0.44
J7	51.18	11.54	37.28	0.33	0.57
J8	46.30	13.52	40.18	0.41	0.49
J9	50.35	8.46	41.19	0.44	0.63
J10	50.27	10.43	39.30	0.47	0.65
J11	47.18	11.00	41.82	0.47	0.43
J12	47.23	12.10	40.67	0.39	0.40

Table 3.6: Gas chromatogram data of steranes and diasteranes of the black shales of the Upper Member of the Al Jurf Formation (calculated on m/z 217)

Sample No.	C_{27}	C_{28}	C_{29}	C_{29} (ββ/ββ+αα)	C_{29} ßα(S+R)-dia/ (C_{28} ßα(S+R)-dia+ C_{27} ßα(S+R)-dia)
J13	46.44	12.56	41.00	0.39	0.59
J14	50.47	8.61	40.92	0.43	0.57
J15	48.43	10.61	40.96	0.44	0.60
J16	50.41	6.66	42.93	0.44	0.41
J17	48.28	9.59	46.13	0.40	0.38
J18	45.34	14.57	40.09	0.42	0.36
J19	46.53	12.51	40.96	0.40	0.49
J20	50.51	10.56	38.93	0.40	0.60

Table 3.7: Gas chromatogram data of terpanes, hopanes and TPP ratios of the black shales of the Lower Member of the Al Jurf Formation (calculated on m/z 217)

Sample No.	C_{31}R/ C_{30}H	C_{32} 22S/ (22S+22R)	G/C_{30}	Hopanes/ (Hopanes+ ∑20R steranes)	TPP ratios
J1	0.44	0.55	0.63	0.54	0.13
J2	0.41	0.57	0.78	0.52	0.17
J3	0.51	0.61	0.90	0.56	0.20
J4	0.50	0.61	0.72	0.55	0.19
J5	0.50	0.64	0.72	0.55	0.23
J6	0.53	0.68	0.65	0.50	0.23
J7	0.46	0.68	0.88	0.59	0.21
J8	0.42	0.63	0.76	0.53	0.16
J9	0.42	0.59	0.80	0.53	0.13
J10	0.49	0.55	0.80	0.50	0.13
J11	0.40	0.54	0.62	0.48	0.17
J12	0.40	0.57	0.83	0.47	0.20

Table 3.8: Gas chromatogram data of terpanes, hopanes and TPP ratios of the black shales of the Upper Member of the Al Jurf Formation (calculated on m/z 217)

Sample No.	$C_{31}R/C_{30}H$	C_{32} 22S/(22S+22R)	G/C_{30}	Hopanes/(Hopanes+∑20R steranes)	TPP ratios
J13	0.57	0.70	0.74	0.61	0.12
J14	0.52	0.68	0.71	0.60	0.11
J15	0.51	0.65	0.71	0.63	0.15
J16	0.47	0.68	0.88	0.60	0.17
J17	0.39	0.67	0.82	0.57	0.13
J18	0.36	0.67	0.90	0.55	0.18
J19	0.33	0.65	0.92	0.59	0.17
J20	0.33	0.69	0.92	0.62	0.17

Where:

Pr/Ph = Pristane/Phytane

G/C_{30} = Gammacerane index

Carbon preference index: $CPI = 2(C_{23}+C_{25}+C_{27}+C_{29})/(C_{22}+2[C_{24}+C_{26}+C_{28}]+C_{30})$

Waxiness index: $WI = \Sigma(n\text{-}C_{21}\text{-}n\text{-}C_{31})/\Sigma(n\text{-}C_{15}\text{-}n\text{-}C_{20})$

TPP = Tetracyclic polyprenoid

Table 3.9: Descriptive statistics of organic parameters of the studied black samples

Parameters	N	Minimum	Maximum	Mean	Std. Deviation
TOC	20	0.57	4.78	1.91	1.55
T_{max}	20	432.00	441.00	436.00	3.11
Ro	20	0.62	0.84	0.73	0.06
S_1	20	3.37	9.20	5.57	2.16
S_2	20	2.29	17.14	7.33	5.69
S_3	20	1.08	1.62	1.44	0.15
HI	20	245.68	603.45	400.51	95.84
OI	20	33.47	230.77	128.03	72.34
PI	20	0.33	0.78	0.59	0.19

Table 3.10: Correlation matrix of organic parameters of the studied black samples

Parameters	TOC	T_{max}	Ro	S_1	S_2	S_3	HI	OI	PI
TOC	1.00								
T_{max}	-0.06	1.00							
Ro	0.80	-0.23	1.00						
S_1	0.89	-0.20	0.83	1.00					
S_2	0.91	-0.18	0.81	0.97	1.00				
S_3	0.66	-0.19	0.60	0.62	0.59	1.00			
HI	-0.22	-0.48	0.06	0.14	0.17	-0.22	1.00		
OI	-0.94	0.11	-0.79	-0.92	-0.93	-0.52	0.05	1.00	
PI	-0.92	0.14	-0.84	-0.93	-0.97	-0.56	-0.11	0.94	1.00

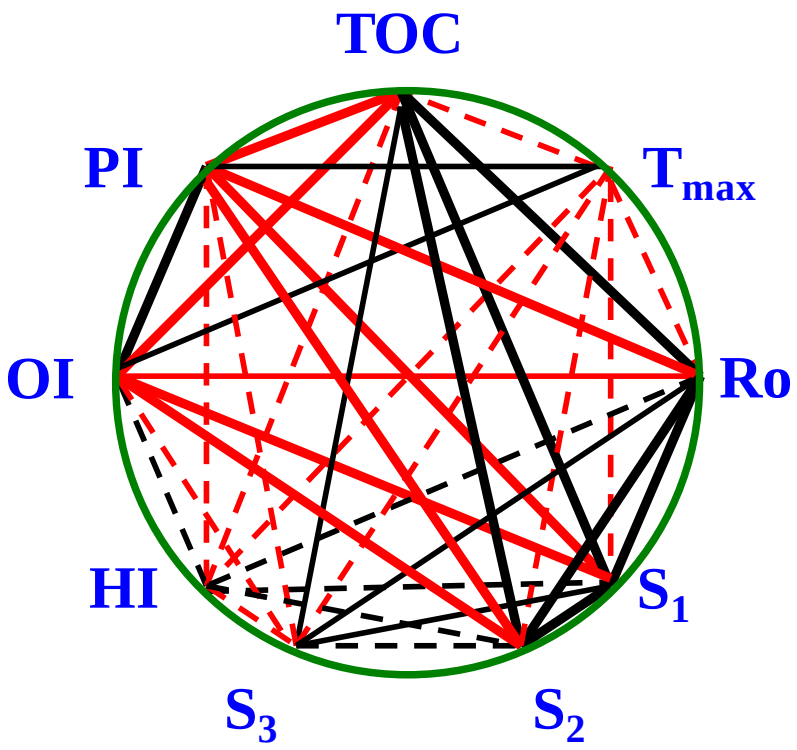

Fig. 3.10: Correlations among the analyzed organic parameters in the black shale samples (intensity of lines corresponds to the strength of the correlation coefficient (< 0.4 to > 0.8)) (red line means inverse relation).

Table 3.11: Factor analysis of organic parameters of the black shale samples

Eigenvalue	5.94	1.55	0.79
% of Variance	65.96	17.26	8.74
Cumulative %	65.96	83.22	91.96
Factor	1	2	3
TOC	0.95	0.24	-0.01
T_{max}	-0.21	0.78	0.51
Ro	0.89	-0.06	-0.04
S_1	0.97	-0.08	0.10
S_2	0.97	-0.09	0.15
S_3	0.69	0.18	-0.59
HI	0.03	-0.91	0.30
OI	-0.95	-0.09	-0.15
PI	-0.97	0.03	-0.18

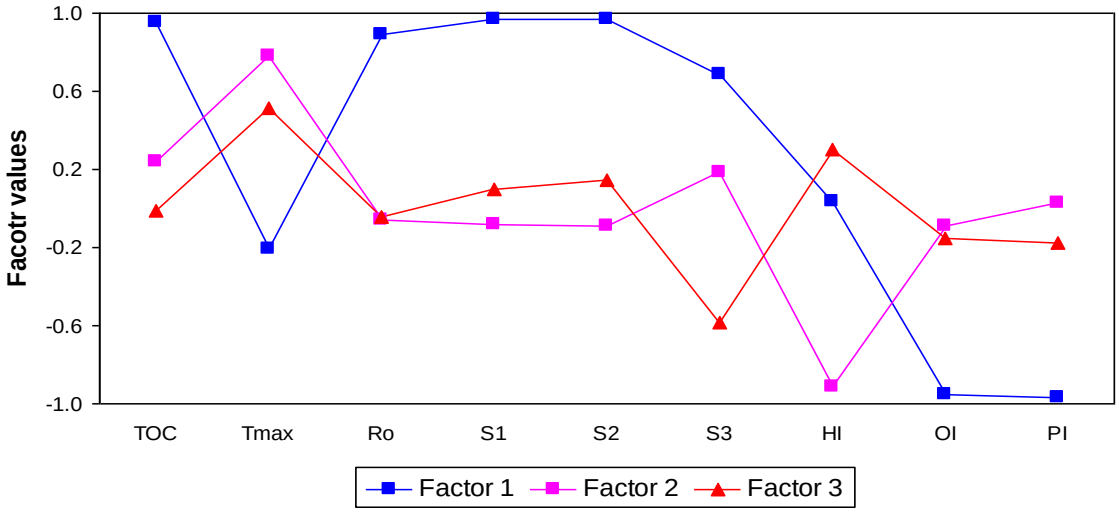

Fig. 3.11: Distribution of the analyzed parameters in factors 1, 2 and 3

Three factors were conducted for the black shale samples. The following is an explanation of these factors:

Factor one (F1): It accounts for about 65.95 % of the total variables. It shows positive loading for TOC, Ro, S_1, S_2 and S_3 and negative loading for OI and PI. This factor is important in interpreting source rock quality.

Factor two (F2): It accounts for 17.26 % of the total variables. It shows positive loading for T_{max} and negative loading for HI. It can be nominated as the factor of thermal maturity.

Factor three (F3): It accounts for 8.74 % of the total variables. This factor is practically insignificant, because it does not show loading for any parameter.

3.3.1. Organic Matter Richness

Peters and Cassa, (1994) divided the organic richness of the source rocks into five grades:

1) Poor (TOC < 0.5 %).
2) Fair (0.5 % < TOC < 1 %).
3) Good (1 % < TOC < 2 %).
4) Very good (2 % < TOC < 4 %).
5) Excellent (TOC > 4 %).

Figs (3.12-3.13) indicate that the black shale of the Upper Member of the Al Jurf Formation has very good to excellent quality, whereas the black shale of the Lower Member is a fair source rock. Moreover, the positive correlation between TOC and Al_2O_3 (Fig. 3.14) suggests that clay minerals are the main carrier of TOC. Additionally, TOC is strongly correlated with U (Fig. 3.15). The mobility/stability of U is influenced by a suite of inorganic, organic and microbial processes often operating in parallel. The net outcome of such processes determines whether U mobility is retarded in such away that U can become stabilized within deposits (Cumberland *et al.*, 2016).

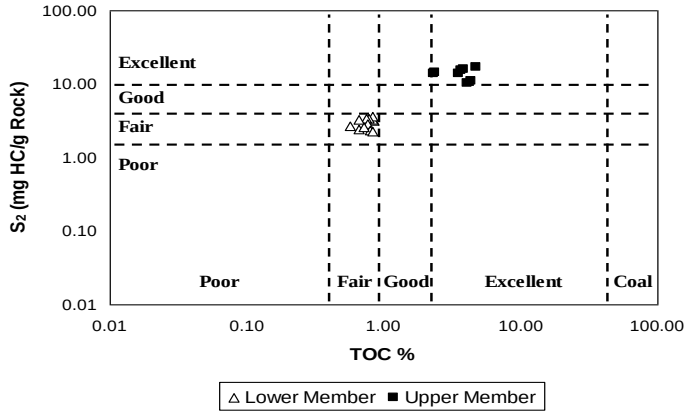

Fig. 3.12: Plot of TOC vs. S_2 showing the hydrocarbon potentialities for the studied black shales (fields after Dembicki, 2009).

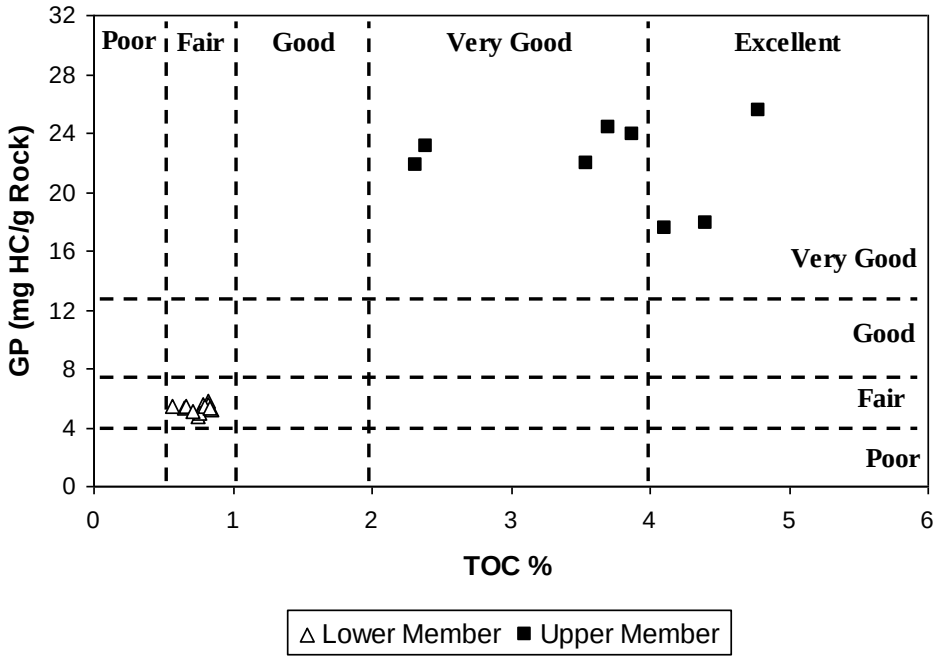

Fig. 3.13: Plot of TOC vs. GP showing the hydrocarbon potentialities for the studied black shales (fields after Ghori, 2002).

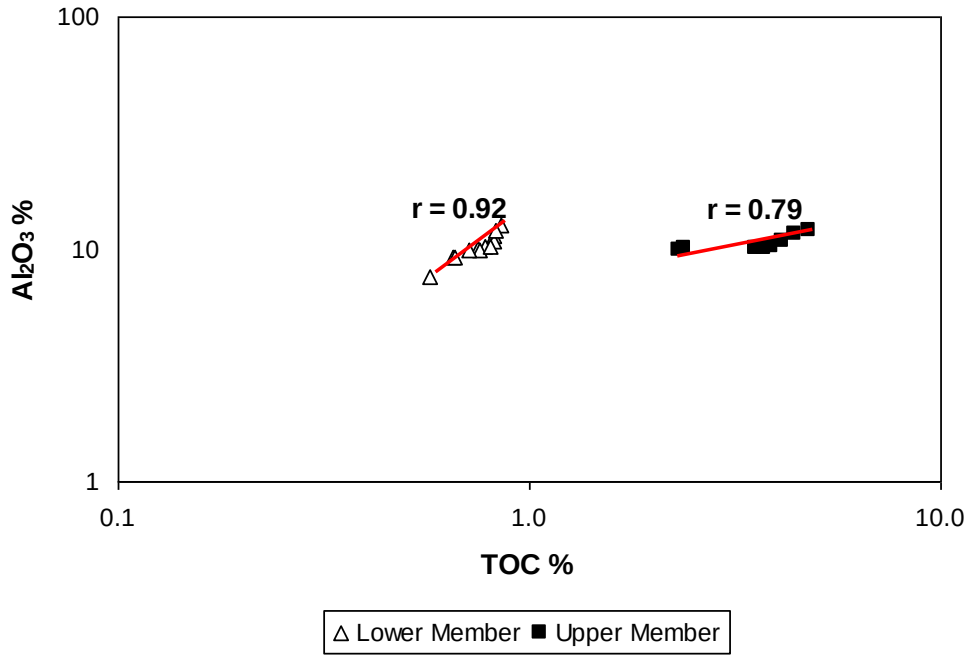

Fig. 3.14: Relationship between TOC and Al_2O_3 for the studied black shales.

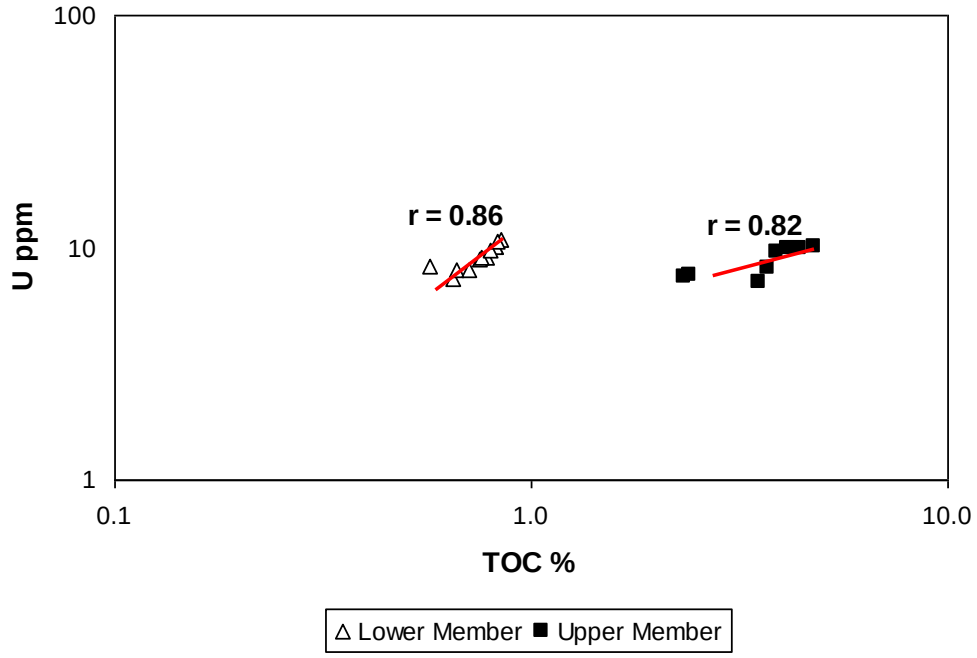

Fig. 3.15: Relationship between TOC and U for the studied black shales.

3.3.2. Organic Matter Type

Classification of kerogen depends mainly on chemical composition. Based on C, H and O compositions, four basic types are defined: I, II, III, and IV (Van Krevelen, 1961). Type I and II kerogen produce oil when the kerogen has matured and gas when post-mature; Type III kerogen produces gas after being subjected to significant thermal maturity. Type IV is an inert kerogen. A Type IIS kerogen is from a sulfur rich kerogen that decomposes into heavier, sulfur rich oil at somewhat lower thermal maturity (Van Krevelen, 1961).

The plots of HI versus OI and TOC versus S_2 (Figs. 3.16-3.17) show that all black shales contain two types of kerogen (II and II/III) that are capable of generating of both oil and gas. This result corresponds to the petrographic assessment, because Type II kerogen contains algal and bacterial organic matter that is dominated by liptinite macerals, while Type III kerogen consists of higher plant material dominated by vitrinite macerals.

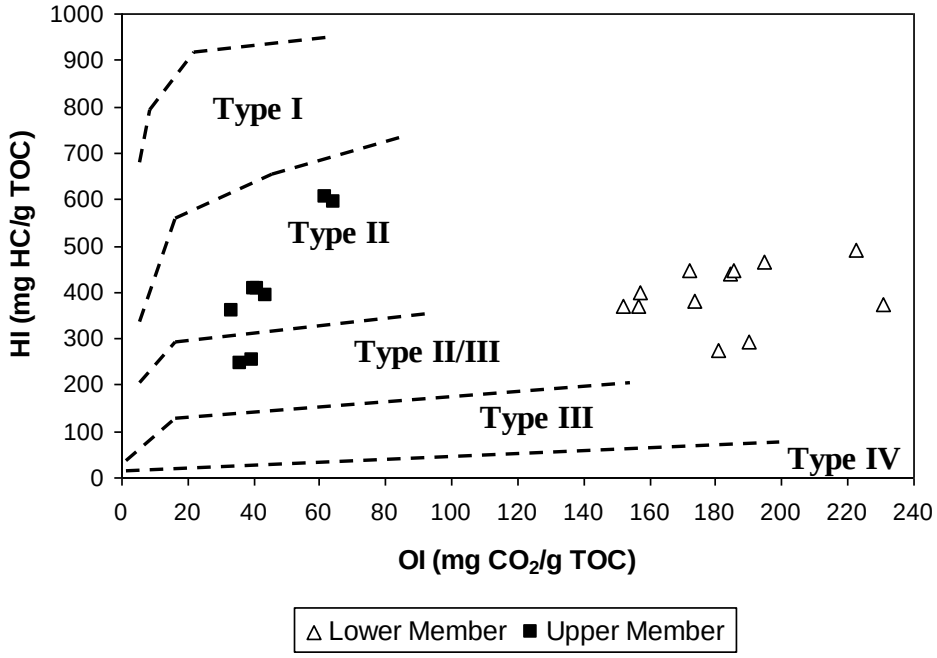

Fig. 3.16: Plot of OI vs. HI showing the kerogen type for the studied black shales (fields after Van Krevelen, 1961).

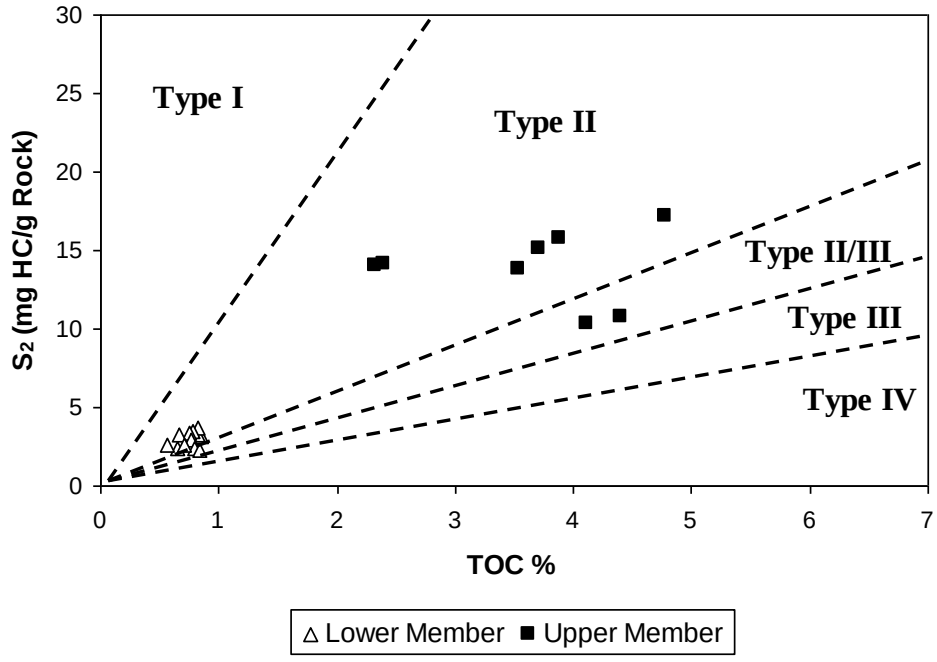

Fig. 3.17: Plot of TOC vs. S_2 showing the kerogen type for the studied black shales (fields after Longford and Blanc-Valleron, 1990).

3.3.3. Thermal Maturity

Thermal maturity is a key parameter for the determination of potentially prospective shale oil and gas accumulations at initial stages of exploration. Based on thermal maturity values, source rocks are categorized as thermally immature, mature or post-mature rocks in terms of capability to generate hydrocarbons (Kok *et al.,* 2001). Immature (i.e. thermally unaltered) source rocks that are still at relatively small depths may generate (biogenic) natural gas which is formed by certain bacteria species as a result of their metabolic activity (Kok *et al.,* 2001; Nabbefeld *et al.,* 2010 and Jubb *et al.,* 2018). Normally, these processes occur at temperatures below 50 ^{o}C, and the degree of organic matter alteration, as expressed by reflectance index, is not in excess of 0.5 % Ro. As the source rock is buried, for example under an increasingly thicker overburden, the processes of bacterial organic matter alteration subside, while temperatures and pressures of the rock increase and gradually trigger chemical changes that lead to the generation of oil and smaller quantities of natural gas (Kok *et al.,* 2001). A rock which had been heated so as to generate crude oil is called mature rock in the oil generation phase or in the so-called "oil window", and its alteration degree, expressed as vitrinite reflectance index, ranges from 0.5 to 1.2 % Ro (Hall *et al.,* 2016). If buried deeper, the source rock will generate mostly (thermogenic) natural gas. Accordingly, a mix of the previously generated oil and of the "newly generated" natural gas (the so-called condensate) is expected to occur in the rock (Kok *et al.,* 2001). If the rock medium is even deeper buried, organic matter will generate (thermogenic) natural gas only. Moreover, any oil previously accumulated in the rock will be transformed into (thermogenic) natural gas (Kok *et al.,* 2001). This degree of thermal alteration called the "gas window" occurs at temperatures in the order of 120-150 ^{o}C and is expressed by reflectance index values ranging from approx. 1.2 to 2 % Ro (Hall *et al.,* 2016). The process will continue until alteration processes reach the degree at which the source rock becomes overmature and its hydrocarbon generative potential is exhausted (> 3 % Ro). This occurs at temperatures in excess of 200 ^{o}C (Hall *et al.,* 2016).

It should be noted that the oil and gas generation cycle, as presented above, is much simplified, and petroleum basins vary in terms of hydrocarbon generation conditions. In fact, each basin has its specific thermodynamical conditions, different type of organic

matter distributed within the rocks, different rock-building minerals, different burial rates and several other factors (Hall *et al.*, 2016).

The plots of T_{max} versus HI (Fig. 3.18), T_{max} versus Ro (Fig. 3.19) and C_{32} 22S/(22S+22R) homohopane versus C_{29} (ßß/ßß+αα) sterane (Fig. 3.20) are used to determine the level of maturation for the black shales of the Al Jurf Formation. Generally, all organic matter is thermally mature. A small contribution of immature organic matter is also observed in the black shales.

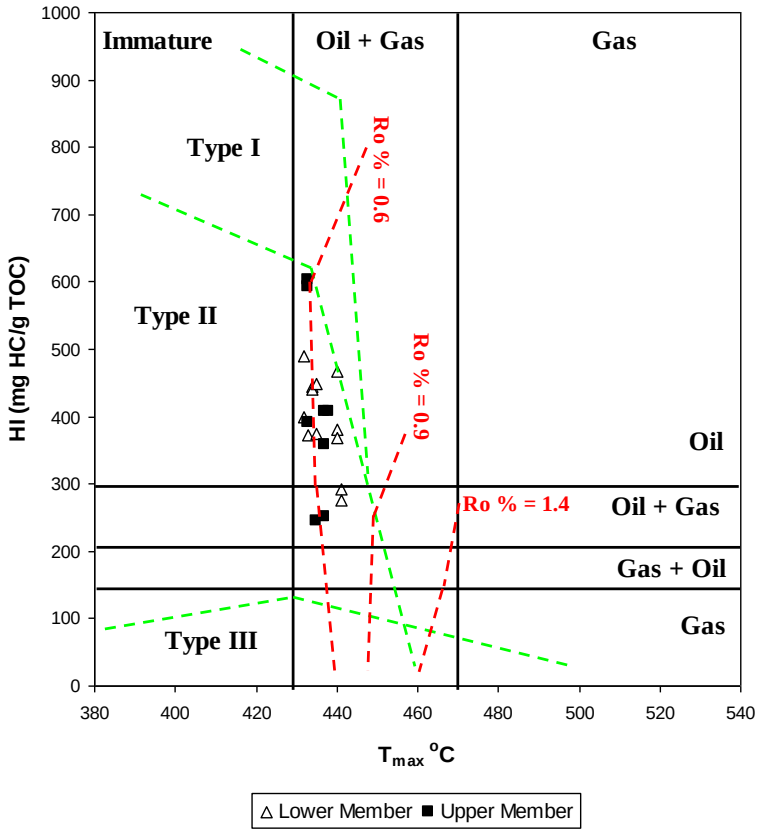

Fig. 3.18: Plot of T_{max} vs. HI showing the thermal maturity for the studied black shales (fields after Hall et al., 2016).

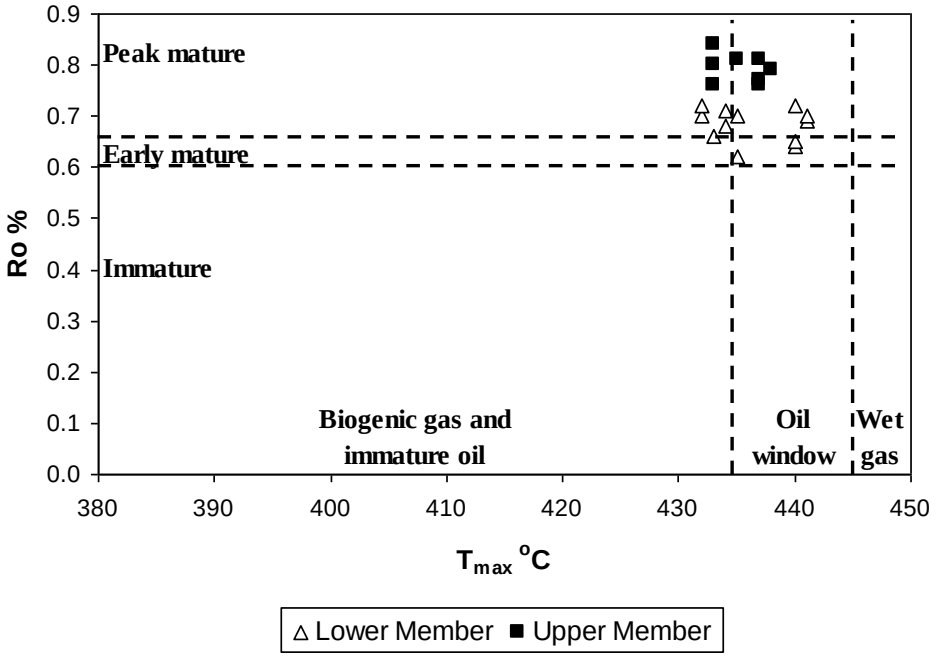

Fig. 3.19: Plot of T_{max} vs. Ro showing the thermal maturity for the studied black shales (fields after Atta-Peters and Garrey, 2014).

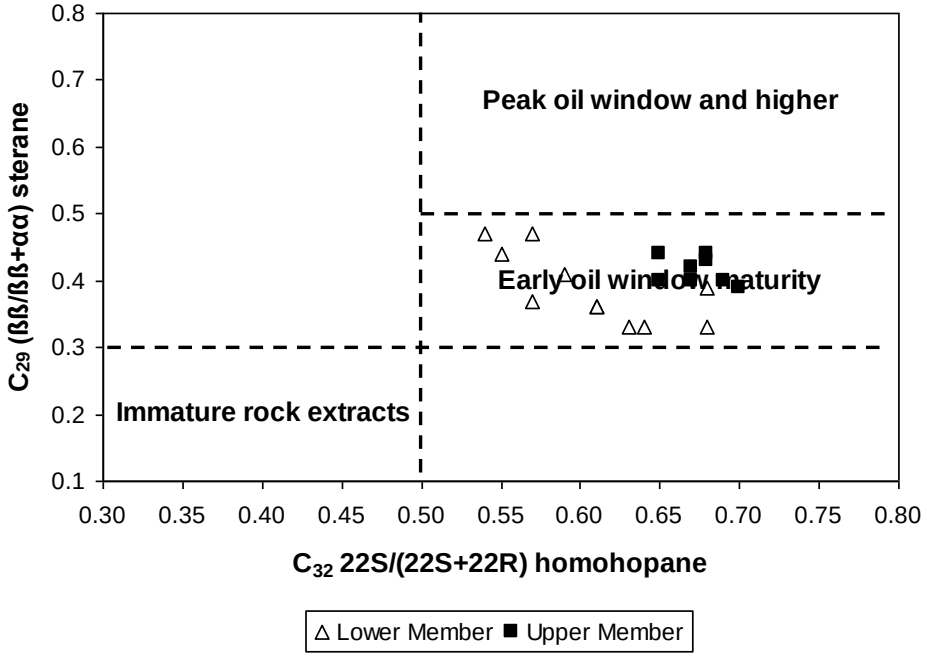

Fig. 3.20: Plot of C_{32} 22S/(22S+22R) homohopane vs. C_{29} (ßß/ßß+αα) sterane showing the thermal maturity for the studied shales (fields after Peters and Moldowan, 1993).

3.3.4. Status of Hydrocarbons

Using the plot of TOC versus S_1, Hunt (1996) classified the status of hydrocarbons into two types, namely nonindigenous (migrated) hydrocarbons and indigenous (generated) hydrocarbons. Fig (3.21) shows that all black shales fall in the field of nonindigenous hydrocarbons.

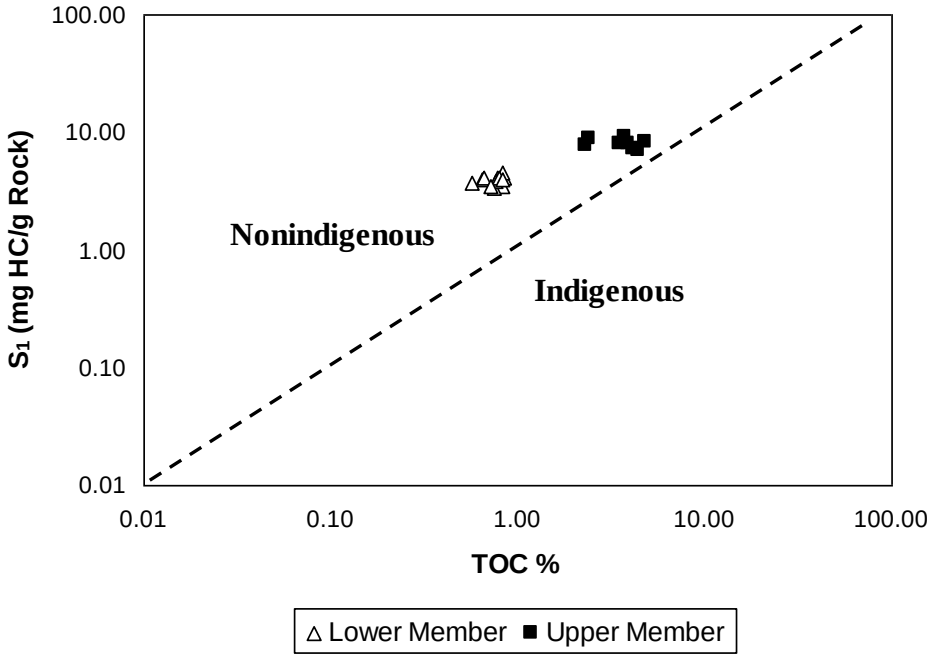

Fig. 3.21: Plot of TOC vs. S_1 showing the status of hydrocarbons for the studied black shales (fields after Hunt, 1996).

3.3.5. Organic Matter Origin and Depositional Environment

The Pr/Ph ratio is a familiar proxy to evaluate paleoredox condition (Brooks *et al.*, 1969 and Didyk *et al.*, 1978). Phytol originated from chlorophyll is known to be altered to pristane (C_{19}) via oxidation and decarboxylation by diagenetic processes under oxic conditions, or to phytane (C_{20}) after dehydration under anoxic conditions (Didyk *et al.*, 1978). Such difference in alteration processes is basically thought as main factors of changing Pr/Ph ratios in the sediments. Moreover, the Pr/Ph values increase with excess input of terrestrial organic matter, and even pelagic sediments influenced by allochthonous terrigenous matter have higher Pr/Ph values. In addition, tocopherols (vitamin E), which

marine and terrestrial photoautotroph organisms ubiquitously biosynthesize, are potential precursors of pristane (Goossens *et al.*, 1984 and Rontani *et al.*, 2010). The phytane could also be produced by degradation of archeal lipid, namely diphytanyl glyceryl ether, during thermal maturation (Pease *et al.*, 1998 and Rontani *et al.*, 2013). Thermal maturity simulation shows that the Pr/Ph ratio also tends to increase during early diagenesis (Koopmans *et al.*, 1999). In general, biomarkers are used to determine the organic matter input, redox condition, depositional environment and paleosalinity (Huang and Meinschein, 1979; Shanmugam, 1985; Peters *et al.*, 2005; Zhou and Huang, 2008; El Diasty and Moldowan, 2012; Yandoka *et al.*, 2015 and Shaltami *et al.*, 2019).

In the current study, several models (Figs. 3.22-3.33) using biomarkers clearly suggest that the studied black shales contain mixed organic matter. Furthermore, the black shales were deposited under suboxic marine environment with a high degree of salinity.

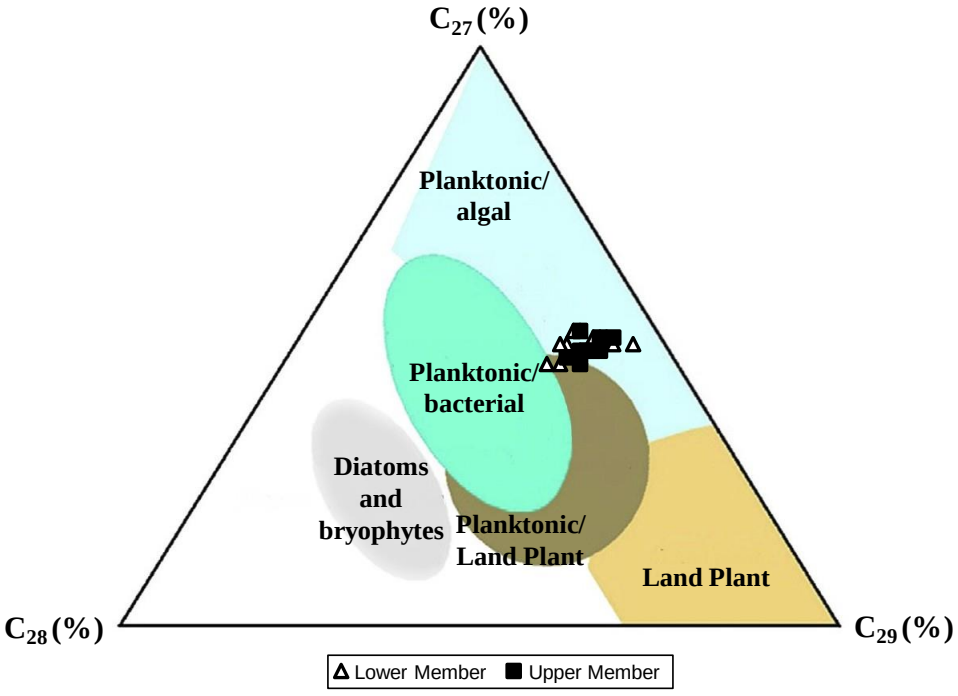

Fig. 3.22: Ternary diagram of C_{27}-C_{28}-C_{29} regular steranes showing the organic matter origin for the studied black shales (fields after Huang and Meinschein, 1979).

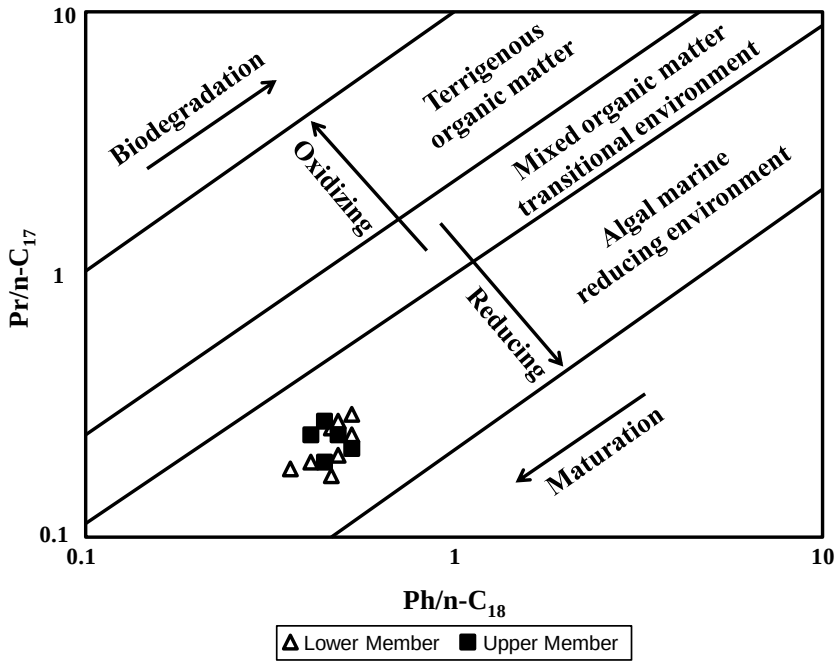

Fig. 3.23: Plot of Ph/n-C_{18} vs. Pr/n-C_{17} showing the organic matter origin and redox conditions for the studied black shales (fields after Shanmugam, 1985).

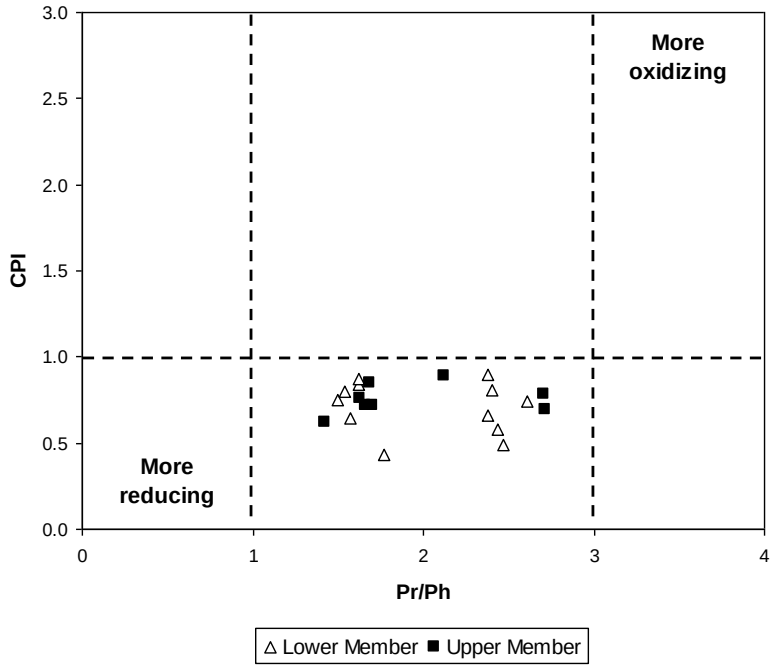

Fig. 3.24: Plot of Pr/Ph vs. CPI showing the organic matter origin and redox conditions for the studied black shales (fields after Akinlua et al., 2007).

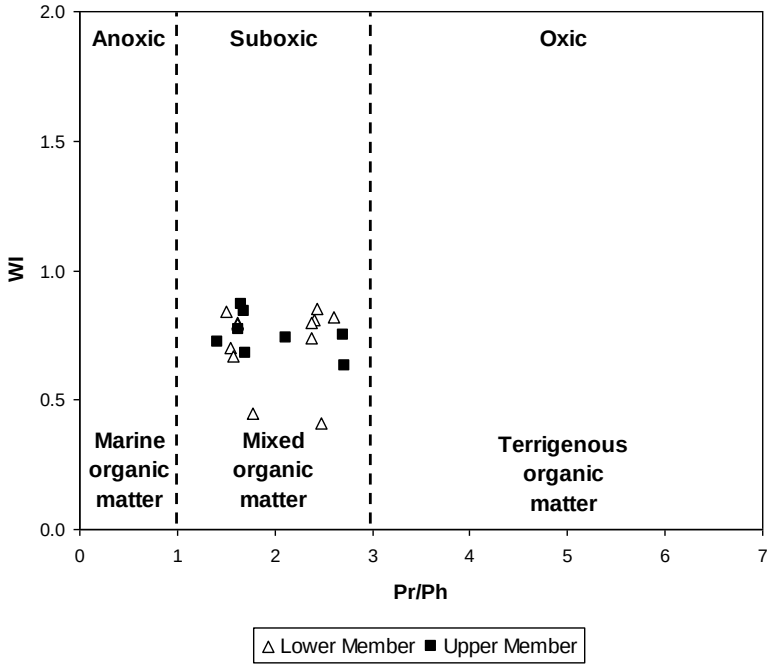

Fig. 3.25: Plot of Pr/Ph vs. WI showing the organic matter origin and redox conditions for the studied black shales (fields after El Diasty and Moldowan, 2012).

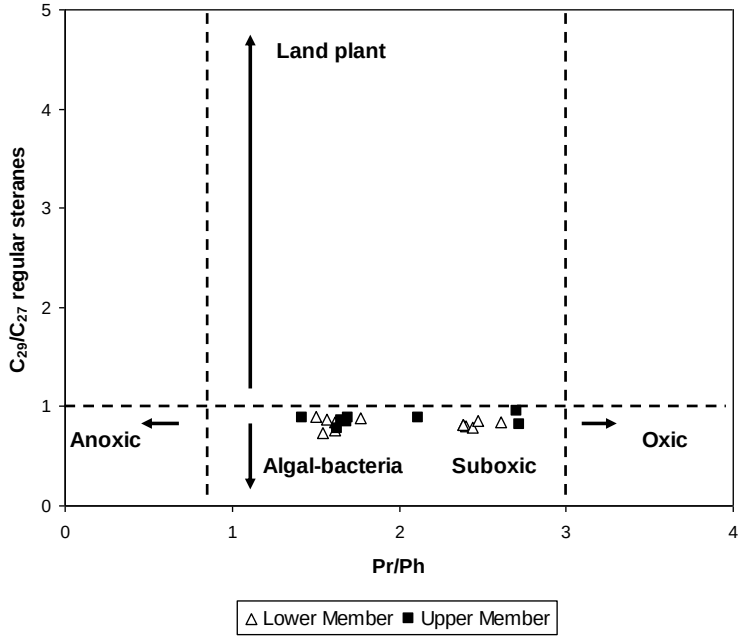

Fig. 3.26: Plot of Pr/Ph vs. C_{29}/C_{27} regular steranes showing the organic matter origin and redox conditions for the studied black shales (fields after Yandoka et al., 2015).

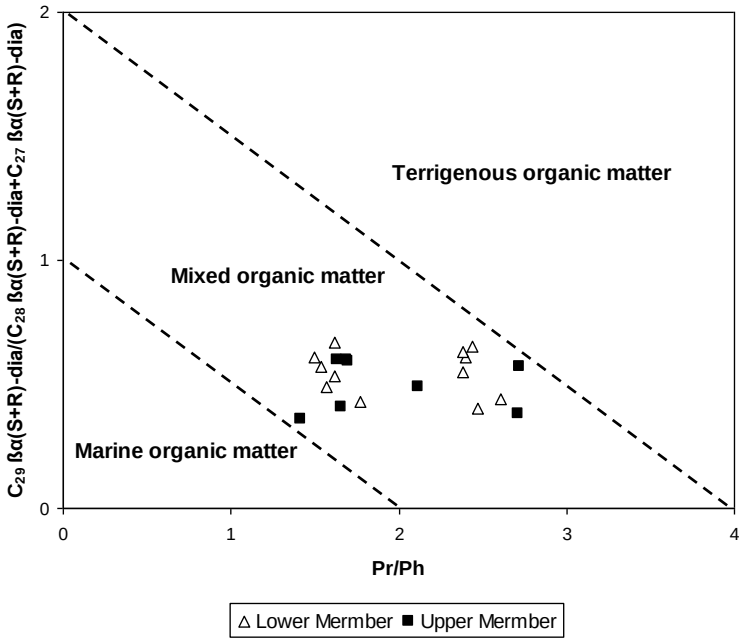

Fig. 3.27: Plot of Pr/Ph vs. predominance of C_{29} -components amongst diasteranes showing the organic matter origin for the studied black shales (fields after Shaltami et al., 2019).

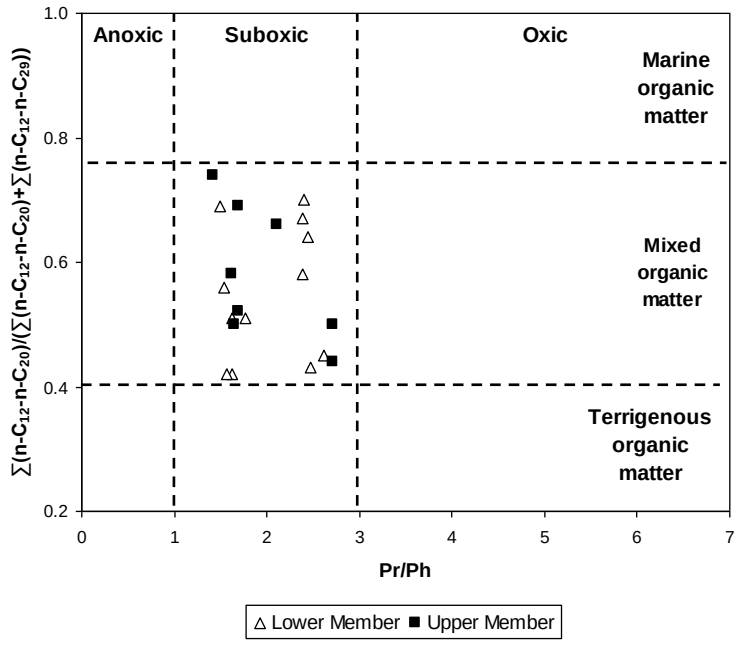

Fig. 3.28: Plot of Pr/Ph vs. n-alkane SLR (Σn-C_{12-20})/(Σn-C_{12-29}) showing the organic matter origin and redox conditions for the studied black shales (fields after Shaltami et al., 2019).

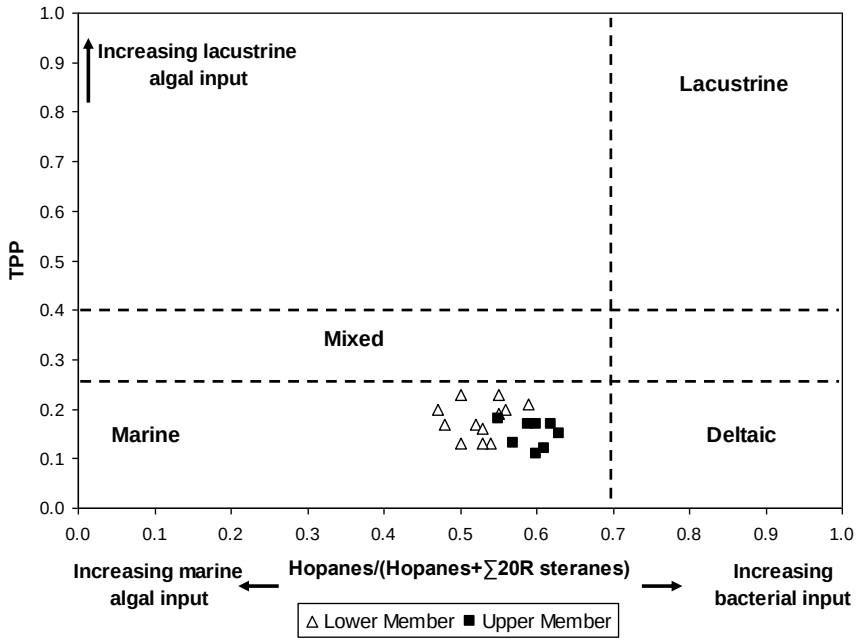

Fig. 3.29: Plot of TPP vs. hopane/(hopanes+Σ20R steranes) showing the depositional environment of the studied black shales (fields after Holba et al., 2003).

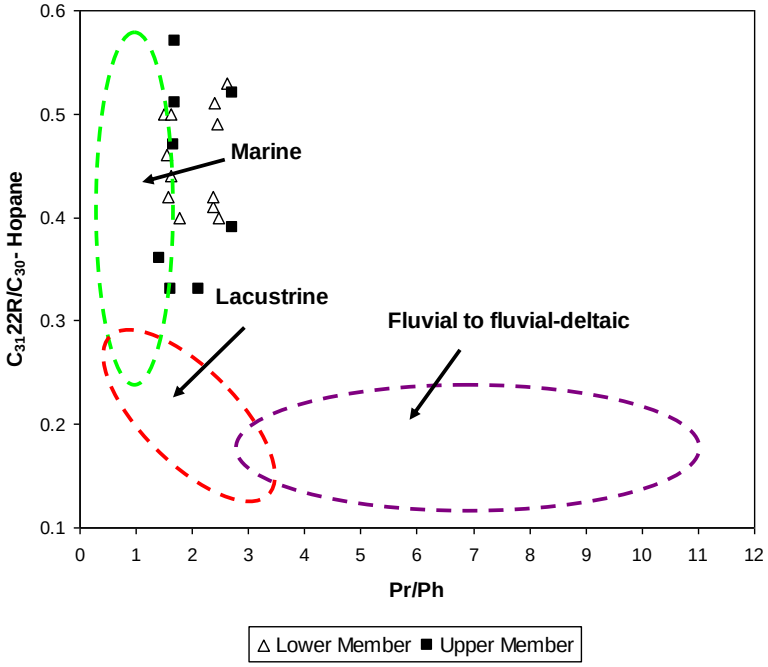

Fig. 3.30: Plot of Pr/Ph vs. $C_{31}R/C_{30}$ hopane showing the depositional environment of the studied black shales (fields after Peters et al., 2005).

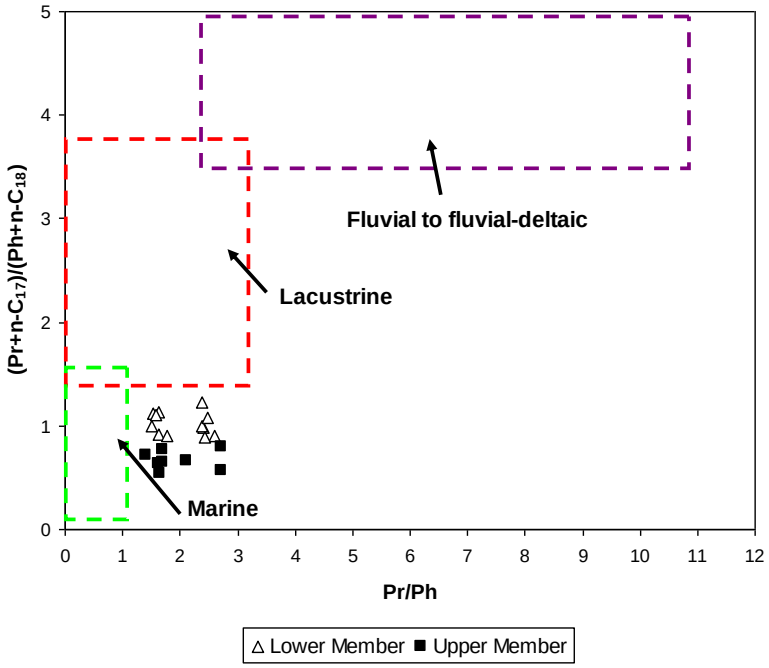

Fig. 3.31: Plot of Pr/Ph vs. (Pr+n-C_{17})/(Ph+n-C_{18}) showing the depositional environment of the studied black shales (fields after Shaltami et al., 2019).

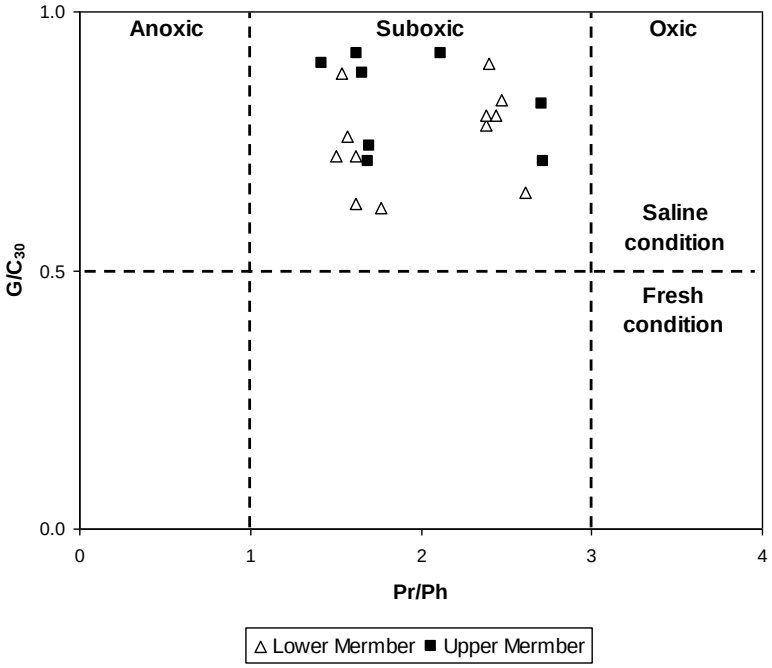

Fig. 3.32: Plot of Pr/Ph vs. G/C_{30} showing the paleosalinity and redox conditions for the studied black shales (fields after Zhou and Huang, 2008).

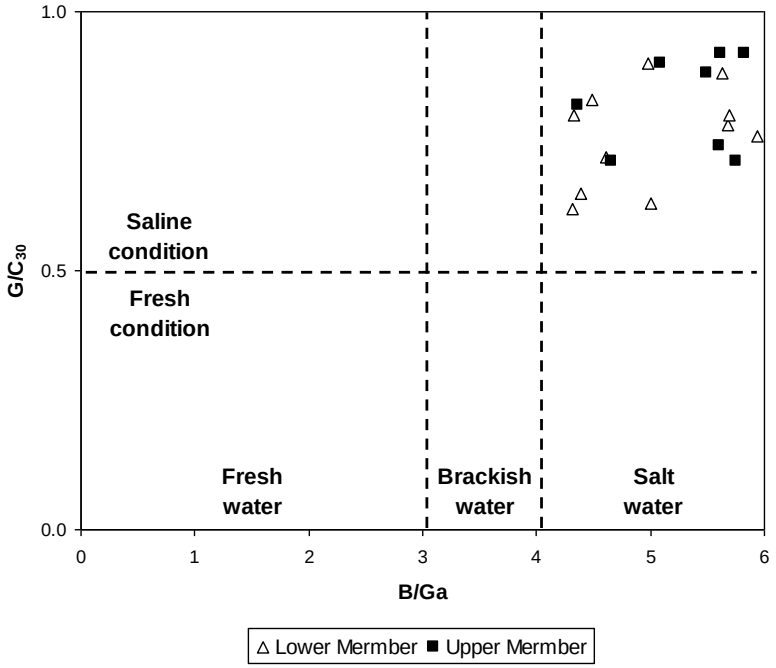

Fig. 3.33: Plot of B/Ga vs. G/C_{30} showing the paleosalinity for the studied black shales (fields after Deng and Qian, 1993; Zhou and Huang, 2008).

CHAPTER FOUR
CONCLUSIONS

Using several techniques such as organic petrographic microscope, inductively coupled plasma mass spectrometer (ICP-MS), source rock analyzer (SRA) and gas chromatography-mass spectrometry (GC-MS), a petrographical and geochemical evaluation was carried out of the black shales of the Al Jurf Formation in the offshore well C-NC 41, Sabratah Basin, NW Libya. Ten conclusions were reached:

1) The detected clay minerals in the black shales are smectite, illite, kaolinite, gibbsite, chlorite and mixed layer clays. These minerals are the main carrier of TOC.

2) The weathering indices (CIA, CIW, CIW´ and PIA) suggesting high degree of chemical weathering in the source area.

3) The low ICV values (< 1) indicating the maturation of the black shales.

4) The climatic discrimination diagrams show that the semi-humid climate is dominant in the source area.

5) The observed macerals in the black shales are vitrinite (collotelinite and vitrodetrinite), liptinite (resinite, cutinite, sporinite and alginite) and inertinite (fusinite and inertodetrinite).

6) The black shale of the Upper Member has very good to excellent quality, whereas the black shale of the Lower Member is a fair source rock.

7) The black shales contain two types of kerogen (II and II/III).

8) Generally, all organic matter is thermally mature.

9) The black shales contain nonindigenous hydrocarbons.

10) The biomarkers and the trace element ratios suggest that the Al Jurf Formation was deposited in a suboxic marine environment with a high degree of salinity.

REFERENCES

Akinlua, A., Ajayi, T.R. and Adeleke, B.B. (2007): Organic and inorganic geochemistry of northwestern Niger Delta oils. Geochemical Journal; 41: 271-281.

Algeo, T.J. and Maynard, J.B. (2004): Trace-element behavior and redox facies in core shales of Upper Pennsylvanian Kansas-type cyclothems. Chemical Geology; 206: 289-318.

Anketell, J.M. and Mriheel, I.Y. (2000): Depositional environment and diagenesis of the Eocene Jdeir Formation, Gabes-Tripoli Basin, western offshore, Libya. Journal of Petroleum Geology; 23: 425-447.

Armstrong-Altrin, J.S., Lee, Y.I., Verma, S.P. and Ramasamy, S. (2004): Geochemistry of sandstones from the Upper Miocene Kudankulam Formation, southern India: implication for provenance, weathering and tectonic setting. Journal of Sedimentary Research; 74: 285-297.

Atta-Peters, D. and Garrey, P. (2014): Source rock evaluation and hydrocarbon potential in the Tano basin, South Western Ghana, West Africa. International Journal of Oil, Gas and Coal Engineering; 2(5): 66-77.

Bailey, H.W., Dungworth, G., Hardy, M., Scull, D. and Vaughan, R.D. (1989): A fresh approach to the Metlaoui. Actes des IIeme journees de geologie tunisienne appliquee a la recherche des hydrocarbures. Mem. ETAP, No. 3, Tunis, pp. 281-307.

Baioumy, H.M., Ahmedb, A.H. and Khed, M.Z. (2014): A mixed hydrogenous and hydrothermal origin of the Bahariya iron ores, Egypt: Evidences from the trace and rare earth element geochemistry. Journal of Geochemical Exploration; 146: 149-162.

Baiyegunhi, C., Liu, K. and Gwavava, O. (2017): Geochemistry of sandstones and shales from the Ecca Group, Karoo Supergroup, in the Eastern Cape Province of South Africa: Implications for provenance, weathering and tectonic setting. Open Geosciences; 9:340-360.

Bau, M. and Alexander, B.W. (2009): Distribution of high field strength elements (Y, Zr, REE, Hf, Ta, Th, U) in adjacent magnetite and chert bands and in reference standards FeR-3 and FeR-4 from the Temagami iron-formation, Canada, and the redox level of the Neoarchean ocean. Precambrian Research; 174: 337-346.

Belkin, H.E., Tewalt, S.J., Hower, J.C., Stucker, J.D., O'Keefe, J.M.K., Tatu, C.A. and Buia, G. (2010): Petrography and geochemistry of Oligocene bituminous coal from the Jiu Valley, Petroşani basin (southern Carpathian Mountains), Romania. International Journal of Coal Geology; 82(1-2): 68-80.

Bernasconi, A., Poliani, G. and Dakshe, A. (1991): Sedimentology, petrography and diagenesis of Metlaoui Group in the offshore northwest of Tripoli. Third Symposium on the Geology of Libya, vol. 5. (eds. M.J. Salem and M.N. Belaid), Elsevier, Amsterdam, pp. 1907-1928.

Bhatia, M.R. (1983): Plate tectonics and geochemical composition of sandstones. Journal of Geology; 92: 181-193.

Bishop, W.F. (1988): Petroleum Geology of east-central Tunisia. Bulletin-AAPG; 72: 1033-1058.

Brooks, J.D., Gould, K. and Smith, J.W. (1969): Isoprenoid hydrocarbons in coal and petroleum. Nature; 222: 257-259.

Cavelan, A., Boussafir, M., Rozenbaum, O. and Laggoun-Defarge, F. (2019): Organic petrography and pore structure characterization of low-mature and gas-mature marine

organic-rich mudstones: Insights into porosity controls in gas shale systems. Marine and Petroleum Geology; 103: 331-350.

Claes, H., Huysmans, M., Soete, J., Dirix, K., Vassilieva, E., Erthal, M.M., Vandewijngaerde, W., Hamaekers, H., Aratman, C., Ozkul, M. and Swennen, R. (2019): Elemental geochemistry to complement stable isotope data of fossil travertine: Importance of digestion method and statistics. Sedimentary Geology; 386: 118-131.

Cox, R., Low, D.R. and Cullers, R.L. (1995): The influence of sediment recycling and basement composition on evolution of mudrock chemistry in the southwestern United States. Geochimica et Cosmochimica Acta; 59: 2919-2940.

Cullers, R.L. and Podkovyrov, V.N. (2000): Geochemistry of the Mesoproterozoic Lakhanda shales in southeastern Yakutia, Russia: implications for mineralogical and provenance control, and recycling. Precambrian Research; 104(1-2): 77-93.

Cumberland, S.A., Douglas, G., Grice, K. and Moreau, J.W. (2016): Uranium mobility in organic matter-rich sediments: A review of geological and geochemical processes. Earth-Science Reviews; 159: 160-185.

Curiale, J.A. and Curtis, J.B. (2016): Organic geochemical applications to the exploration for source-rock reservoirs – A review. Journal of Unconventional Oil and Gas Resources; 13: 1-31.

Dai, S.F., Li, D., Chou, C.L., Zhao, L., Zhang, Y., Ren, D.Y., Ma, Y.W. and Sun, Y.Y. (2008): Mineralogy and geochemistry of boehmite-rich coals: new insights from the Haerwusu Surface Mine, Jungar Coalfield, Inner Mongolia, China. International Journal of Coal Geology; 74: 185-202.

Dean, W.E., Piper, D.Z. and Peterson, L.C. (1999): Molybdenum accumulation in Cariaco basin sediment over the past 24 k.y.: a record of water-column anoxia and climate. Geology; 27: 507-510.

Dembicki, H.J. (2009): Three common source rock evaluation errors made by geologists during prospect or play appraisals. AAPG Bulletin; 93(3): 341-356.

Deng, H.W. and Qian, K. (1993): Sedimentary geochemistry and environment analysis. Lanzhou: Gansu Science and Technology Press.

Dianshi, D., Guijian, L., Biao, F. and Cuicui, Q. (2019): Characteristics of the coal quality and elemental geochemistry in Permian coals from the Xinjier mine in the Huainan Coalfield, north China: Influence of terrigenous inputs. Journal of Geochemical Exploration; 186: 50-60.

Didyk, B.M., Simoneit, B.R.T., Brassell, S.C. and Eglinton, G. (1978): Organic geochemical indicators of paleoenvironmental conditions of sedimentation. Nature; 272: 216-222.

El Diasty, W.S. and Moldowan, J.M. (2012): Application of biological markers in the recognition of the geochemical characteristics of some crude oils from Abu Gharadig Basin, north Western Desert–Egypt. Marine and Petroleum Geology; 35:28-40.

Fedo, C.M., Nesbitt, H.W. and Young, G.M. (1995): Unraveling the effects of potassium metasomatism in sedimentary rocks and paleosols, with implications for paleoweathering conditions and provenance. Geology; 23: 921-924.

Flores, D., Pereira, L.C.G., Ribeiro, J., Pina, B., Marques, M.M., Ribeiro, M.A., Bobos, I. and de Jesus, A.P. (2010): The Buçaco Basin (Portugal): Organic petrology and geochemistry study. International Journal of Coal Geology; 81(4): 281-286.

Fornaciari, M. (2007): Petroleum geology in the NC 41 area (Western Libyan offshore). 3rd EAGE North African/Mediterranean Petroleum and Geosciences Conference and Exhibition, Tripoli extended abstract.

Furmann, A., Mastalerz, M., Brassell, S.C., Pedersen, P.K., Zajac, N.A. and Schimmelmann, A. (2015): Organic matter geochemistry and petrography of Late Cretaceous (Cenomanian-Turonian) organic-rich shales from the Belle Fourche and Second White Specks formations, west-central Alberta, Canada. Organic Geochemistry; 85: 102-120.

Ghori, K.A.R. (2002): Modeling the hydrocarbon generative history of the Officer Basin, Western Australia. Journal of Philosophy of Education Society of Australasia (PESA); 29: 29-42.

Goossens, H., De Leeuw, J.W., Schenck, P.A. and Brassell, S.C. (1984): Tocopherols as likely precursors of pristane in ancient sediments and crude oils. Nature: 312: 440-442.

Hall, L.S., Boreham, C.J., Edwards, D.S., Palu, T.J., Buckler, T., Hill, A.J. and Troup, A. (2016): Cooper Basin source rock geochemistry: Regional hydrocarbon prospectivity of the Cooper Basin. Geoscience Australia, Part2; 62p.

Hallett, D. (2002): Petroleum geology of Libya. Amsterdam, Elsevier Inc., 503p.

Hallett, D. and Clark-Lowes, D. (2016): Petroleum geology of Libya. 2nd edition, Amsterdam, Elsevier Inc., 404p.

Hammuda, O.S., Sbeta, A.M., Mouzughi, A.J. and Eliagoubi, B.A. (1985): Stratigraphic nomenclature of the northwestern offshore of Libya. Earth Sciences Society of Libya, 166p.

Haq, B.U., Hardenbol, J. and Vail, P.R. (1988): Mesozoic and Cenozoic chronostratigraphy and eustatic cycles. SEPM Special Publication vol. 42. (eds. C.K. Wilgus, H. Posamentier, C.K. Ross, C.G.S. Kendall), Sea-Level Changes: An Integrated Approach, pp. 71-108.

Hassan, H.H. and Kendall, C. (2014): Hydrocarbon provinces of Libya: A petroleum system study. (eds. L. Marlow, C. Kendall, L. Yose), Petroleum Systems of the Tethyan Region. American Association of Petroleum Geologists, Tulsa, pp. 101-141 Memoir No. 106.

He, J., Zhou, Y. and Li, H. (2011): Study on geochemical characteristics and depositional environment of Pengcuolin chert, Southern Tibet. Journal of Geography and Geology; 3(1): 178- 188.

Holba, A.G., Dzoub, L.I., Wood, G.D., Ellisd, L., Adame, P., Schaeffere, P., Albrechte, P., Greenef, T. and Hughes, W.B. (2003): Application of tetracyclic polyprenoids as indicators of input from fresh-brackish water environments. Organic Geochemistry; 34: 441-469.

Huang, W.Y. and Meinschein, W.G. (1979): Sterols as ecological indicators. Geochimica et Cosmochimica Acta; 43: 739-745.

Hunt, J.M. (1996): Petroleum geochemistry and geology, 2nd edition, vol. 743. New York: Freeman and Company.

Jones, B. and Manning, D.C. (1994): Comparison of geochemical indices used for the interpretation of paleo-redox conditions in Ancient mudstones: Chemical Geology; 111(1-4): 111-129.

Jubb, A.M., Botterell, P.J., Birdwell, J.E., Burruss, R.C., Hackley, P.C., Valentine, B.J., Hatcherian, J.J. and Wilson, S.A. (2018): High microscale variability in Raman thermal

maturity estimates from shale organic matter. International Journal of Coal Geology; 199: 1-9.

Kaufman, R.L., Ahmed, A.S. and Elsinger, R.J. (1990): Gas chromatography as a development and production tool for fingerprinting oils from individual reservoirs: applications in the Gulf of Mexico. GCSSEPM Foundation Ninth Annual Research Conference Proceedings; pp. 263-282.

Kok, M.V., Senguler, I., Hufnagel, H. and Sonel, N. (2001): Thermal and geochemical investigation of Seyitomer oil shale. Thermochimica Acta; 371(1-2): 111-119.

Koopmans, M.P., Rijpstra, W.I.C., Klapwijk, M.M., De Leeuw, J.W., Lewan, M. D. and Damste, J.S.S. (1999): A thermal and chemical degradation approach to decipher pristane and phytane precursors in sedimentary organic matter. Organic Geochemistry; 30: 1089-1104.

Kruszewska, K.J. (2003): Fluorescing macerals in South African coals. International Journal of Coal Geology; 54(1-2): 79-94.

Kvenvolden, K.A. (2006): Organic geochemistry – A retrospective of its first 70 years. Organic Geochemistry; 37(1): 1-11.

Liu, L.F. and Lee, Y.J. (2001): Geochemistry of source rocks in the lower Tertiary Nadu Formation, Eastern Depression of the Baise Bas in, Guangxi Province, China. Journal of Petroleum Science and Engineering; 41: 135-157.

Longford, F.F. and Blanc-Valleron, M.M. (1990): Interpreting Rock–Eval pyrolysis data using graphs of pyrolyzable hydrocarbons vs. total organic carbon, AAPG Bulletin; 74: 799-804.

McLennan, S.M., Hemming, S.R., McDaniel, D.K. and Hanson, G.N. (1993): Geochemical approaches to sedimentat ion, provenance, and tectonics. In: Johnsson, M.J., Basu, A. (Eds.), Processes controlling the composition of clastic sediments. Special Papers-Geological Society of America; 284: 21-40.

Morgan, J.W. and Heier, K.S. (1966): Uranium, thorium and potassium in six U.S.G.S. standard rocks. Earth and Planetary Science Letters; 1: 158-160.

Nabbefeld, B. Grice, K., Schimmelmann, A., Summons, R.E., Troitzsch, U. and Twitchett, R.J. (2010): A comparison of thermal maturity parameters between freely extracted hydrocarbons (Bitumen I) and a second extract (Bitumen II) from within the kerogen matrix of Permian and Triassic sedimentary rocks. Organic Geochemistry; 41(2): 78-87.

Nagarajan, R.; Madhavaraju, J.; Nagendra, R.; Armstrong-Altrin, J.S. and Moutte, J. (2007): Geochemistry of Neoproterozoic shales of the Rabanpalli Formation, Bhima Basin, Northern Karnataka, southern India: implications for provenance and paleoredox conditions. Revista Mexicana de Ciencias Geologicas; 24 (2): 150-160.

Nath, B.N., Bau, M., Ramlingeswara-Rao, B. and Rao, C.M., (1997): Trace and rare earth elemental variation in Arabian Sea sediments through a transect across the oxygen minimum zone. Geochimica et Cosmochimica Acta; 61: 2375-2388.

Ndip, E.A., Agyingi, C.M., Nton, M.E., Hower, J.C. and Oladunjoye, M.A. (2019): Organic petrography and petroleum source rock evaluation of the Cretaceous Mamfe Formation, Mamfe basin, southwest Cameroon. International Journal of Coal Geology; 202: 27-37.

Nesbitt, H.W., Markovics, G. and Price, R.C. (1980): Chemical processes affecting alkalis and alkaline earths during continental weathering. Geochimica et Cosmochimica Acta; 44: 1659-1666.

Nesbitt, H.W. and Young, G.M. (1982): Early Proterozoic climates and plate motions inferred from major element chemistry of lutites. Nature; 299: 715-717.

Nesbitt, H.W. and Young, G.M. (1984): Prediction of some weathering trends of plutonic and volcanic rocks based upon thermodynamic and kinetic consideration. Geochimica et Cosmochimica Acta; 48: 1523-1534.

Pease, T.K., Van Vleet, E.S., Barre, J.S. and Dickins, H.D. (1998): Simulated degradation of glyceryl ethers by hydrous and flash pyrolysis. Organic Geochemistry; 29: 979-988.

Peters, K.E. and Cassa, M.R. (1994): Applied source rock geochemistry. In: Magoon, L.B., Dow, W.G. (Eds.): The petroleum system from source to trap, AAPG, Mem.; 60: 93-117.

Peters, K.E. and Moldowan, J.M. (1993): The biomarker guide: Interpreting molecular fossils in petroleum and ancient sediments. Prentice-Hall, Inc, Englewood Cliffs, New Jersey.

Peters, K.E., Walters, C.C. and Moldowan, J.M. (2005): The biomarker guide: Biomarkers and isotopes in petroleum exploration and Earth history. 2nd edition, vol. 2. Cambridge University Press, Cambridge.

Pratt, L.M. and Davis, C.L. (1992): Intertwined fates of metals, sulfur, and organic carbon in black shales. In: Pratt, L.M., Comer, J.B., Brassell, S.C. (Eds.), Geochemistry of Organic Matter in Sediments and Sedimentary Rocks. SEPM Short Course Notes; 27: 1-27.

Racey, A., Bailey, H.W., Beckett, D., Gallagher, L.T., Hampton, M.J. and Mcquilken, J. (2001): The petroleum geology of the Early Eocene El Garia Formation, Hasdrubal field, offshore Tunisia. Journal of Petroleum Geology; 24: 29-53.

Ricchiuto, T. and Pajola, M. (2003): Libya NC 41: Integration of chemical and isotopic analyses. Second Symposium on the Sedimentary Basins of Libya, The geology of northwest Libya, vol. 3. (eds. M.J. Salem, K.M. Oun and H.M. Seddiq), Earth Science Society of Libya, Tripoli, pp. 55-64.

Rontani, J.F., Bonin, P., Vaultier, F., Guasco, S. and Volkman, J.K. (2013): Anaerobic bacterial degradation of pristenes and phytenes in marine sediments does not lead to pristane and phytane during early diagenesis. Organic Geochemistry: 58: 43-55.

Rontani, J.F., Nassiry, M., Michotey, V., Guasco, S. and Bonin, P. (2010): Formation of pristane from α-tocopherol under simulated anoxic sedimentary conditions: a combination of biotic and abiotic degradative processes. Geochimica et Cosmochimica Acta; 74: 252-263.

Roser, B.P. and Korsch, R.J. (1988): Provenance signatures of sandstone–mudstone suites determined using discriminant function analysis of major-element data. Chemical Geology; 67: 119-139.

Roy, D.K. and Roser, B.P. (2013): Climatic control on the composition of Carboniferous-Permian Gondwana sediments, Khalaspir basin, Bangladesh. Gondwana Research; 23: 1163-1171.

Sbeta, A.M. (1990): Stratigraphy and lithofacies of Farwah Group and its equivalent: offshore NW Libya. Journal of Petroleum Research (Tripoli); 2: 42-56.

Shaltami, O.R. (2012): Mineral composition and environmental geochemistry of the beach sediments along the Mediterranean Coast from Benghazi to Bin Jawwad, Northeast Libya. Unpublished PhD Thesis, Cairo University, Egypt.

Shaltami, O.R., Fares, F.F. and Bustany, I. (2016): Geochemistry of Mamuniyat Formation, Idri area, SW Libya. 11th International Conference and Meeting on Geology, Institute of Geosciences, University of Campinas, Brazil, Proceeding Book; pp. 88-102.

Shaltami, O.R., Fares, F.F., EL Oshebi, F.M., Errishi, H. and Souza, R. (2018): Geochemistry of the terra rossa in the Al Jabal Al Akhdar, NE Libya: Implications on provenance, paleoclimate, paleoweathering, paleooxygenation and tectonic setting. Geoinformatics 2018, Kiev, Ukraine, Proceeding Book; pp. 28-45.

Shaltami, O.R., Liu, Y., Jorgensen, L., Elkjaer, C., Fares, F.F., Errishi, H., EL Oshebi, F.M. and Souza, R. (2019): Organic geochemistry of shale and marl: A case study of the Miocene deposits in the Cyrenaica Basin, NE Libya. World Chemistry 2019, Philadelphia, USA, Proceeding Book; pp. 70-82.

Shanmugam, G. (1985): Significance of coniferous rain forests and related organic matter in generating commercial quantities of oil, Gippsland Basin, Australia. American Association of Petroleum Geologists Bulletin; 69: 1241-1254.

Sun, L.H., Gui, H.R. and Chen, S. (2012): Geochemistry of sandstones from the Neoproterozoic Shijia Formation, northern Anhui Province, China: implications for provenance, weathering and tectonic setting. Chemie der Erde-Geochemistry; 72: 253-260.

Suttner, L.J. and Dutta, P.K. (1986): Alluvial sandstone composition and paleoclimate. Framework mineralogy. Journal of Sedimentary Petrology; 56: 326-345.

Van Krevelen, D.W. (1961): Coal: typology-chemistry-physics-constitution: Elsevier Science, Amsterdam; 514p.

Wood, D.A. (1980): The application of the Th-Hf-Ta diagram to problems of tectonomagmatic classification and establishing the nature of crustal contamination of

Basaltic Lava of the British Tertiary Volcanic Province. Earth and Planetary Science; Letters: 50: 11-30.

Xiaodong, F., Jianzhong, Q., Tenger, D. and Xiaofang, W. (2011) Mineral components of source rocks and their petroleum significance: A case from Paleozoic marine source rocks in the Middle-Upper Yangtze region. Petroleum Exploration and Development; 38(6): 671-684.

Yandoka, B.M.S., Abdullah, W.H., Abubakar, M.B., Hakimi, M.H. and Adegoke, A.K. (2015): Geochemical characterisation of Early Cretaceous lacustrine sediments of Bima Formation, Yola Sub-basin, Northern Benue Trough, NE Nigeria: Organic matter input, preservation, paleoenvironment and palaeoclimatic conditions. Marine and Petroleum Geology; 61: 82-94.

Yao, C., Guo, W., Liu, J. and Li, H. (2017): Multiple proxies on the paleoenvironment of the Early Cambrian marine black rock series in the Tarim Basin, NW China: Molybdenum isotope and trace element evidence. International Journal of Geosciences; 8: 965-983.

Yao, Z., Yang Y., Ying H. and Dong Y. (2014): Mineral characteristics and their geological significance of black shales in southeastern Ordos Basin by X-ray diffraction analysis. Chinese Journal of Geochemistry; 33:119-124.

Zhou, S. and Huang, H. (2008): Controls on alkylphenol occurrence and distribution in oils from lacustrine rift basins in East China. Science in China Series D: Earth Sciences; 51(7): 976-983.

جيوكيمياء صخور المصدر لتكوين الجرف في البئر البحري س – ن س 41، بحوض صبراته، شمال غرب ليبيا

قدمت من قبل :

ابراهيم عبدالهادى محمد التيكالى

تحت إشراف :

د. أسامة الشلطامي

الملخص

ان الهدف من هذا العمل هو التقييم البتروغرافي والجيوكيميائي لطبقات الطين السوداء من التكوين الجرف في البئر البحري س– ن س 41، حوض صبراتة، شمال غرب ليبيا. بصوره عامه، تعتبر صخور الطين السوداء للطبقة العلويه بمثابة صخور مصدر جيدة جدًا إلى ممتازة، بينما يتمتع الصخر الزيتي للطبقة السفليه بجودة جيدة. تعتبر معادن الطين الرئيسية هي (سمكتايت – إلايت – كوليونايت – جبسايت – كلورايت– طبقات الطين المختلطة). تعتبر صخور الطين السوداء رواسب ناضجة (ICV < 1) يسوده مناخ شبه رطب أثناء الترسيب. تحتوي صخور الطين السوداء على نسبة عالية من فيترينيت وليبتينيت، مع كميات أقل من القصور الذاتي. المواد العضوية ناضجة حرارياً. الكيروجين من النوع الثاني – الثاني / الثالث هم الغالب في الصخر الزيتي. البيئة الترسبية المؤكدة لتشكيل الجرف هي البحرية تحت الظروف المؤكسدة.

الكلمات الدالة:

الصخور العضوية ، علم الجيوكيمياء، صخور المصدر ، تكوين الجرف ، حوض صبراته ، ليبيا.

جيوكيمياء صخور المصدر لتكوين الجرف في البئر البحري س – ن س 41، بحوض صبراته، شمال غرب ليبيا

قدمت من قبل :

ابراهيم عبدالهادى محمد التيكالى

تحت إشراف :

د. أسامة الشلطامي

قدمت هذه الرسالة استكمالا لمتطلبات الحصول على درجة الماجستير في علم

الجيوكيمياء

جامعة بنغازي

كلية العلوم

ديسمبر 2019